W MASS MEASUREMENT WITH MUONS AT $\sqrt{S} = 1.8$ TEV

BY

PHILIP SCHLABACH

B.S., Case Western Reserve University, 1985
M.S., University of Illinois, 1987

THESIS

Submitted in partial fulfillment of the requirements
for the degree of Doctor of Philosophy in Physics
in the Graduate College of the
University of Illinois at Urbana-Champaign, 1990

Urbana, Illinois

W Mass Measurement with Muons at $\sqrt{s} = 1.8$ TeV

Philip Schlabach, Ph.D.
Department of Physics
University of Illinois at Urbana-Champaign, 1990
Professor Steve Errede, advisor

The mass of the W vector boson has been measured from an analysis of $W \rightarrow \mu\ \nu$ decays in the CDF detector at the Fermilab Tevatron $\bar{p}p$ collider. The mass is 79.90±0.53(stat.)±0.31(syst.)±0.16(scale) GeV/c^2. When this result is combined with previous CDF measurements, $\sin^2\theta_W$ is determined to be 0.231 ± 0.008. These measurements place an upper bound on the mass of the unfound top quark.

This is for all those who never tried because they were convinced they could never make it.

Acknowledgments

I must acknowledge that had it not been for William I'd still be a graduate student – and very happy being one.

I want to thank Steve for rekindling my enthusiasm for physics. Were it not for him, I doubt I'd be a physicist today. Lee and Larry taught me most of what I know about analysis and bought me lots of beer while doing so.

During the dark, dismal, desparate days of bringing up the detector, during the dark dismal, desparate days of taking data, during the dark, dismal, desparate days of trying to measure the W mass, I got by with a little help from my friends. Amongst others, I thank Vic, Karen, Peter, Hovhannes, Paul, Tim, Leigh, Les, Jodi, Toshi, JJ, Steve, Dee, Paul, Drew, Mikio, John, Melissa, Chris, Keith, Brian, Dave, Tom, Jo, Randy, Andrew, Alain, and anyone who ever popped a top at 28 Sauk; well, not quite everyone...

I want to thank the technical and secretarial staff at the University of Illinois and at Fermilab who made my life easier in many ways. Dave and Jerry made the computer system here hum and have generally answered my silly questions without too many snide comments.

All of us who do muon analyses owe Tom and Dave for paving the road down which we stagger.

It's hard to think about physics when someone's using your stomach for a trampoline; I want to thank Kylie and Chad for periodically making me forget all about it.

I spent one memorable Thanksgiving with Scot, Joann, and Amanda.

I want to thank all my friends outside of particle physics who patiently listened to me gripe about my profession over the years: Fred, Toni, Rob, Christian, Glen, Jacque, Kathy, Paul, the only one I know who would pop out of bed at six in the morning to head

for a race at the drop of a hat, Dave, who taught me everything I know about cooking gumbo, and Leona, who let us use her kitchen, and Tom, without whom Urbana just isn't the same place. I want to thank Sam for introducing me to Steve Goodman and much more.

Finally, I want to thank my mother and father and Steve and Melissa their love and support during these five long years.

I have to acknowledge that this list could go on forever, and I've undoubtably forgetten someone, but the graduate college wants my thesis.

This research was supported in part by the U.S. Department of Energy under contract DE-AC02-76ERO1195.

CDF Collaboration for the 1988-1989 Run

F. Abe,[8] D. Amidei,[4] G. Apollinari,[11] M. Atac,[4] P. Auchincloss,[14] A. R. Baden,[6] A. Bamberger,[19] A. Barbaro-Galtieri,[9] V. E. Barnes,[12] F. Bedeschi,[11] S. Behrends,[2] S. Belforte,[11] G. Bellettini,[11] J. Bellinger,[18] J. Bensinger,[2] A. Beretvas,[4] J. P. Berge,[4] S. Bertolucci,[5] S. Bhadra,[7] M. Binkley,[4] R. Blair,[1] C. Blocker,[2] A. W. Booth,[4] G. Brandenburg,[6] D. Brown,[6] E. Buckley,[14] A. Byon,[12] K. L. Byrum,[18] C. Campagnari,[3] M. Campbell,[3] R. Carey,[6] W. Carithers,[9] D. Carlsmith,[18] J. T. Carroll,[4] R. Cashmore,[19] F. Cervelli,[11] K. Chadwick,[4] G. Chiarelli,[5] W. Chinowsky,[9] S. Cihangir,[4] A. G. Clark,[4] D. Connor,[10] M. Contreras,[2] J. Cooper,[4] M. Cordelli,[5] D. Crane,[4] M. Curatolo,[5] C. Day,[4] S. Dell'Agnello,[11] M. Dell'Orso,[11] L. Demortier,[2] P. F. Derwent,[3] T. Devlin,[14] D. DiBitonto,[15] R. B. Drucker,[9] J. E. Elias,[4] R. Ely,[9] S. Errede,[7] B. Esposito,[5] B. Flaugher,[14] G. W. Foster,[4] M. Franklin,[6] J. Freeman,[4] H. Frisch,[3] Y. Fukui,[8] Y. Funayama,[16] A. F. Garfinkel,[12] A. Gauthier,[7] S. Geer,[6] P. Giannetti,[11] N. Giokaris,[13] P. Giromini,[5] L. Gladney,[10] M. Gold,[9] K. Goulianos,[13] H. Grassmann,[11] C. Grosso-Pilcher,[3] C. Haber,[9] S. R. Hahn,[4] R. Handler,[18] K. Hara,[16] R. M. Harris,[9] J. Hauser,[3] T. Hessing,[15] R. Hollebeek,[10] L. Holloway,[7] P. Hu,[14] B. Hubbard,[9] B. T. Huffman,[12] R. Hughes,[10] P. Hurst,[7] J. Huth,[4] M. Incagli,[11] T. Ino,[16] H. Iso,[16] H. Jensen,[4] C. P. Jessop,[6] R. P. Johnson,[4] U. Joshi,[4] R. W. Kadel,[4] T. Kamon,[15] S. Kanda,[16] D. A. Kardelis,[7] I. Karliner,[7] E. Kearns,[6] R. Kephart,[4] P. Kesten,[2] R. M. Keup,[7] H. Keutelian,[7] S. Kim,[16] L. Kirsch,[2] K. Kondo,[16] S. E. Kuhlmann,[1] E. Kuns,[14] A. T. Laasanen,[12] J. I. Lamoureux,[18] W. Li,[1] T. M. Liss,[7] N. Lockyer,[10] C. B. Luchini,[7] P. Maas,[4] M. Mangano[11] J. P. Marriner,[4] R. Markeloff,[18] L. A. Markosky,[18] R. Mattingly,[2] P. McIntyre,[15] A. Menzione,[11] T. Meyer,[15] S. Mikamo,[8] M. Miller,[3] T. Mimashi,[16] S. Miscetti,[5] M. Mishina,[8] S. Miyashita,[16] Y. Morita,[16] S. Moulding,[2] A. Mukherjee,[4] L. F. Nakae,[2] I. Nakano,[16] C. Nelson,[4] C. Newman-Holmes,[4] J. S. T. Ng,[6] M. Ninomiya,[16] L. Nodulman,[1] S. Ogawa,[16] R. Paoletti,[11] A. Para,[4] E. Pare,[6] J. Patrick,[4] T. J. Phillips,[6] R. Plunkett,[4] L. Pondrom,[18] J. Proudfoot,[1] G. Punzi,[11] D. Quarrie,[4] K. Ragan,[10] G. Redlinger,[3] J. Rhoades,[18] M. Roach,[17] F. Rimondi,[19] L. Ristori,[11] T. Rohaly,[10] A. Roodman,[3] D. Saltzberg,[3] A. Sansoni,[5] R. D. Sard,[7] A. Savoy-Navarro,[4] V. Scarpine,[7] P. Schlabach,[7] E. E. Schmidt,[4] M. H. Schub,[12] R. Schwitters,[6] A. Scribano,[11] S. Segler,[4] Y. Seiya,[16] M. Sekiguchi,[16] P. Sestini,[11] M. Shapiro,[6] M. Sheaff,[18] M. Shochet,[3] J. Siegrist,[9] P. Sinervo,[10] J. Skarha,[18] K. Sliwa,[17] D. A. Smith,[11] F. D. Snider,[3] R. St. Denis,[6] A. Stefanini,[11] R. L. Swartz, Jr.,[7] M. Takano,[16] K. Takikawa,[16] S. Tarem,[2] D. Theriot,[4] M. Timko,[15] P. Tipton,[9] S. Tkaczyk,[4] A. Tollestrup,[4] G. Tonelli,[11] J. Tonnison,[12] W. Trischuk,[6] Y. Tsay,[3] F. Ukegawa,[16] D. Underwood,[1] R. Vidal,[4] R. G. Wagner,[1] R. L. Wagner,[4] J. Walsh,[10] T. Watts,[14] R. Webb,[15] C. Wendt,[18] W. C. Wester, III,[9] T. Westhusing,[11] S. N. White,[13] A. B. Wicklund,[1] H. H. Williams,[10] B. L. Winer,[9] A. Yagil,[4] A. Yamashita,[16] K. Yasuoka,[16] G. P. Yeh,[4] J. Yoh,[4] M. Yokoyama,[16] J. C. Yun,[4] F. Zetti[11]

[1] *Argonne National Laboratory, Argonne, Illinois 60439;* [2] *Brandeis University, Waltham, Massachusetts 02254*
[3] *University of Chicago, Chicago, Illinois 60637;* [4] *Fermi National Accelerator Laboratory, Batavia, Illinois 60510*
[5] *Laboratori Nazionali di Frascati, Istituto Nazionale di Fisica Nucleare, Frascati, Italy*
[6] *Harvard University, Cambridge, Massachusetts 02138;* [7] *University of Illinois, Urbana, Illinois 61801*
[8] *National Laboratory for High Energy Physics (KEK); Tsukuba, Ibaraki 305, Japan*
[9] *Lawrence Berkeley Laboratory, Berkeley, California 94720*
[10] *University of Pennsylvania, Philadelphia, Pennsylvania 19104*
[11] *Istituto Nazionale di Fisica Nucleare, University and Scuola Normale Superiore of Pisa, I-56100 Pisa, Italy*
[12] *Purdue University, West Lafayette, Indiana 47907;* [13] *Rockefeller University, New York, New York 10021*
[14] *Rutgers University, Piscataway, New Jersey 08854;* [15] *Texas A&M University, College Station, Texas 77843*
[16] *University of Tsukuba, Tsukuba, Ibaraki 305, Japan;* [17] *Tufts University, Medford, Massachusetts 02155*
[18] *University of Wisconsin, Madison, Wisconsin 53706;* [19] *Visitor*

Contents

1 Introduction

One of the many successes of the Weinberg-Glashow-Salam explanation of electromagnetic and weak interactions by a single electroweak theory was the prediction of massive vector bosons ($W^{\pm}$, Z^0) which mediate the weak force. The masses of these bosons were first measured at the CERN SPS collider in 1983 where the mass of the W was found by the UA1 group from 6 events to be 81 $^{+5}_{-5}$ GeV/c^2 [1] and by UA2 from 4 events to be 80^{+10}_{-6} GeV/c^2 [2]. The measurement of the Z mass was reported later that year. The result from UA2 was $M_Z = 91.9 \pm 1.3 \pm 1.4$ [3]; and from UA1, $M_Z = 95.2 \pm 2.5$ GeV/c^2 [4]. Both groups observed 4 Z^0 events.

More recently, there have been a flurry of measurements of vector boson masses. These measurements (especially those from the electron-positron machines) have substantially reduced the uncertainty on M_Z. CDF and MARK II announced new measurements in the summer of 1989. The CDF measurement ($M_Z = 90.9 \pm 0.3$ (stat.+syst.) ± 0.2 (scale) [5]) was made at the Fermilab Tevatron and that of MARK II ($M_Z = 91.11 \pm 0.23$ [6]) at the the Stanford Linear Collider. These results were soon followed by measurements at the LEP electron-positron collider from the ALEPH, OPAL, L3, and DELPHI experiments:[1] $M_Z = 91.10 \pm 0.06$ (stat.) [7], [8], [9], [10]. MARK II has also updated its result: $M_Z = 91.14 \pm 0.12$ [11].

Until LEP2 produces W^+W^- pairs from e^+e^- collisions, precise measurements of the W mass can only be made at $\overline{p}p$ colliders. UA2 has recently announced new measurements of M_W, M_Z, and the electroweak mixing angle: $\sin^2\theta_W = 1 - \frac{M_W^2}{M_Z^2}$ [12].

$$M_W = 80.79 \pm 0.31(\text{stat.}) \pm 0.21(\text{syst.}) \pm 0.81(\text{scale})$$

$$M_Z = 91.49 \pm 0.35(\text{stat.}) \pm 0.12(\text{syst.}) \pm 0.92(\text{scale})$$

$$\sin^2\theta_W = 0.2202 \pm 0.0084(\text{stat.}) \pm 0.0045(\text{syst.})$$

[1] This is the weighted average of the four LEP results.

This thesis presents a measurement of M_W at CDF, where the mass of the W is measured from its decay to muon and neutrino.

The thesis is organized as follows: Section 2 gives a brief overview of the Standard Model prediction of the W mass. This is followed by a description of hadroproduction of Ws and their decay to muon and neutrino in Section 3. We then turn to the experimental apparatus and data-taking in Sections 4, 5, and 6. A description of the features of the CDF detector utilized in this analysis and of the triggers used for accumulating the data is provided. In Sections 7 and 8, we discuss how the detector is calibrated to provide the most accurate measurement of the momentum of the two leptons from the W decay. We describe the selection of W decays from the data in Section 9. This includes a description of the topology of W decays and a description of the backgrounds to the sample. Having described the apparatus and the selection of the data sample, we next discuss the determination of the mass of the W. Section 10 gives an overview of the measurement. This is followed in Sections 11 and 12 by details of how W production and decay is simulated and the systematic uncertainties in the mass measurement due to the simulation. Sections 13 and 14 describe the fitting procedure and its associated systematics. We present the results of the analysis in Section 15, which is followed in Section 16 by a summary of how this measurement fits in with other experimental results and what its implications are for the Standard Model. We finish with a discussion of how the measurement might evolve with the expected upgrades to the CDF detector and with the additional data CDF will accumulate in the run which is scheduled to begin next spring.

2 Theoretical Motivation

The unification of the electromagnetic and weak theories into a "Standard Model" leads to the prediction of the existence of charged, massive, spin-1 vector bosons: $W^{\pm}$. Their

mass is also predicted in terms of fundamental constants of the theory.

$$m_W^2 = \frac{\pi\alpha}{\sqrt{2}G_F \sin^2\theta_W} \quad . \tag{1}$$

In the lowest-order calculation, α is constant, but higher-order radiative corrections lead to the running of α with Q^2. These radiative corrections are due to loop (in next-to-lowest-order) diagrams of the type shown in Fig. 1. One can rewrite the W mass with the effect of the radiative corrections lumped into a single constant as

$$m_W^2 = \frac{\pi\alpha_0}{\sqrt{2}G_F \sin^2\theta_W} \frac{1}{(1-\Delta r)} \quad , \tag{2}$$

where $\Delta r = f(m_{Higgs}, m_{top}, m_{quark}, m_{lepton}, \cdots)$ and $\alpha_0 \equiv \alpha(Q^2 = 0)$. The dependence

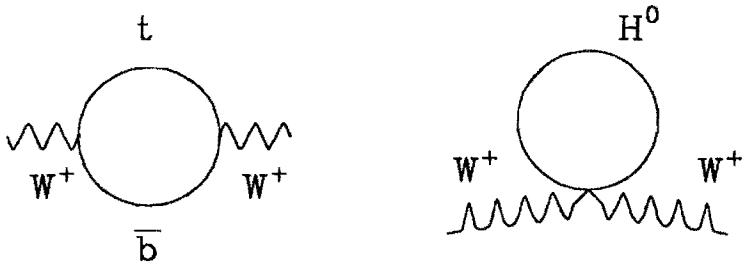

Figure 1: Next-to-lowest-order diagrams showing a $t\bar{b}$ loop and a Higgs loop in the W propagator on the left and right respectively. These radiative loops (and others like them) imply corrections to the mass of the W.

of m_W on the top and Higgs masses is shown in Fig. 2. The mass of the W is a sensitive probe of the electroweak theory. Not only is it an important parameter of the model, but its dependence on fundamental constants and on the masses of the unfound top quark and Higgs particle make its measurement a powerful tool in testing the theory.

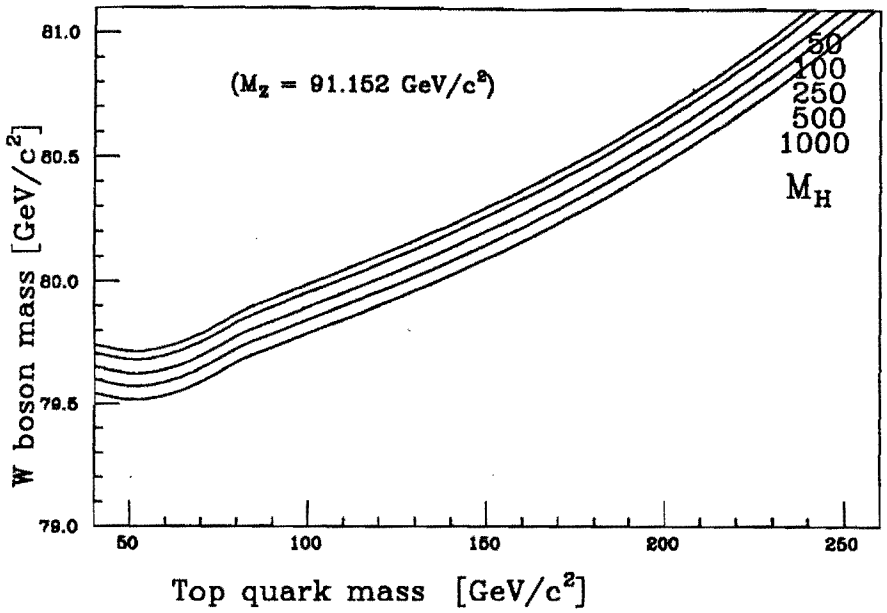

Figure 2: Dependence of the W mass on those of the top quark and Higgs particle [13].

3 Standard Model Production and Decay of the W

The W is created by annihilation of a quark-antiquark pair in a proton-antiproton collision:

$$u\bar{d}_c \to W^+; \quad \bar{u}d_c \to W^- \quad .$$

The d_c quark is the combination of d and s quarks due to Cabbibo mixing. The lowest-order (in α_s) diagram is shown in Fig. 3. The cross section for W production involves a sum over quark species,

$$\sigma(u\bar{d} \to W^+X) = \frac{1}{3}\sigma_0 x_p x_{\bar{p}}\{[u^{(p)}(x_p)\bar{d}^{(\bar{p})}(x_{\bar{p}}) + \bar{d}^{(p)}(x_p)u^{(\bar{p})}(x_{\bar{p}})]\cos^2\theta_c$$
$$+[u^{(p)}(x_p)\bar{s}^{(\bar{p})}(x_{\bar{p}}) + \bar{s}^{(p)}(x_p)u^{(\bar{p})}(x_{\bar{p}})]\sin^2\theta_c\} \quad , \qquad (3)$$

where the strange quark enters through the Cabbibo mixing of the d and s quarks in d_c. The factor of $\frac{1}{3}$ is due to the color of the quark and antiquark; u, d, s $(\bar{u}, \bar{d}, \bar{s})$ are the number densities of the quarks (antiquarks) in the proton or antiproton; $x_{p(\bar{p})}$ is the fraction of the proton (antiproton) momentum carried by the quark or antiquark;

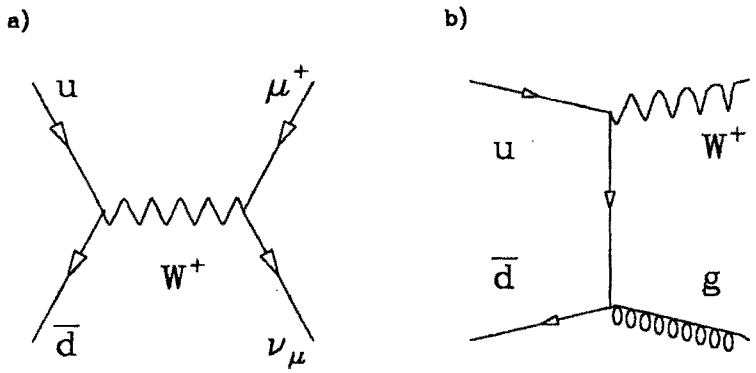

Figure 3: a) Lowest-order in α_s Feynman diagram for production of the W from quark-antiquark annihilation. This diagram shows subsequent decay to a muon and neutrino. b) A higher-order diagram with initial state radiation. In this diagram the quark radiates a gluon before formation of a W. This type of diagram can give non-negligible p_t to the W.

and $\sigma_0 = \frac{2\pi G_F}{\sqrt{2}}$. At the lower energies of previous measurements of the W mass, one could make the valence quark approximation (Fig. 4), where the the proton contains only quarks, and the antiproton, only antiquarks. Equation 3 then reduces to

$$\sigma = \frac{1}{3}\sigma_0 x_p x_{\bar{p}} \{u^{(p)}(x_p)\bar{d}^{(\bar{p})}(x_{\bar{p}})\cos^2\theta_c + u^{(p)}(x_p)\bar{s}^{(\bar{p})}(x_{\bar{p}})\sin^2\theta_c\} \quad .$$

At the 1.8 TeV energy of the Fermilab Tevatron, this approximation does not hold (see Fig. 5); and we need to include the effect of sea quarks within the hadrons. In addition to requiring that we include the the sea quark content of the hadrons in Equation 3, there is an effect on the polarization of the W. In the case where there are only valence quark interactions, the Ws are produced with specific polarizations due to helicity conservation (see Fig. 6). Since the quark comes only from the proton and the antiquark from the antiproton, the spin of the W boson is always aligned with the direction of the incident antiproton. This gives rise to specific asymmetries in the distributions of the decay

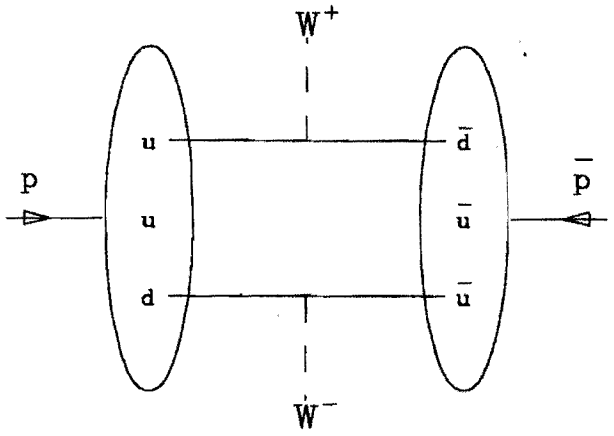

Figure 4: In the valence quark approximation, the proton contains only quarks and the antiproton only antiquarks. A W^+ thus comes from the annihilation of a u quark from the proton and a d antiquark from the antiproton; and the W^-, from a u antiquark in the antiproton and a d quark in the proton.

leptons. The differential cross section for the W^+ decay must vanish as a consequence of helicity conservation at $\hat{\theta} = \pi$ (see Equation 6). ($\hat{\theta}$ is defined in Fig. 6 as the angle between the emitted muon and the antiproton.) Thus, μ^+s (μ^-s) are emitted preferentially in the antiproton (proton) direction. However, since the u quark can come from the sea in the antiproton and the $\bar{d}$ antiquark from the sea in the proton, there will be an admixture of Ws with spin aligned along the proton direction with the obvious consequences for the μ^+ and μ^- decay angle distributions. We define the "polarization" distribution of the W^+, P_{W+}, as:

$$P_{W+} \equiv \frac{f^{u_p}}{f^{u_p} + f^{u_p}} \quad , \tag{4}$$

where f^{u_p} is the fraction of W^+ coming from u quarks in the proton, etc. The polarization of the W^- is defined analogously. We will use this definition when we describe our Monte Carlo simulation of W production. That the valence quark approximation does not hold is one of the differences between this measurement of the W mass and

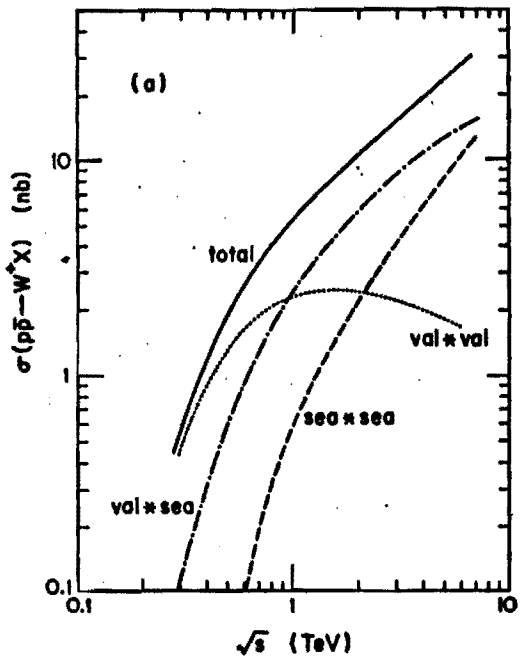

Figure 5: The cross section for W production as a function of the energy of the $\bar{p}p$ center of mass. The contribution from valence-valence, valence-sea and sea-sea quark interactions are also shown. The cross sections are from [14].

previous ones. The treatment of the sea quark distribution in the different computations of the parton distribution functions has important consequences (see Section 12.1) for the measurement.

The net momentum of the quark-antiquark pair gives the W its longitudinal momentum in the laboratory frame:

$$p_L = \frac{1}{2}(x_a - x_b)\sqrt{s} \quad . \tag{5}$$

In the lowest-order diagram (Fig. 3), the motion of the W in the direction perpendicular to the incoming quarks is small, coming entirely from the Fermi motion of the quarks within the hadrons. Initial state QCD radiation gives the W boson additional transverse motion, due to higher-order diagrams in which the quark or the antiquark (or both) radiate a gluon before the annihilation. For experimental reasons – the longitudinal component

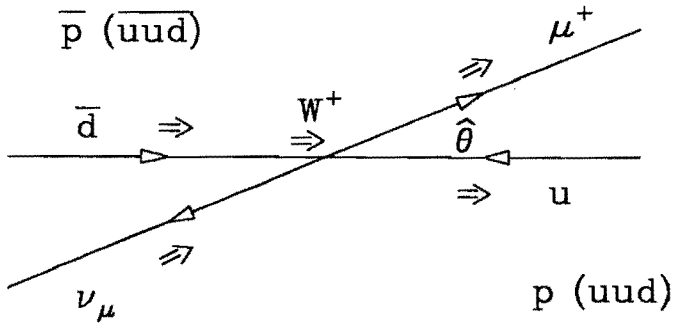

Figure 6: Momenta (single arrows) and helicities (double arrows) in the subprocess W decay to $\mu\,\nu$. Because ν_μ is left-handed, helicity conservation forbids emission of a μ^+ in the proton direction.

of the neutrino momentum in the W decay is not measured – we are interested only in the characteristics of W decays in the plane transverse to the proton-antiproton beam direction. In the W rest frame, the transverse momenta, p_t, of muon and neutrino are equal and opposite:

$$\hat{p}_t^2 = \frac{1}{4}\,\hat{s}\sin^2\hat{\theta} \quad .$$

The differential subprocess cross section is given by

$$\frac{d\hat{\sigma}}{d\cos\hat{\theta}}(u\bar{d} \to \mu^+\nu) = \sigma_0\,\frac{\hat{s}}{(\hat{s}-m_W^2)^2 + (\Gamma_W m_W)^2}\,(1+\cos\hat{\theta})^2 \quad , \tag{6}$$

where we see, as pointed out previously, the disappearance of the cross section at $\hat{\theta} = \pi$ required by helicity conservation. The total cross section is

$$\hat{\sigma}(u\bar{d} \to \mu^+\nu) = \sigma_0\,\frac{\hat{s}}{(\hat{s}-m_W^2)^2 + (\Gamma_W m_W)^2} \quad . \tag{7}$$

This Breit-Wigner relationship of $\hat{s}$, m_W, and Γ_W is a consequence of the matrix element for the subprocess. Changing variables in Equation 6 from $\cos\hat{\theta}$ to $\hat{p}_t^2$, we encounter the

Jacobian factor

$$\frac{d\cos\hat{\theta}}{d\hat{p}_t^2} = -\frac{2}{\hat{s}\cos\hat{\theta}}$$

and get

$$\frac{d\hat{\sigma}}{d\hat{p}_t^2} = 3\frac{\hat{\sigma}}{\hat{s}}\frac{1-2\frac{\hat{p}_t^2}{\hat{s}}}{\sqrt{1-4\frac{\hat{p}_t^2}{\hat{s}}}} \quad .$$

This is plotted in Fig. 7. The divergence at $p_t = \frac{\sqrt{s}}{2} \approx \frac{m_W}{2}$ is a consequence of the Jacobian and is known as the *Jacobian peak.* In determining the total cross section,

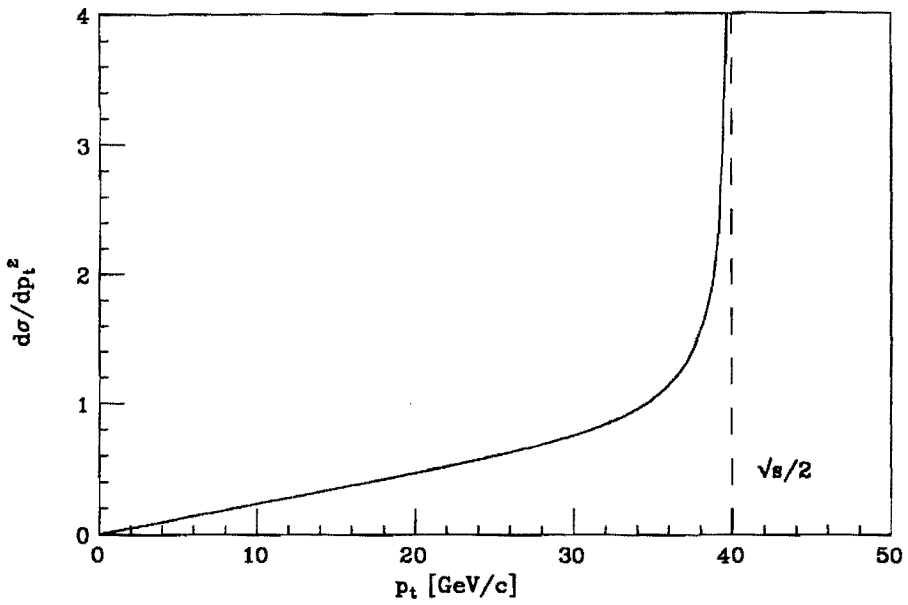

Figure 7: Differential subprocess cross section as a function of the p_t of the muon. This shows the characteristic Jacobian peak for a W mass of 80.0 GeV/c^2. The dimensions of cross section and p_t are nb and GeV/c respectively.

which is what we observe, this subprocess cross section is embedded in an integral over the $\hat{s}$ dependence of $\hat{\sigma}$ and sum over quark densities.

$$\sigma(\bar{p}p \to W^+ \to \mu^+ X) = \frac{1}{3}\sum_{q\bar{q}'}\int_0^1 dx_p \int_0^1 dx_{\bar{p}} q(x_p, m_W^2)\bar{q}'(x_{\bar{p}}, m_W^2)\hat{\sigma}(q\bar{q}' \to W^+ \to \mu + \nu) \tag{8}$$

The summation over $q, \bar{q}'$ is that defined by Equation 3. The integral over $\hat{s}$ removes the divergence and leaves a finite peak near $p_t = \frac{m_W}{2}$ (see Fig. 8). It is the characteristic

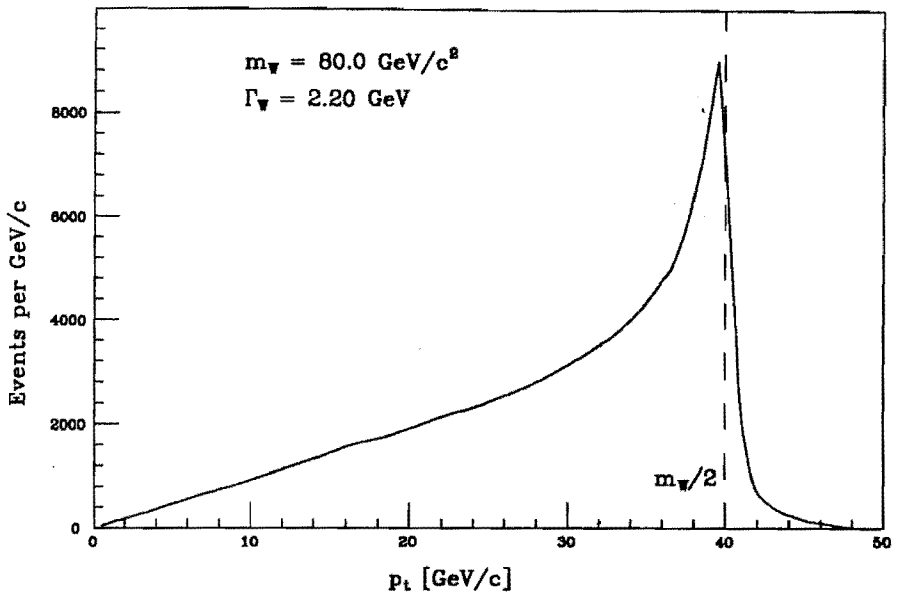

Figure 8: Distribution of p_t^μ for $\bar{p}p \rightarrow W \rightarrow \mu\,\nu$ events. This calculation does not include the effects of a finite p_t^W or detector resolution. It shows only the effect of the parton distribution functions on the sum over quark species and integration over the Breit-Wigner dependence of $\hat{s}$. A W mass of 80.0 GeV/c^2 and width of 2.2 GeV were assumed in the calculation. MRS-E [15] parton distribution functions were used.

shape of this process and its dependence on m_W that we will use to determine the mass of the W.

4 Detector

The Collider Detector at Fermilab (CDF) is a 5000 ton detector built to study the 900 GeV/c on 900 GeV/c $\bar{p}p$ collisions produced by the Tevatron [16]. A view of the detector is shown in Fig. 9. The CDF coordinate system defines the positive z-axis along the direction traveled by the protons. The y-axis is vertically upward and the x-axis is radially outward from the center of the Tevatron ring. The angles θ and ϕ are the usual polar and azimuthal angles. Pseudorapidity, $\eta = -\ln\tan(\theta/2)$, is the approximately Lorentz invariant variable appropriate for distributions in the polar angle. A superconducting solenoid, 5 m long and 3 m in diameter, provides a magnetic field

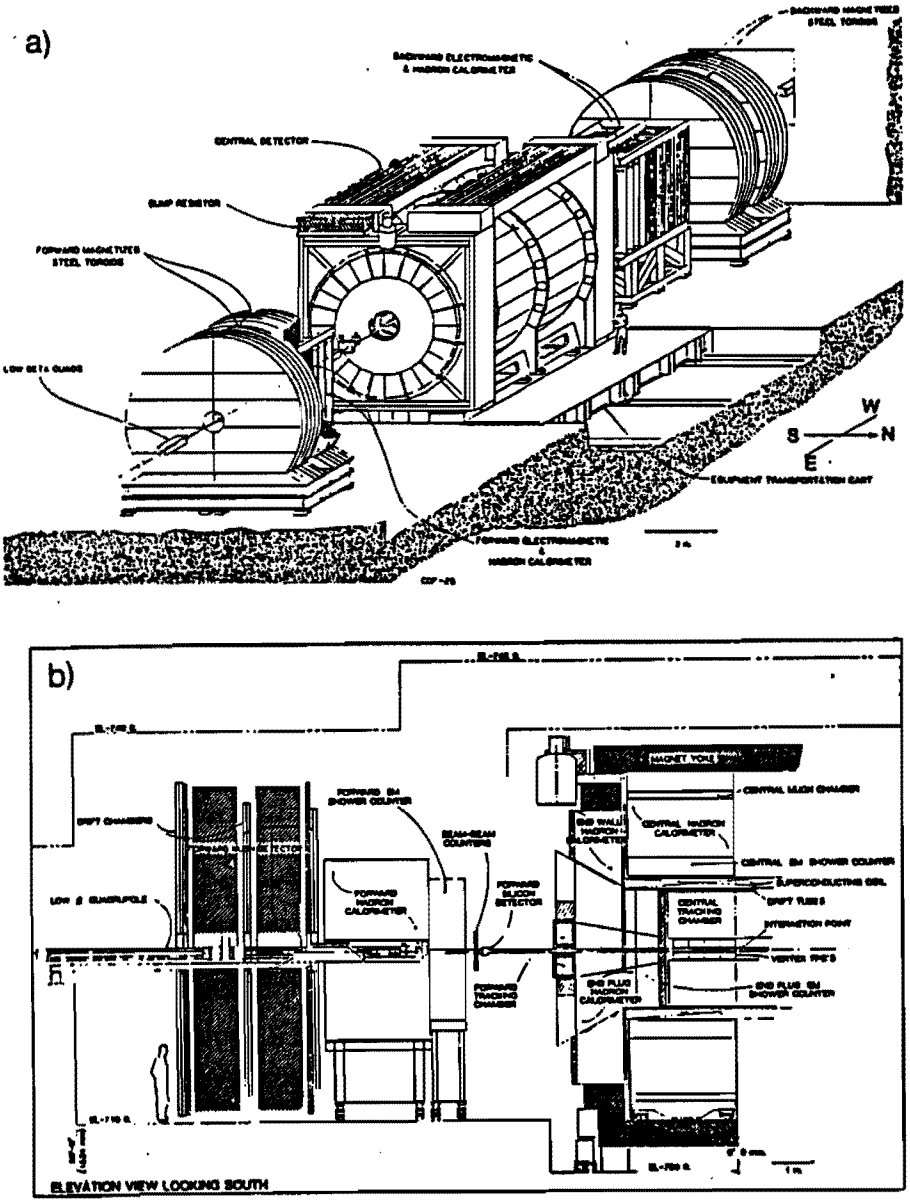

Figure 9: The CDF detector as configured during the 1988-89 run when the data used in this analysis was taken. a) Perspective view. Note the segmentation of the central calorimeter into 15° "wedges" in ϕ and the division into removable "arches" at z=0. b) Side view.

of 1.4116 T for measurement of charged particle momenta in the central region ($40° < \theta < 140°$). Calorimeter coverage extends to within 2° of the beamline ($2° < \theta < 178°$, $-4.2 < \eta < 4.2$) and has uniform granularity in pseudorapidity and azimuthal angle.

4.1 Tracking Detectors

Eight Vertex Time Projection chambers (the VTPC) [17] surround the beam pipe, extending 2.8 m along the beam line. Each chamber is divided into 8 slices covering 45° in ϕ. Alternate chambers are rotated 11.3° in ϕ to provide small-angle stereo information. These chambers measure charged particle tracks in the R-z plane to within 3.5° of the beam line. The azimuthal segmentation and small-angle stereo provide some ϕ information; however, only the R-z information is used to measure the z vertex of the $\bar{p}p$ interaction. The primary interaction vertex of the $\bar{p}p$ collisions is reconstructed with an rms resolution of 1 mm in the z direction. This is used as a reference point in computing the transverse energy ($E_t = E \sin\theta$) deposited in each calorimeter cell. Multiple interaction vertices in the same beam crossing are reconstructed. (At a luminosity of 10^{30} $cm^{-2}s^{-1}$, one in five events contains a multiple interaction.) The distribution in z of reconstructed vertices in candidate W events is shown in Fig. 10 and is well described by a Gaussian of mean -1.5 cm and width 31 cm. This spread in vertices reflects the convolution of the finite-length proton and antiproton bunches in the collider and not an inherent limitation of the detector.

The Central Tracking chamber (CTC) [18] surrounds the VTPC. The CTC was designed to measure charged particle tracks in the R-ϕ plane, determining their curvature in the magnetic field and thus their momentum. The CTC has 84 layers of sense wires grouped together in nine "superlayers" (see Fig. 11). The nine superlayers are subdivided into measurement cells so that the drift distance is approximately 40 mm in all superlayers. This corresponds to a drift time of about 800 ns. Five superlayers have twelve sense wires, parallel to the beam direction, per cell. These axial layers are used for the primary

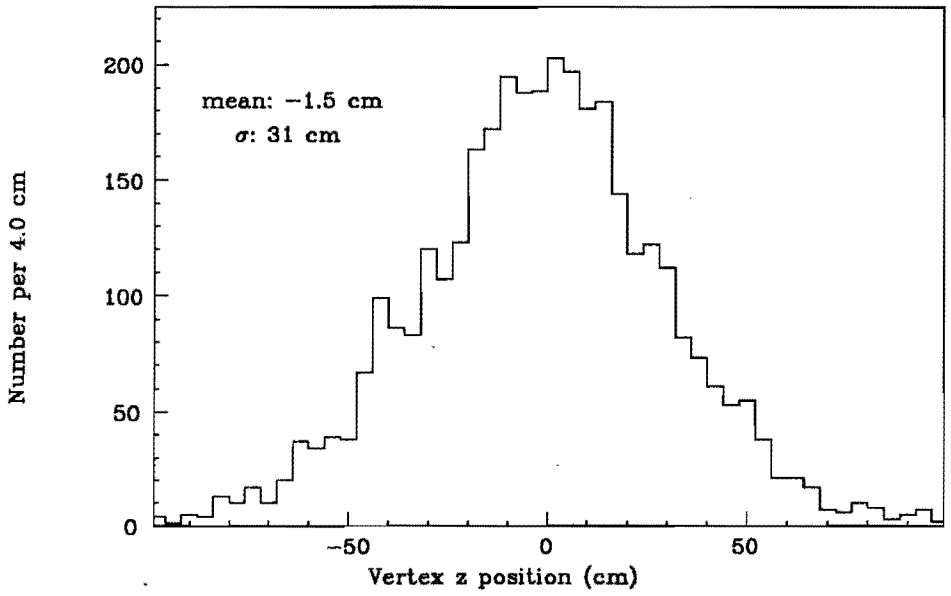

Figure 10: The event vertex distribution along the beam line for the inclusive W decay candidates. In the final event sample, we require $|z| \leq 60$ cm.

determination of track curvature. In the other four superlayers, each cell has six sense wires with an alternating $\pm 3°$ stereo angle with respect to the beam line to enable determination of the polar angle of tracks. Measurement of the polar angle, together with track curvature, allows full 3-dimensional reconstruction of track momentum. The cells in all superlayers are tilted at a 45° angle with respect to the radial direction to compensate for the Lorentz angle of electron drift in the magnetic field. Thus, in the ideal case, the electrons drift azimuthally, simplifying the time-to-distance relationship. For tracks with $p_t > 1$ GeV/c, the azimuthal position in each layer is measured with greater than 200 μ precision. Stereo position is measured with a typical precision of 1 mm at each superlayer.

The rms momentum resolution of the CTC is $\delta p_t/p_t = 0.0020 \times p_t$ (p_t in GeV/c) for isolated tracks. Adding a beam position point to the track ("beam constraint") in R-ϕ extends the effective tracking radius, ℓ, from 1.0 to 1.3 m thereby improving the effective resolution (which scales as $1/B\,\ell^2$) to $\delta p_t/p_t = 0.0011 \times p_t$. Complete tracking

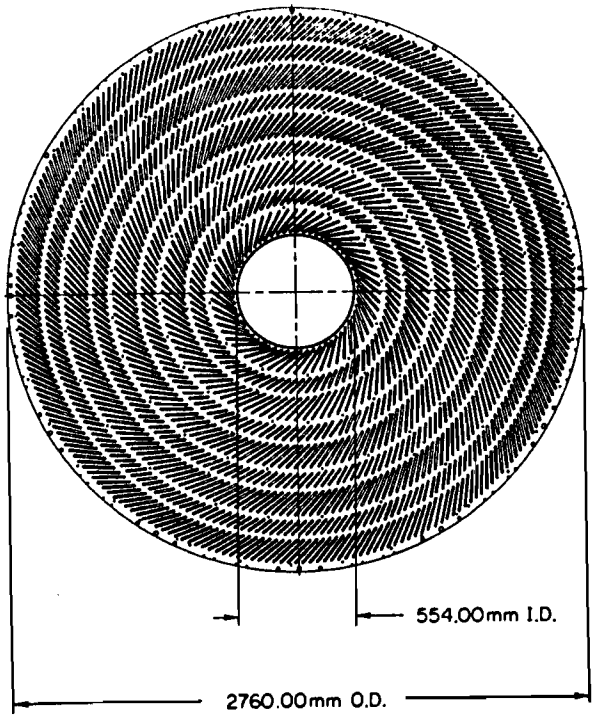

Figure 11: The layout of wires at the end of the Central Tracking chamber (CTC) showing the grouping into 9 superlayers and the 45° Lorentz angle.

information is only available for $40° < \theta < 140°$. Tracks outside this angular region do not pass through all layers of the chamber, degrading the momentum measurement resolution. Tracks which reach the Central Muon detector (described in Section 4.3) have passed through all layers of the CTC.

The Central Drift Tube (CDT) [19] array is attached to the outer edge of the CTC cylinder. This cylindrical array of 2 016 12.7 mm diameter drift tubes provides high-precision R-ϕ-z information for tracking charged particles. The drift tubes, operating in the limited streamer mode, provide a z-resolution: $\sigma_z < 0.1\%L$ (where L is the length of the tube). Track information is available in the R-ϕ view from single-hit TDCs, and in R-z, by charge division. The CDT track information was not included in the track parameter calculation used in this analysis. It was, however, included for a short time in the CDF trigger (described in Section 5) and was part of the primary trigger for taking

unbiased cosmic ray data used in efficiency studies of the Central Muon level 1 trigger (Section 5.1) and in determination of the cosmic ray background in the W mass sample (Section 9.2).

4.2 Calorimeters

The CDF detector has three calorimeter systems: Central, Plug, and Forward (see Fig. 9). The central ($-1.1 < \eta < 1.1$) system is made up of lead-scintillator shower counters (CEM) followed by an iron-scintillator hadron calorimeter (CHA). The central calorimeter is divided into 15° segments ("wedges") in ϕ and 0.1 segments in η. These modules are grouped into four removable "arches" which surround the solenoid (see Fig. 9). The boundaries between wedges and arches produce gaps in calorimeter coverage. Outside the central region, the active elements of the calorimeters are gas proportional chambers with cathode-pad readout. The plug electromagnetic and hadronic calorimeters cover $1.1 < |\eta| < 2.4$, and the forward electromagnetic and hadronic calorimeters cover $2.2 < |\eta| < 4.2$. All calorimeters have a projective tower geometry. Tower segmentation, $\delta\eta$ x $\delta\phi$, in the central region is 0.1 x 15°, while in the plug and forward regions it is 0.1 x 5°.

Energy balance in the overall CDF calorimeter is used to the infer the transverse energy of the neutrino coming from the W decay. This is the subject of Section 8. Calorimeters were calibrated in testbeams with electrons and pions. The gas electromagnetic calorimeter energy scales have been checked with electrons from W and Z decays. The central hadron calorimeter is studied with charged pions from $\overline{p}p$ collisions [20]. Using the approximate energy balance of di-jet events, we transfer our better understanding of the central hadron calorimeter to the forward and plug calorimeters using jets with one jet in the central and one in the forward or plug [21]. We also implement offline filters to remove noise in the gas calorimeters [22]. This noise removal substantially improves the resolution of the inferred neutrino energy [23], as energy balance is particularly sensitive

to detector-specific noise.

We study the overall calorimeter performance in minimum-bias events.[2] These studies are also used to understand the background event from spectator hadrons underlying the $W \rightarrow \mu\ \nu$ decay.

4.3 Muon Detector

The Central Muon Chambers [24] are at 3470 mm from the beam line. These drift chambers operate in the limited-streamer mode, flowing 50%/50% argon/ethane with 0.7% ethanol, and provide muon detection for $56° < \theta < 124°(\eta < .63)$. Approximately 5 hadronic absorption lengths of the CDF central calorimeter separate the muon chambers from the interaction region. The four layers of drift cells in a muon chamber provide 3-dimensional reconstruction of tracks via single-hit TDCs in the transverse direction and charge division in the longitudinal direction. The muon chambers are grouped in 15° wedges in ϕ at the outer edge of the calorimeter wedges described above (see Fig. 12). Only 12.6° of the wedge is covered by the chambers, leaving a 2.4° gap between adjacent wedges. Each wedge consists of three muon chambers. In addition to the gap in coverage in ϕ, there is a 1.5° gap in θ between the arches (at $\theta = 90°$). A muon chamber has 16 drift cells divided into 4 layers and 4 towers (see Fig. 17). To reduce the number of electronic channels needed for chamber readout, sense wires from alternate cells in each layer are ganged at $\theta = 90°$. The sense wires from alternate layers in a muon tower lie on a radial line with the nominal $\bar{p}p$ interaction point. The other 2 are offset from this line by 2 mm at the radial chamber midpoint to resolve the ambiguity as to on which side (in ϕ) of the sense wire the particle passed. The outer edge of each cell is held at a nominal voltage of -2500 volts with the sense wire at the center at 3000 volts, producing an approximately constant electron drift velocity in the cell of 45 μm/ns. The maximum

[2]These are events taken with minimal trigger requirements and, thus, assumed to have little trigger bias. These are generic $\bar{p}p$ events selected by requiring only a forward-backward coincidence of hits in scintillation counters on either side of the central detector (see Fig. 9).

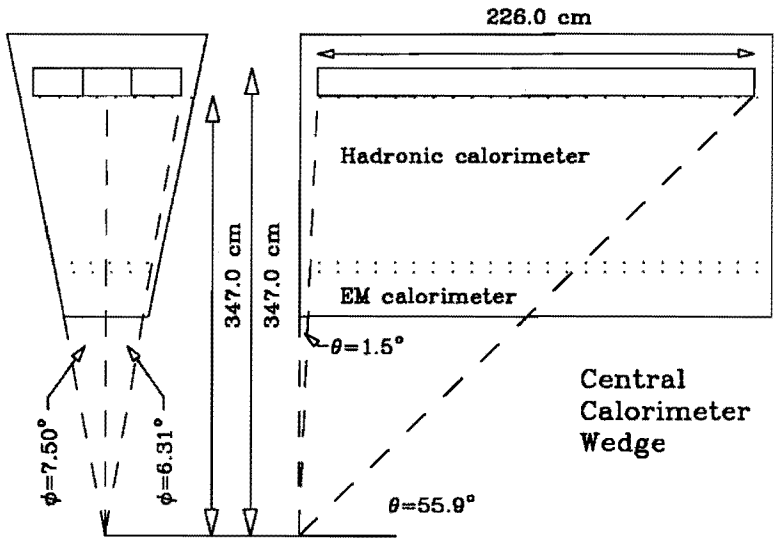

Figure 12: A central calorimeter wedge. The relative positions of the electromagnetic and hadronic calorimeters and the muon chambers are indicated.

drift time is approximately 700 ns.

Cosmic ray data taken by CDF show the resolution of the chamber in the drift direction to be $\sigma = 250$ μm (Fig. 13) and in the longitudinal direction to be $\sigma = 1.2$ mm [24]. Calibration of the muon chambers and central calorimeters with 57 GeV/c muons in a testbeam show the energy deposited by muons in the electromagnetic calorimeter to be Landau distributed with a mean of 300 MeV; while in the hadronic calorimeter, the mean energy deposit is 2.1 GeV (see Fig. 14) [25]. From Fig. 15, we see that the energy deposited in the central calorimeter by muons from candidate J/Ψ and Υ decays have the same characteristic distributions. The mean energy deposited in the electromagnetic calorimeter is 300 MeV and in the hadronic calorimeter is 2.0 GeV.

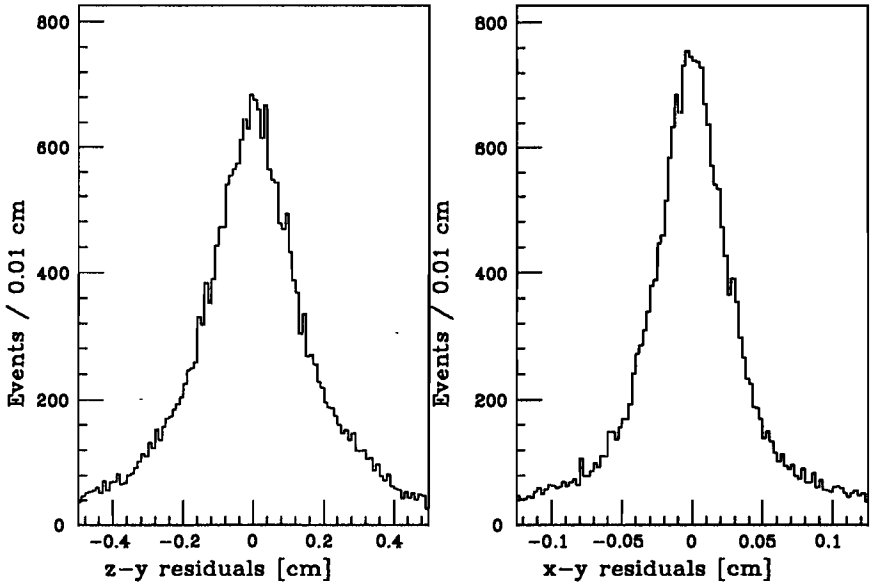

Figure 13: a) Plot of residuals for cosmic ray tracks using charge division information. The rms resolution along the sense wire is 1.2 mm. b) Residuals for these tracks using drift time information. The rms resolution in the drift direction is 250 μm.

5 Trigger

The interaction rate during the 1988-89 run at the Tevatron collider was 10^5 times higher than the rate at which the CDF data acquisition system could record data. To sift interesting events from the background, a four-level trigger system [26] was used. With a minimal trigger bias, the data rate was reduced at each level to one at which the next higher level could perform a more sophisticated analysis without incurring significant deadtime. Typical deadtimes for each trigger level are given in Table 1. We give here a brief overview of the trigger system, followed by a description of the triggers relevant to the collection of W candidate events. A schematic view of the muon trigger is shown in Fig. 16.

The lowest level of the triggering scheme, level 0, selected inelastic collisions by requiring that time-of-flight counters on either side of the interaction region be hit in coincidence. This was also the minimum-bias trigger. This trigger decision was made

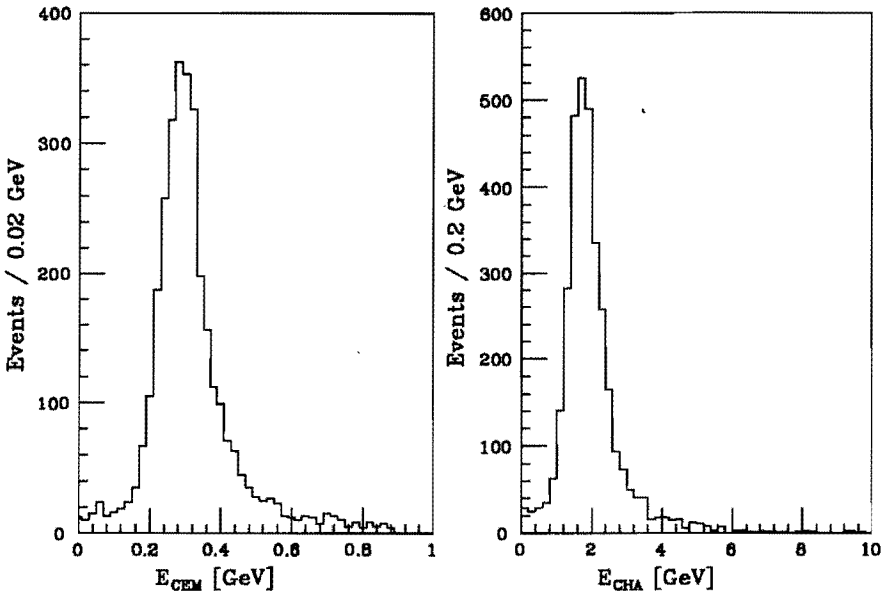

Figure 14: Energy deposition by 57 GeV/c testbeam muons in the central calorimeters.

in the 3.5 μs between beam crossings. For events which contained an inelastic collision, data-taking was inhibited during the next beam crossing in order for the level 1 trigger decision to be made.

For two weeks at the end of the 1989-90 run, the level 0 trigger was modified. In addition to the trigger on hits in the time-of-flight counters, a trigger on a coincidence of hits in the inner two superlayers of the CTC and a hit cluster in the CDT detector was added. This is described in greater detail in Appendix B.

A level 1 decision was made in the 7 μs allowed by level 0. If the event selected by level 0 failed the level 1 criteria, the front-end electronics were reset for taking data from the second crossing after the initial level 0 decision. Trigger decisions at this level were based on global features of calorimeter energy deposition, overall energy balance in the electromagnetic or hadronic calorimeters, and the presence of stiff tracks in the CTC or the muon chambers.

The level 2 trigger operated on global event topology in order to decide whether to initiate readout of the the detector. Requirements were more stringent at this level since

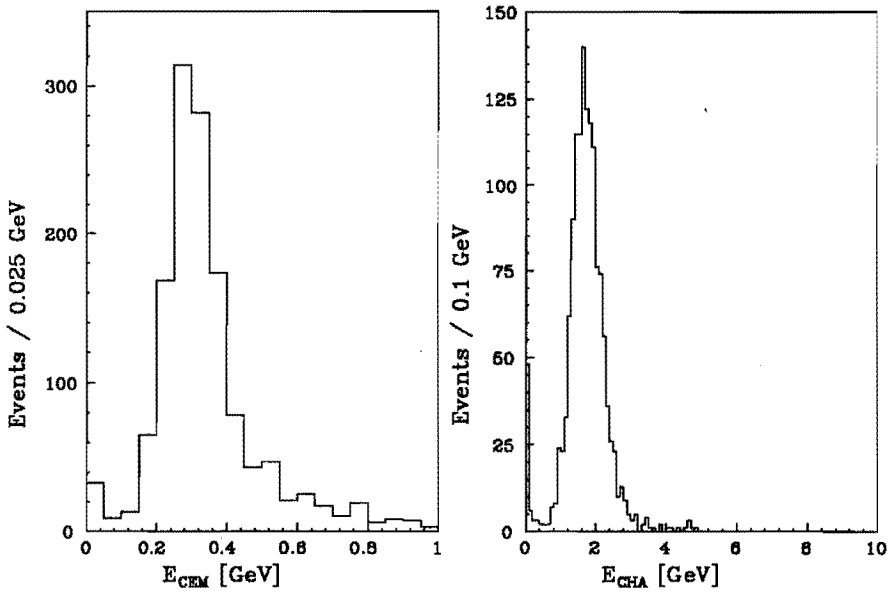

Figure 15: Energy deposited in the CEM and CHA calorimeters by J/Ψ and $\Upsilon \rightarrow \mu\mu$ decay candidates; an invariant mass plot for J/Ψ and Υ decay candidates is shown in Fig. 26.

detector readout typically took 10-15 ms. At this level the trigger could begin to match different trigger objects. Stiff tracks in the CTC were matched to tracks in the muon chambers. Tracks could be associated with clusters of energy; clusters of energy, with each other, and so forth. The transverse energy balance in the calorimeter as a whole was also determined at this level. The level 2 trigger decision was typically made in $\sim$100 μs.

A level 3 trigger system was implemented during the course of the 1988–89 run. This consisted of a farm of 60 Motorola 68020 processor nodes which analyzed the raw data from different events in parallel. The intent is to eventually run the complete CDF event reconstruction code; but, due to constraints on execution time, streamlined versions of the complete code were used during the 1988-89 run. The trigger decision took $\sim$20 seconds of real time per event per processor.

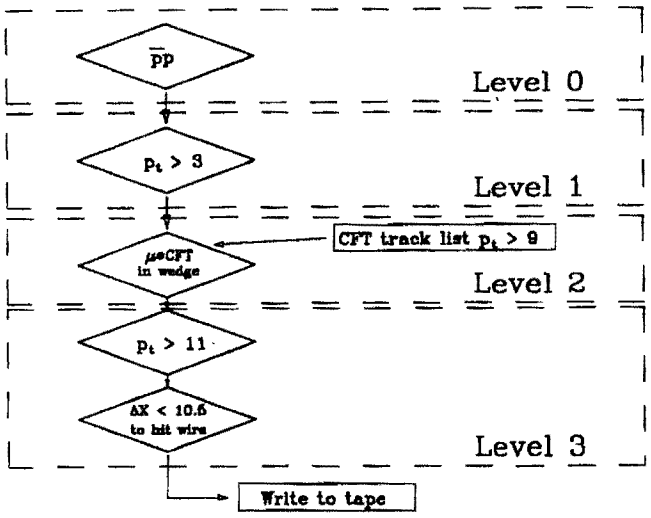

Figure 16: Muon trigger logic. The different trigger levels are highlighted. Note the prerequisite nature of the triggers from the requirement of a $\bar{p}p$ collision in level 0 to the writing of the data on tape. Momenta are given in units of GeV/c and ΔX in cm.

5.1 Muon Level 1 Trigger

The level 1 muon trigger used prompt hits from the muon TDCs to identify high p_t tracks in the muon chambers. The trigger imposed a cut on the time difference $|t_4 - t_2|$ or $|t_3 - t_1|$ (see Fig. 17) between the two radially aligned wires in a muon tower, where t_i is the drift time to the i-th wire in a muon tower [27]. This specifies the maximum allowed angle of a track with respect to an infinite momentum track emanating from the $\bar{p}p$ vertex, and, thus, a cut on the p_t of the track: $p_t = \frac{154}{\Delta t}$ GeV/c with Δt in ns. Due to multiple scattering, it was possible for a particle with initial p_t above the trigger threshold to fail the timing cut and vice versa. This lead to a soft turn on of the trigger with track p_t. About two thirds of the data used in this analysis was gathered with a level 1 p_t threshold of 3 GeV/c, while the other third was taken early in the 1988-89 run with a threshold of 5 GeV/c. Measurement of the trigger efficiency with cosmic rays shows that, for the two thresholds used and for tracks with transverse momenta greater than 15 GeV/c, the

Trigger Level	Fractional Dead Time
Level 0	0.00 (1.3) %
Level 1	7.7 %
Level 2	3.0 %
DAQ	7.0 %
Total	18.1 %

Table 1: Deadtime incurred at each level of the trigger system. Beam luminosity was 0.6×10^{30} cm^{-2}s^{-1} when this data was taken. DAQ (data acquisition) deadtime includes all deadtime incurred after level 2. It includes level 3 as well as deadtime, if any, incurred waiting for events to be emptied out of level 3 and written to magnetic tape so that new events can be transferred into level 3. The level 0 deadtime is truly 0.0%. However, there is a deadtime of 1.3% associated with this trigger. Fermilab's 150 GeV Main Ring is used to accumulate protons for later injection into the Tevatron. The Main Ring passes directly over the CDF detector. During certain parts of its cycle, beam losses will splash into the CDF detector, generating false triggers. Triggering is inhibited during these parts of the Main Ring cycle. This inhibit is implemented in level 0, leading to a 1.3% deadtime.

efficiency of muon track finding in level 1 was above 90% and independent of p_t (see Fig. 18). The muon trigger made a separate decision for each muon tower and triggered if the time difference between either of the two radially aligned pairs was less than the trigger threshold.

5.2 CFT

In level 2, muon triggers (as well as other CDF level 2 triggers) used 2 dimensional tracks found by Central Fast Tracker (CFT), a hardware track processor which used fast timing information from the CTC to detect high transverse momentum tracks. The track finder was a 19 stage digital pipeline which analyzed "prompt" hits from the 4392 axial sense wires of the CTC to identify tracks. Tracks were found by comparing the hits in the CTC to predetermined hit patterns for the range of transverse momenta allowed by the CFT trigger threshold [28]. The processor had 8 p_t bins covering the range from 2.5 to 15 GeV/c. In an average of 2.5 μs per event, the identification of all high p_t tracks in the

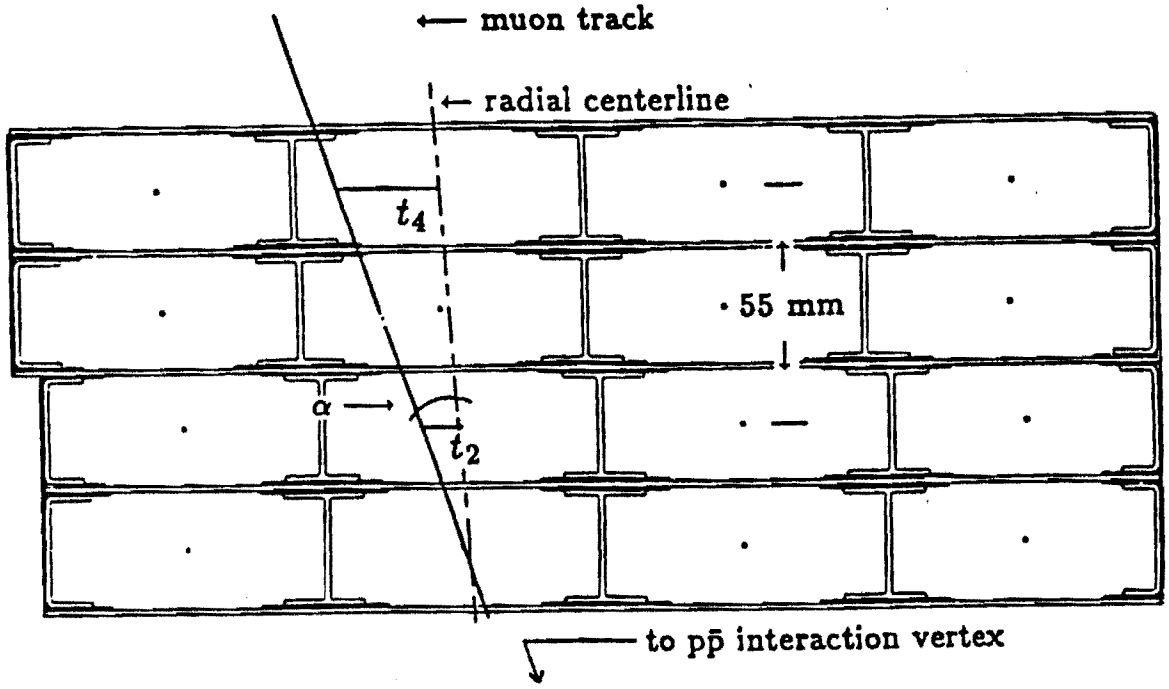

Figure 17: A cross section of a muon chamber. Note the incident muon with an angle α and its associated drift times in two of the four layers.

CTC was complete; and the list of found tracks was presented to the rest of the CDF trigger system for use in level 2 decisions. The momentum resolution was $\frac{\delta p_t}{p_t^2} = 3.5\%$. The data used in this analysis was taken with a 9 GeV/c track p_t threshold. The efficiency for finding tracks above this threshold was 98%, independent of track transverse momentum and track density in the event (see Fig. 19 and Fig. 20).

5.3 Muon Level 2 Trigger

The level 2 muon trigger first decoded the list of CFT tracks to predict where in the Central Muon chambers tracks could hit. This was done by a special FASTBUS module which used look-up tables stored in RAM to predict from the ϕ-coordinate of the CFT track and its uncertainty, which, if any, of the muon towers should be hit [29]. (The calculation of the RAM tables took into account multiple scattering.) These predictions

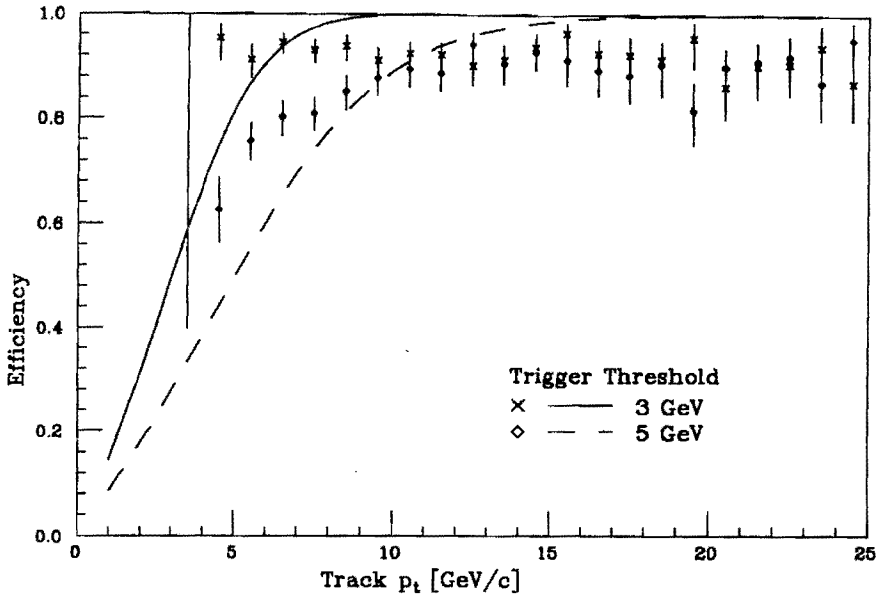

Figure 18: The efficiency of the CMU level 1 trigger as a function of track p_t. The efficiency for both the 3 and 5 GeV/c thresholds is plotted. The solid and dashed lines show the predicted efficiency for the 3 and 5 GeV/c thresholds respectively. The calculation included only the effect of multiple scattering, not the effects of δ-rays from the calorimeter hitting the muon chambers. These δ-rays cause a several percent inefficiency.

were passed to other FASTBUS modules which matched them to hit muon towers. The p_t and ϕ for CFT tracks which had a match were then passed to the rest of the level 2 trigger system for combination with other information in the final level 2 trigger decision. The data used in this analysis was taken requiring only a match between a hit muon tower and a CFT track. The efficiency of this trigger is plotted in Fig. 20.

5.4 Muon Level 3 Trigger

The level 3 muon trigger first verified the level 2 result by checking for a track from the CFT with p_t above the level 2 threshold. Then, for each track, a fast, 2-dimensional reconstruction algorithm determined the track p_t and the ϕ of the track at the radius of the muon chambers. If no track above the level 3 p_t threshold of 11 GeV/c was found, the event was rejected. If such a track was found, the filter looped over all stubs identified

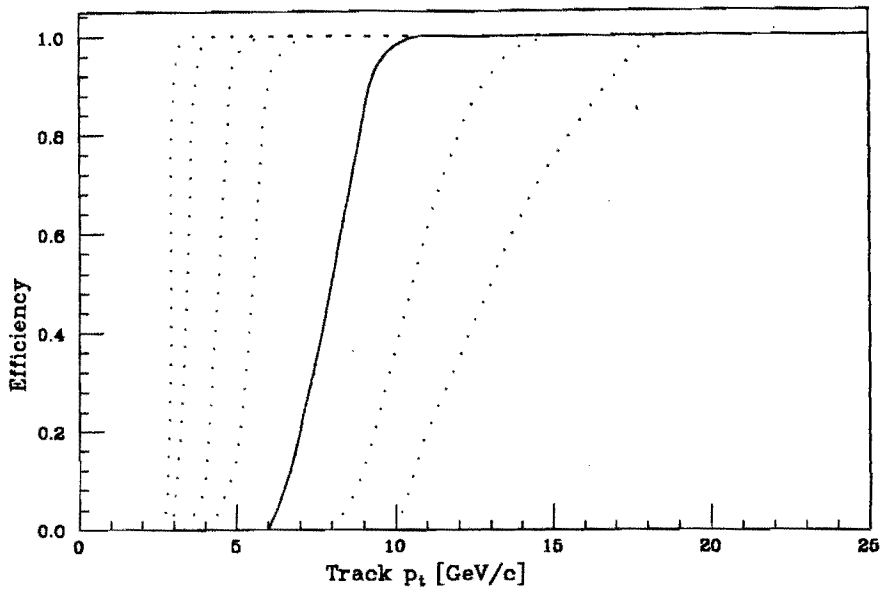

Figure 19: From left to right, the predicted CFT efficiency as a function of track p_t for p_t bins 0 to 6 respectively. The solid line is the efficiency for the threshold used (p_t bin 4) for taking the data analyzed in this thesis. Bin 4 is nominally 90% efficient at 9.2 GeV/c.

by the muon level 1 trigger electronics and determined the highest p_t track matching the stub. This match was done in the local variable, X, where X is defined as the axis lying along the lowest layer of CMU sense wires in a chamber and X=0 is defined at the radial line passing through the middle of the three muon chambers in a wedge. If an unambiguous determination of which of the two ganged sense wires was hit could be made, the matching window was $\pm$10.5 cm from the hit wire. Otherwise, the window was $\pm$10.5 cm from either wire. If no match with a track of p_t greater than the threshold was found, the event was rejected.

6 Data Collection

We collected the data used in this analysis over a 12-month period from June of 1988 through May of 1989. The peak machine luminosity grew to over 2×10^{30} cm^{-2} s^{-1}. A plot of the integrated luminosity accumulated during the 1988-89 run is given in Fig. 22.

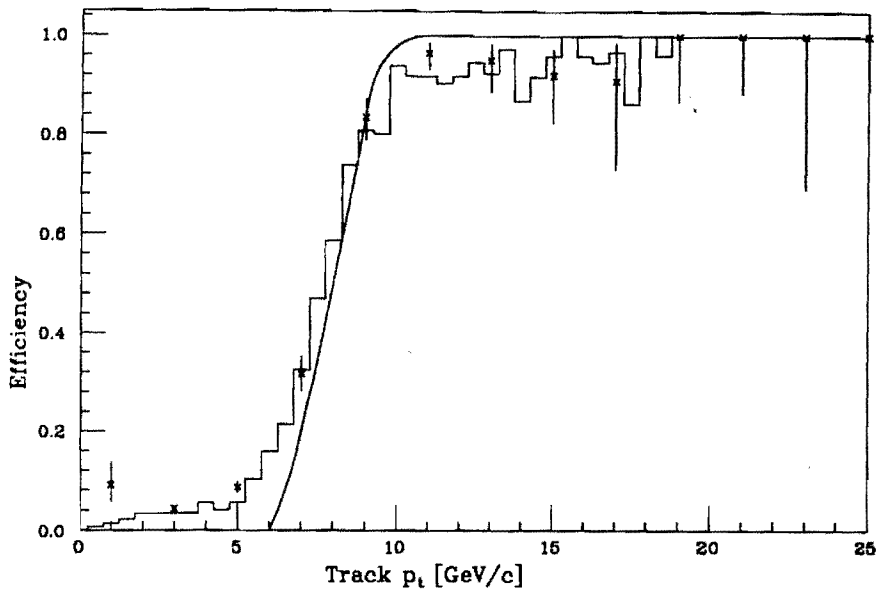

Figure 20: The plotted points give the CMU level 2 trigger efficiency as a function of track p_t. The solid line is the predicted efficiency for the CFT alone for the 9 GeV/c threshold. The histogram is a measurement of the efficiency of the CFT at this threshold using $\bar{p}p$ data.

A total of 9.1 pb^{-1} was delivered by the Tevatron, of which only 4.7 pb^{-1} was written to tape for an overall data-taking efficiency of 52%. There were several reasons for this inefficiency. Luminosity provided during the first two months of the run was not used for analysis, as the detector and data acquisition system were begin debugged during this period. This was a small effect. Part of the inefficiency was attributable to the higher than expected luminosity provided by the accelerator, which lead to a larger deadtime in the trigger at peak luminosity (see Table 2). From Fig. 23 one can see that by the middle of the run CDF achieved weeks where the efficiency was limited by trigger deadtime.

Early in the run, the time taken to turn on detector systems was a significant fraction of the total inefficiency.[3] Detector turn on was often a 10 to 20 minute-long process, occurring during the time of highest luminosity. (Beam luminosity decayed rapidly during

[3]Many detectors were powered down when no stored beam was present in the Tevatron. These were principally wire chambers sensitive to the large current spikes induced by the inevitable particle losses during the injection and focussing of the beam at the beginning of a store.

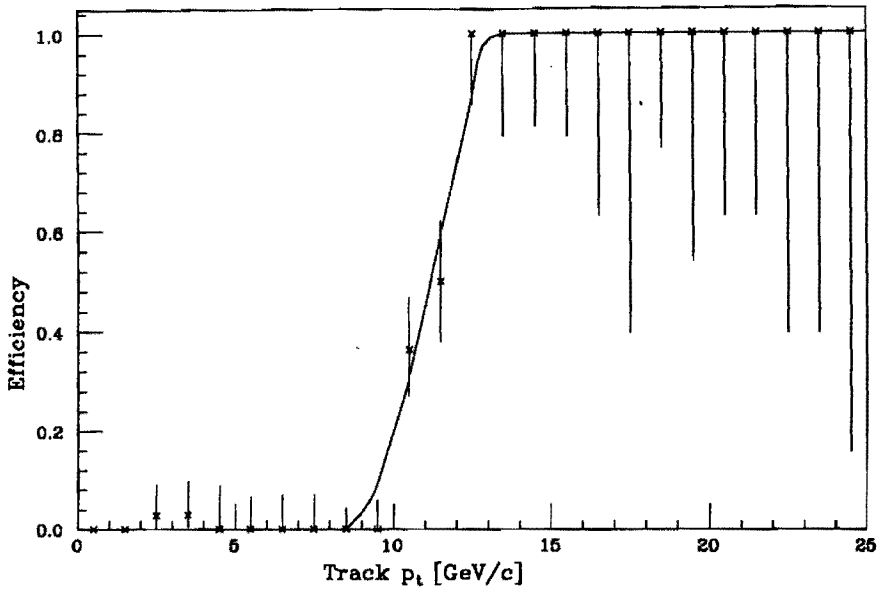

Figure 21: Trigger efficiency of the CMU level 3 trigger as a function of track p_t. The solid curve is a smooth fit to the data.

the first few hours of a store.) Improvements in control code and operator training reduced this substantially over the course of the run. This was routinely done in 5 minutes or less during the latter half of the run and did not result in a substantial loss of data (see Appendix C). The time for detector turn on at this point was limited by the rate at which the power supplies could charge the high source capacitance of the chambers.

Equipment failure, power supply trips induced by beam losses, and pilot error remained the biggest problem. Both the data acquisition system and the power supply control and monitoring system were complex. CDF had very few real "experts". Real-time control of the experiment was given to shifts of 4 persons who served for ten days with a two day overlap between shifts. The shift persons' only real knowledge of the systems often consisted of a few recipes of commands needed to perform the most common procedures. There were entire shifts of people whose first sight of the detector came when it rolled out of the collision hall at the end of the run. To believe that one could

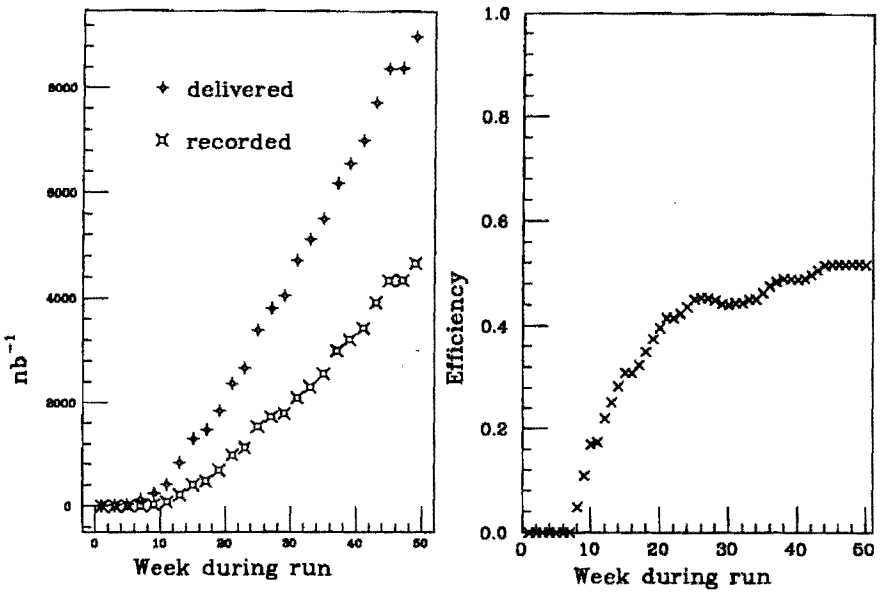

Figure 22: a) The integrated luminosity delivered by the accelerator (upper curve) and collected by the CDF experiment (lower curve). b) The ratio is a measure of the data collection inefficiency of the experiment. Sources of this inefficiency are discussed in the text.

take people off the street (more or less) and train them in a day or two to run a large, sophisticated detector was incredibly naive. To then wonder why the overall efficiency was 52% is to miss the point. It took a tremendous effort to achieve even that. One has only to look at the large fluctuations in week-by-week efficiency (Fig. 23) to understand the problem. The difference between the overall rate of 52% and the 75% efficiency that could have been achieved is the difference between operation of the detector by those who knew what they were doing and those who did not.

The overall trigger rate was limited to 1-2 Hz by the speed with which data could be transferred to tape. The average event record contained 150 kbytes of information. Our 4.4 pb^{-1} sample of analyzed data consists of 4×10^6 events recorded on 5 500 magnetic tapes. The sample useful for muon analysis contains only 3.9 pb^{-1} due to a malfunction of the muon trigger during the early part of the run.

Trigger Level	Fractional Dead Time
Level 0	0.00 (0.4) %
Level 1	15.5 %
Level 2	7.1 %
DAQ	7.1 %
Total	30.2 %

Table 2: Deadtime incurred at each level of the trigger system. Beam luminosity was $1.5 \times 10^{30}\text{cm}^{-2}\text{s}^{-1}$ when this data was taken. At high luminosities deadtime increased substantially as the trigger system was swamped with collisions. (This is to be contrasted with the 18% deadtime at 0.6×10^{30}.) At luminosities of $2 \times 10^{30}\text{cm}^{-2}\text{s}^{-1}$, the deadtime was even higher as we began to be limited by tape writing speed.

Data was written to tape in increments of "runs".[4] A run began when proton and antiproton beams had been injected into the Tevatron, had been focused, and were stable (an accelerator "store"). A run would typically last 10-12 hours, although there were runs of 24 hours or more. A run ended when the Tevatron beams were dumped. Runs were also ended to calibrate the energy scales of the gas calorimeters which were sensitive to atmospheric pressure variations or to change the trigger configuration. During the two to three hours between stores, various calibration and monitoring procedures for the detector front-end electronics and the trigger system were done to prepare for the next accelerator store.

7 Muon Momentum Measurement Calibrations

Of the detector calibrations, calibration of the Central Tracking chamber is the most important for muon analyses. It is in the CTC that we measure the muon p_t. Calibration of the muon chambers enters only in our ability to match tracks in the muon chamber with those in the CTC. We also need to know the magnetic field in the region outside the solenoid, which we use in our extrapolation of the CTC track to the muon chambers.

[4]Note that "run" is also used to refer to the entire 12 months of 1988 and 1989 during which data was taken. It should be clear from the context which meaning is correct.

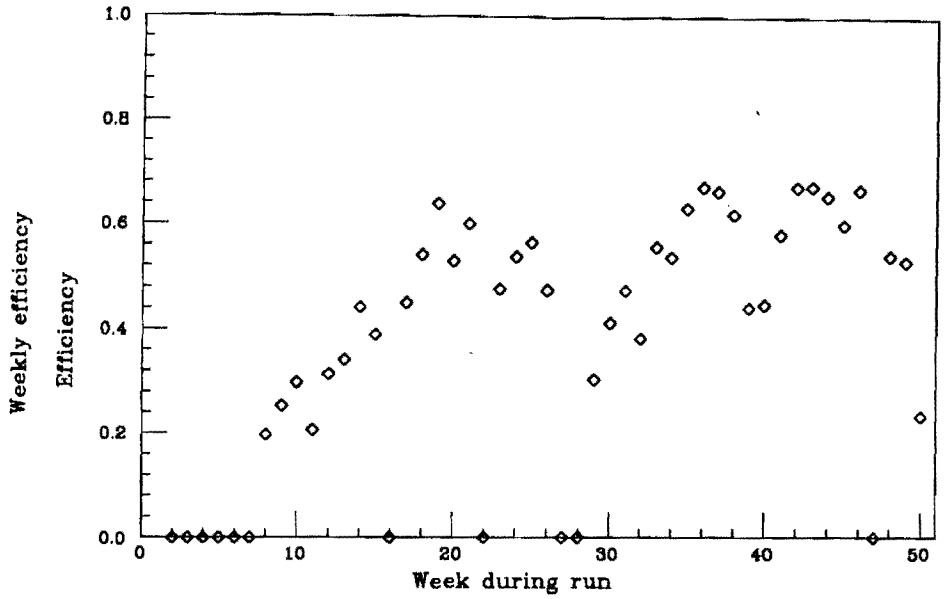

Figure 23: The fraction of luminosity delivered by the accelerator written to tape on a week-by-week basis during the 1988–89 run.

Calibration of the muon chambers and readout electronics will be discussed briefly; details are given in Appendix D. This is followed by a description of the calibration of the tracking chamber.

7.1 Muon Chamber Calibration

Calibration of the muon chambers is straightforward. We first calibrate all the charge-to-voltage (ADC) and time-to-voltage (TDC) channels of the muon readout electronics. The gains of all muon ADC and TDC channels were calibrated on a test stand before insertion into the front-end [30] of the CDF data acquisition system. The relative timing between channels is determined by pulsing the sense wires. The global timing is fixed by comparing the earliest hit distribution with the beam-beam crossing time. The baseline electronic pedestal corresponding to zero charge deposit on the sense wires was measured for each ADC channel between data-taking runs and subtracted online in the front-end system. The drift velocity is monitored by comparing the drift time differences between

alternate layer sense wires which are offset by 2 mm. The charge division coordinate, R,[5] is mapped into z position by a calibration procedure using signals from Fe^{55} sources built into the chambers [31]. Periodic surveys of the muon chambers' positions fixed them relative to the beam interaction region.

The matching of CTC tracks to muon stubs serves as a check of the calibration. Fig. 24 shows the distribution of differences between extrapolated CTC tracks and muon

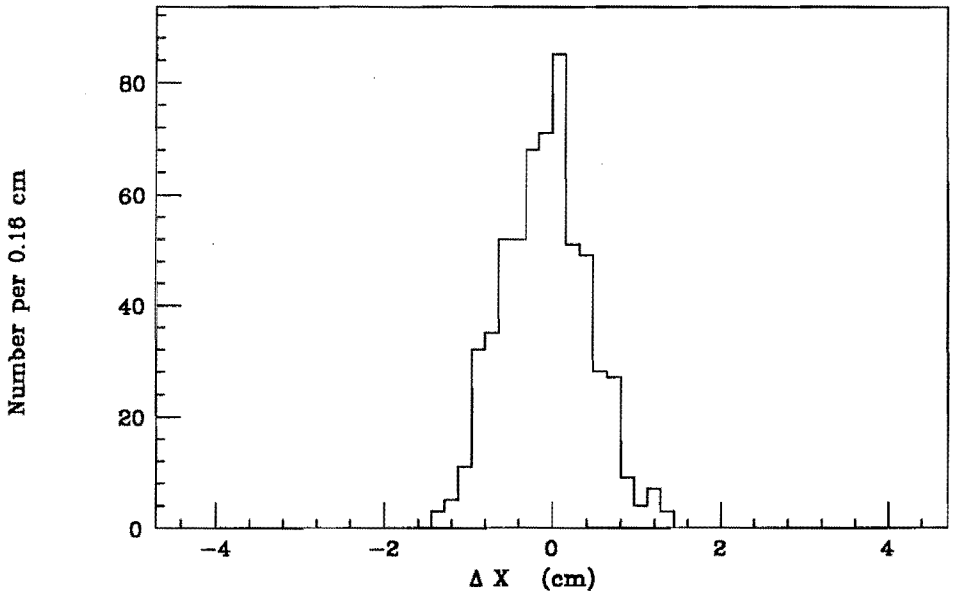

Figure 24: The match in the R-ϕ plane between the CTC track extrapolated to the lowest wire plane of the muon chambers and the muon chamber track at that point for $W \rightarrow \mu\,\nu$ decays. X = 0 is defined to be the midpoint of three muon chambers in the calorimeter wedge.

stubs and is consistent with what is expected from multiple scattering.

7.2 Calibration of the Central Tracking Chamber

Calibration of the CTC [32] begins with determination of pedestals and drift constants associated with the readout electronics and the fields within the chamber. Analog signals from the CTC sense wires are first passed through preamplifiers mounted on the chamber

[5] $R = \frac{Q0-Q1}{Q0+Q1}$, where $Q0$ and $Q1$ are the analog signals read from the two ends of the sense wires.

and then to Amplifier-Shaper-Discriminator (ASD) cards [18] which shape the pulses, amplify them and convert them to a time-over-threshold signal. Data from the ASDs, mounted on the detector, is read out by multi-hit FASTBUS TDCs outside the collision hall. Channel-dependent timing pedestals which take into account channel-to-channel variations in the TDCs and differing signal cable lengths are measured by pulser signals. This calibration is done whenever TDC cards are changed. Minimum-bias data is then used to map the difference between the response of the chamber-mounted preamps to calibration signals and signals from real $\bar{p}p$ collisions. Since preamps are not changed, this is done once. Whenever the fields in the chambers are modified (i.e. when the chamber voltage changes), a conversion table from drift time to drift distance is mapped as a function of position in the chambers. This is done with minimum-bias data. Time-dependent channel pedestals, which are primarily due to variations in the common-stop logic controlling the TDCs, were measured on a run-by-run basis using events taken during normal data-taking from a rate-limited minimum-bias trigger. Data from this stream was also used to measure time-dependent parameters describing pulse-slewing in the TDCs and drift velocity variations within the chamber. This data stream was analyzed online, and results were then used in offline reconstruction of tracks. In each event, the timing offsets of all interactions with respect to the nominal $\bar{p}p$ beam crossing were found from a fit of all primary tracks in each interaction. A run-by-run beam position axis was measured from an iterative analysis of a few thousand tracks in each run. The axis measurement allowed the axis to be off center and tilted with respect to the CTC. The beam position varied little from run to run, allowing the exclusion of secondary tracks from this analysis by requiring that the tracks come from within 1 mm of the previous beam position. (Secondary tracks do not effect the beam position but do artificially inflate the uncertainties of the measurement.) The beam center is determined with 5 μm accuracy [33]. The lateral profile of the beam is 50 μm.

Random errors in nominal wire positions can be measured wire-by-wire by minimizing

track residuals for a large number of events. These are typically less than 10 μ, consistent with chamber design. We correct for these and the effect of gravity on the wires (wire sag). Having reconstructed tracks with this alignment, we find 180 μm average axial residuals and average stereo residuals of 225 μm.

Systematic, layer-dependent, alignment problems are more difficult to measure. The fitting procedure will simply assimilate them into the fit parameters. To find possible systematic alignment errors, we must constrain some of the degrees of freedom of the fitting procedure. We constrain the tracks to come from the measured beam position and from the vertex z position as measured by the VTPC. The orientation of the CTC within the CDF coordinate system is also fixed. To measure azimuthal alignment errors, we need to constrain track curvature. Azimuthal alignment errors effect the chamber's resolution at high momenta by producing charge-dependent sagitta errors of the type:

$$\frac{1}{p} = \frac{1}{p_{\rm true}} + \frac{1}{\Lambda} \tag{9}$$

$$\frac{1}{p} = \frac{1}{p_{\rm true}} - \frac{1}{\Lambda} \tag{10}$$

where Λ is a false momentum. By comparing the average energy to momentum ratios, $< E/p >$, for a large sample of electrons and positrons from W decays, we get

$$\frac{1}{\Lambda} = \frac{1}{< E >_+ + < E >_-} \left(< E/p >_+ - < E/p >_- \right) \quad . \tag{11}$$

As a constraint on track curvature, we force $< E/p >$ for electrons and positrons to be equal. This then allows the determination of 166 wire-layer azimuthal offsets.[6] The size of these sign-dependent shifts is 3%. These misalignments are understood as a twisting of the CTC endplates with respect to each other due to chamber loading and a breaking of azimuthal symmetry due to the slits cut in the endplates for cable passage. Alignment reduces the size of the sign-dependent shifts by an order of magnitude to 0.3%.

[6] An offset is measured for the 84 wire-layers at each end of the chamber. An overall rotation of each end of the CTC is not measured, leaving 166 constants.

We use cosmic rays, which provide apparent tracks of equal momenta but opposite charge, to verify the alignment. Fig. 25 shows the improvement in the curvature match

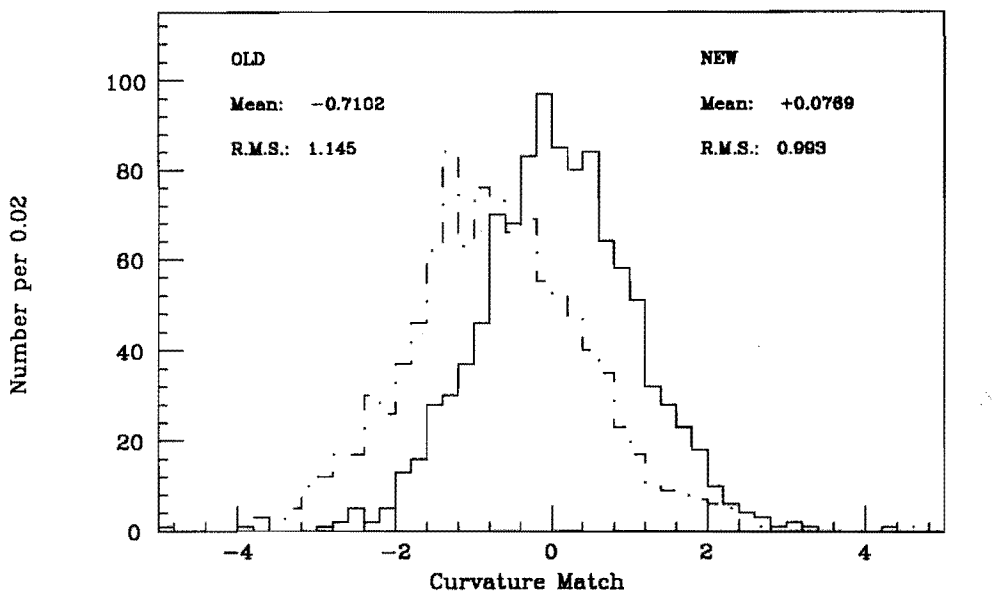

Figure 25: The difference in curvature between the incoming and outgoing branches of a cosmic ray. These branches leave tracks of equal but oppositely-signed curvature. The solid (dotted) histogram shows the matching after (before) chamber alignment. The matching is normalized to the curvature uncertainties; and, thus, should have mean 0.0 and sigma 1.0. The residual charge asymmetry corresponds to an 0.3% difference in momentum for a 35 GeV/c track.

of the two branches of the cosmic ray after the alignment. This alignment of the chamber does not change the scale of the momentum measurement; it only improves the resolution at high momentum. When the beam position is included in the track fit, the chamber resolution is $\delta p_t/p_t = 0.0011 \times p_t$ (p_t in GeV/c) with $\delta p_t = 1.3$ GeV/c for the 35 GeV/c tracks typical of W decay muons. As a check of the tracking chamber calibration, we compare the Z mass we measure with our $Z^\circ \rightarrow \mu^+\mu^-$ sample [5] to the world average, which is dominated by the LEP measurements. Our result is: $m_Z(\mu\mu) = 90.71 \pm 0.45$ GeV/c^2. The PDG average [34] is $m_Z = 91.161 \pm 0.031$ GeV/c^2. These are in good agreement.

Remaining tracking chamber distortions consist of a possible overall magnification, due, for example, to mechanical loading. An overall dilation of the chamber is equivalent

to an error in the magnetic field strength. The nominal wire locations are surveyed with a precision of 50 μm, and the absolute mean magnetic field is known to $\pm$ 0.05%. We check for residual chamber dilation using samples of J/ψ and Υ di-muons (see Fig. 26). Muon

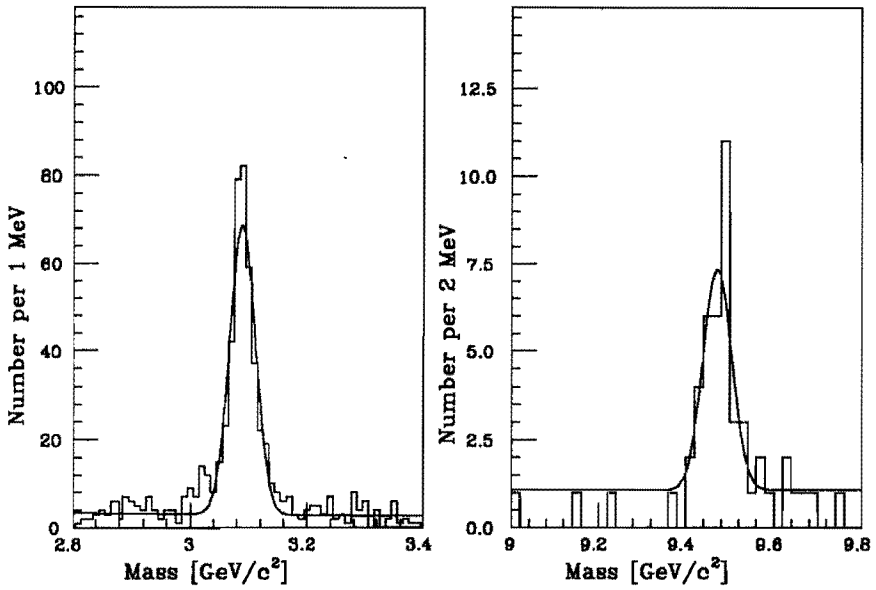

Figure 26: a) Invariant mass of a sample of J/ψ decay di-muons and b) a sample of Υ decay di-muons which we use as a check of our tracking chamber's momentum scale. The mass of the J/ψ from a fit to the data is 3097 ± 1 MeV, and of the Υ is 9.469 ± 0.010 GeV. The world average values are 3096.9 ± 0.1 MeV and 9.460 ± 0.001 GeV respectively [35]. From the agreement between our measured masses and the world's average masses, we conclude that our momentum scale from the tracking chamber is known to better than 0.2%.

transverse momenta in these samples are typically 5-6 GeV/c. Compared to the Particle Data Group value [35], the J/ψ mass agrees to within its 0.03% statistical uncertainty; and the Υ mass is $0.1 \pm 0.1\%$ high. We conclude that the upper limit on the tracking chamber momentum scale uncertainty is 0.2%[5], averaged over charges.

8 Neutrino Energy Measurement Calibrations

We use minimum-bias events taken during the course of normal data-taking to study the measurement of missing transverse energy, $\not\!\!E_t$. There are overall offsets of -250 ± 40 MeV

in x and 100 ± 40 MeV in y in the projections of the $\not\!\!E_t$ of these events as shown in Fig. 27. We correct the missing energy in each event for these offsets when reconstructing

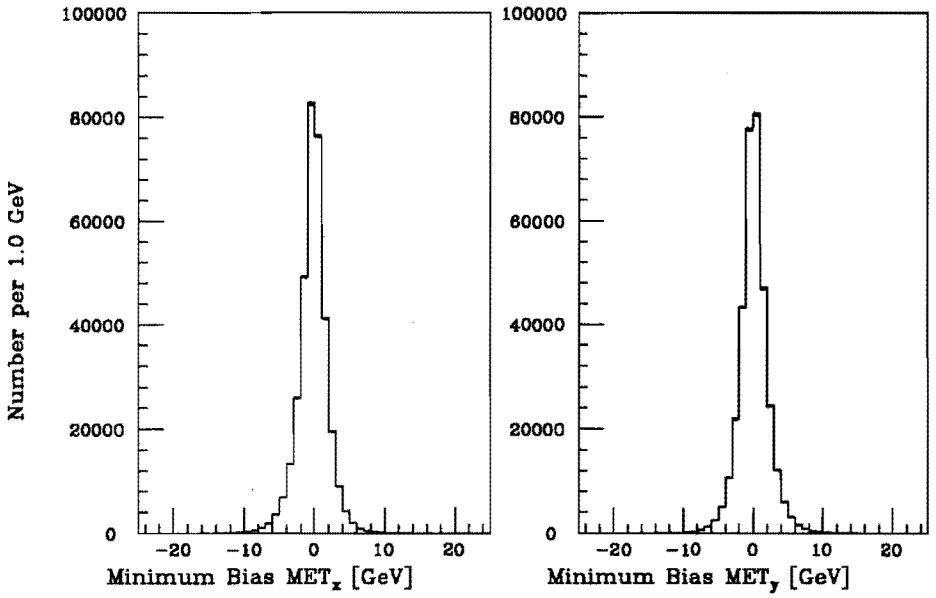

Figure 27: a)The x projection of $\not\!\!E_t$ for 340 000 minimum-bias events. b) The y projection.

the W decay.

When measuring $\not\!\!E_t$, we must separate the muon from the rest of the event. The muon deposits only an average of 2.3 GeV of its energy in the calorimeter. Therefore, we cannot assume that all the missing energy is due to the neutrino. In fact, the muon has nearly as large an effect on the uncorrected $\not\!\!E_t$ measurement as the neutrino (see Section 9). To correct $\not\!\!E_t$ for the muon, we first remove its energy deposition in the calorimeter from the missing energy calculation. We expect the muon energy deposition to be in a single calorimeter tower and remove that tower from the computation of $\not\!\!E_t$. If the muon traverses more than one calorimeter tower, this algorithm will underestimate the amount of energy deposited. We use our overall understanding of the energy deposition of the muon to partially correct for this by removing 1.5 GeV from $\not\!\!E_t$ even if the measured energy deposition is less than this. We define $\vec{\not\!\!\mu}$ to be the $\vec{\not\!\!E}_t$ of the event with the muon

energy nominally removed. As it is defined, $\vec{\not{\mu}}$ contains the energy missing due to both muon and neutrino. We subtract the effect of the muon using its measured momentum and reconstruct the neutrino transverse momentum as

$$\vec{\nu} = \vec{\not{\mu}} - \vec{p}_t^{\,\mu} \quad . \tag{12}$$

The response of the calorimeter to the low energy hadrons that typically comprise the underlying event in W decay has been measured [21]. A combination of several effects cause the calorimeter to undermeasure the energy of charged particles below 10 GeV. The response of our non-compensating calorimeters falls off at low energy. In addition, charged particles with momenta below 400 MeV will curl up in the solenoidal magnetic

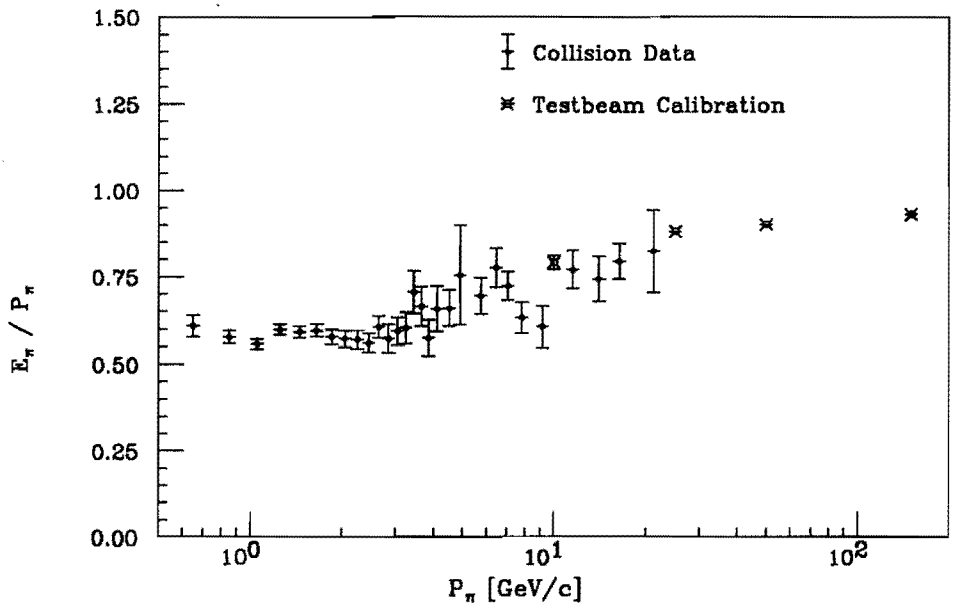

Figure 28: The ratio of the energy (electromagnetic + hadronic) observed in the calorimeter — using nominal testbeam calibrations — to the track momentum for isolated charged pions. The response at low energies is depressed. The fragmentation of jets (into charged and neutral hadrons) is such that this fall off in response results in an undermeasurement of jet energies by a factor of approximately 1.4 for low energy (30 GeV) jets.

field and not reach the calorimeters. Furthermore, the bending of charged particle tracks of less than 800 MeV or so will degrade the directional pointing information of the

calorimeter. Since the average W p_t in our sample is 5 GeV and since we limit the jet energies in the event (see Section 9.3), the particles in the underlying event will be of low energy; and our W mass measurement is sensitive to these effects. In order to compensate for calorimeter nonlinearities, we multiply $\not{u}$ by a factor $k_{\not{u}}^0 = 1.4$ [20]. This does not correct for magnetic field effects. It is difficult to deconvolve the two effects because we do not know *a priori* what part of the energy is due to recoil against the W (directed energy) and which is due to the randomly-distributed energy of underlying event from the spectator hadron. Scaling up the energy to fully compensate for the undermeasurement of the recoil results in an enhancing of the noise due to the random event underneath and a degradation of the measurement of the neutrino momentum. We thus correct only for the nonlinearities in the calorimeter. We will simulate any further effects in the Monte Carlo, where the effects on the recoil and random parts of the event can be separated. We will return to this choice of scale in Section 11.3.2 and discuss its effect on the W mass measurement in greater detail.

9 Event Selection

In this section we describe the selection criteria used to identify the $W \rightarrow \mu\nu$ decay candidates used in determining the W mass. We begin with an overview of the characteristics of W decay. W and Z decays are the primary source of charged leptons with transverse momenta above 20 GeV/c. The neutrino from W decay escapes the calorimeter without depositing any of its energy, producing an apparent transverse energy flow imbalance. The muon does the same, however, depositing on average only 2.3 GeV of its 35 GeV in the calorimeter. In the rest frame of the W, the muon and neutrino decay opposite each other. Since the average p_t of the W is small, the muon and neutrino will be nearly back-to-back in the lab frame. Thus, the missing energies of the two leptons effectively cancel each other, producing a small amount of transverse energy only approximately correlated with the neutrino direction. These characteristics of W decay are shown in Fig. 29 and

Fig. 30. The difference between the muon and neutrino is, of course, that we measure the muon momentum from its track. By extrapolating the track to the calorimeter, we measure its energy deposition in the calorimeter. We can then correct the raw missing transverse energy for the effect of the muon to extract the missing energy due to the neutrino. Thus, we can only look for large missing energy after full reconstruction of the muon track and not, for example, at the trigger level. We obtain a sample of $W \rightarrow \mu\,\nu$

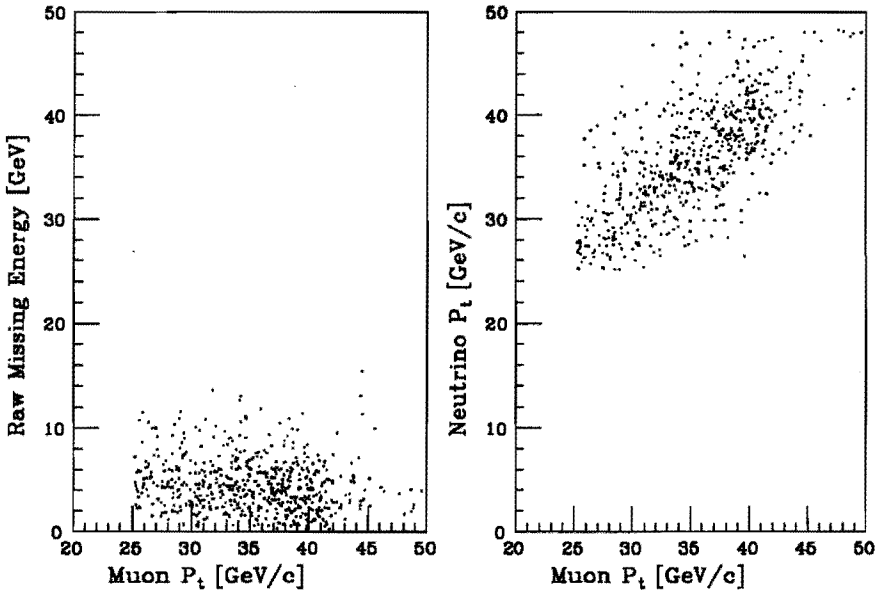

Figure 29: Muon transverse momentum versus a) the raw missing energy and b) the reconstructed neutrino transverse momentum in the $W \rightarrow \mu\,\nu$ decay sample used in this analysis. The muon and neutrino transverse momenta are approximately equal and back-to-back (see Fig. 30). Because the muon deposits only a minimum of its energy while passing through the calorimeter, there is little such correlation between muon momentum and raw missing energy.

decays by looking for events with a high transverse momentum muon accompanied by large missing energy. The topology of a typical W decay in the tracking chambers is shown in Fig. 31 and in the calorimeters in Fig. 32.

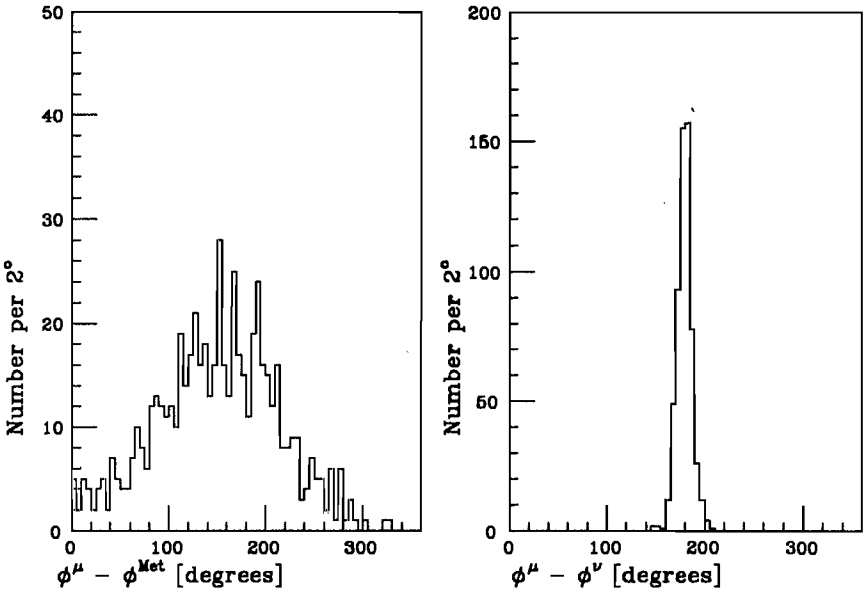

Figure 30: Muon azimuth versus a) azimuth of the raw missing energy vector and b) the azimuth of the reconstructed neutrino in the $W \rightarrow \mu\,\nu$ decay sample. The muon and neutrino are back-to-back. The correlation between muon momentum and raw missing energy is less apparent.

9.1 Selection of an Inclusive, High p_t, Muon Sample

We first selected a inclusive sample of events containing high p_t muons. We used the same fast, 2-dimensional track reconstruction algorithm used in the level 3 trigger to select events containing a track with transverse momentum above 20 GeV/c [36]. If the results of the level 3 analysis were written to tape, we used this information; if not, the events were reanalyzed. Events containing a muon with p_t above 20 GeV/c were analyzed by the full CDF offline analysis package, and those with a muon candidate of $p_t \geq 20$ GeV/c which deposited less than 10 GeV of energy in the calorimeter were kept for further analysis. At this stage, a muon was defined to be a match, $\Delta X < 10$ cm, between a track in the CTC and a track in the muon chambers. This sample contained 10 385 events.

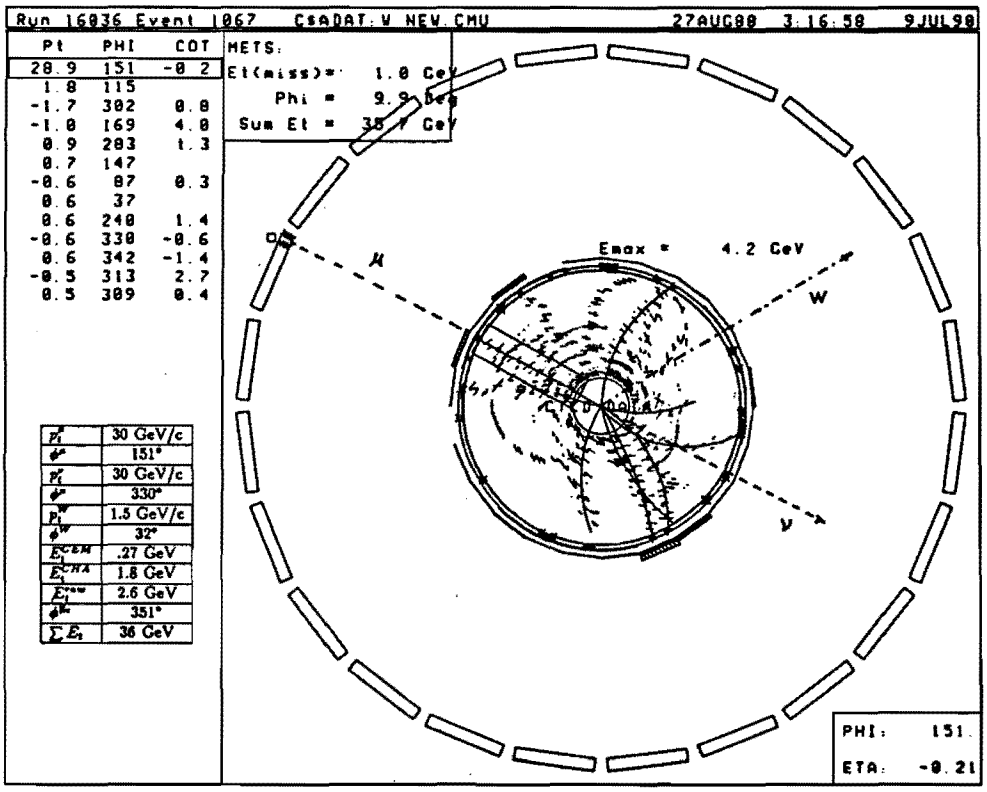

Figure 31: CDF graphics display of a typical W decay to muon and neutrino showing the tracks in the detector plane transverse to the beam. The tracks in both the CTC and muon detector are shown. Reconstructed neutrino and W tracks are superimposed. Notice that the muon and neutrino are nearly back-to-back as the W has very little p_t (1.5 GeV). Calorimeter energy summed over η is also shown. Energy deposition in the calorimeter as a function of η and ϕ is plotted for this event in Fig. 32.

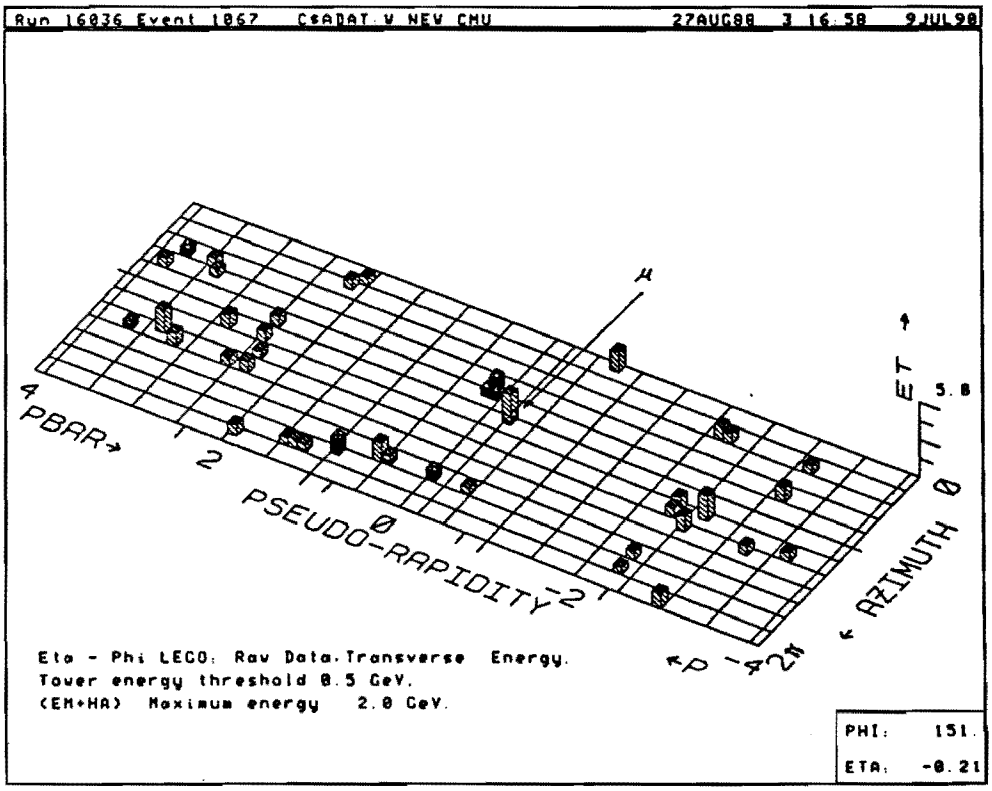

Figure 32: Energy deposition in the detector for the W decay of Fig. 31. The transverse energy deposited in the electromagnetic and hadronic calorimeter in each tower is plotted as a function of η and ϕ.

9.2 W Decay Backgrounds

The backgrounds in W decay events can be classified in either of two ways. The first classification divides them into 1) real muons from processes other than W decay and 2) fake muons. The more illuminating classification for this analysis is not to consider whether the muons are "real" or not but to concentrate on how they effect the transverse mass and momentum spectra we will use to determine the W mass. We thus divide the background into: 1) muons (real or fake) from processes with rapidly falling p_t spectra, and 2) muons from processes producing high pt muons.

A background of the first type comes from the sequential decay of $W \rightarrow \tau\,\nu$, where the τ subsequently decays into a muon. The transverse mass[7] spectrum for the decay of such τs is given in Fig. 33.

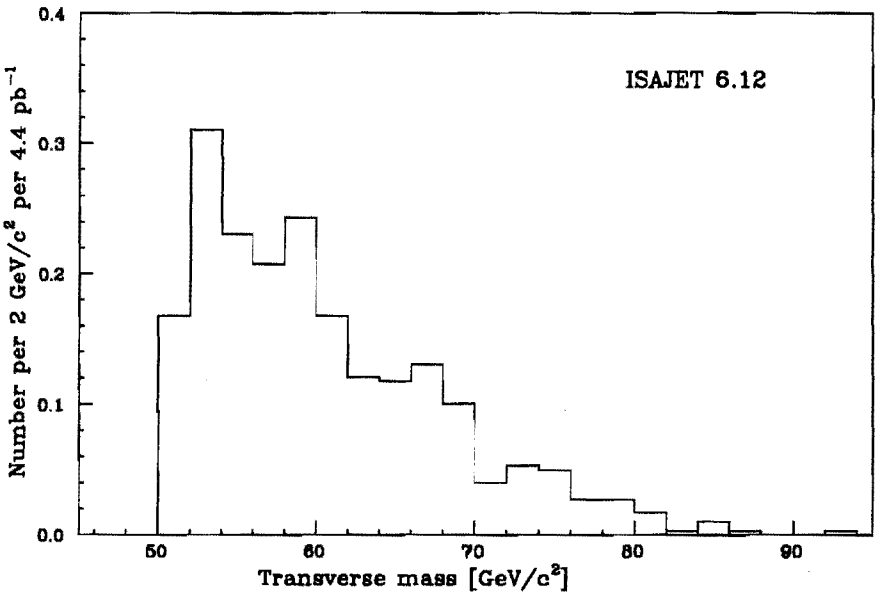

Figure 33: The transverse mass spectrum of the electron and reconstructed neutrino system in simulated sequential decay events: $W \rightarrow \tau\,\nu$ where the τ decays to an electron. This was generated with the ISAJET(V6.12) [37] $\bar{p}p$ simulation. This spectrum differs little if the τ decays to a muon.

A second low p_t background comes from charged pions (*QCD* background). There are

[7]Transverse mass is defined in Equation 13.

approximately 5 hadronic absorption lengths in front of the muon chambers. Energetic pions can "punch through" the calorimeter without depositing all their energy and create a track in the muon chambers. The background from "interacting" punchthrough can be identified by the excess above the minimum ionizing particle energy deposition characteristic of the muon (Fig. 34). The shape of the p_t spectrum of pions contaminating the inclusive muon sample can be identified by looking at those particles with energy

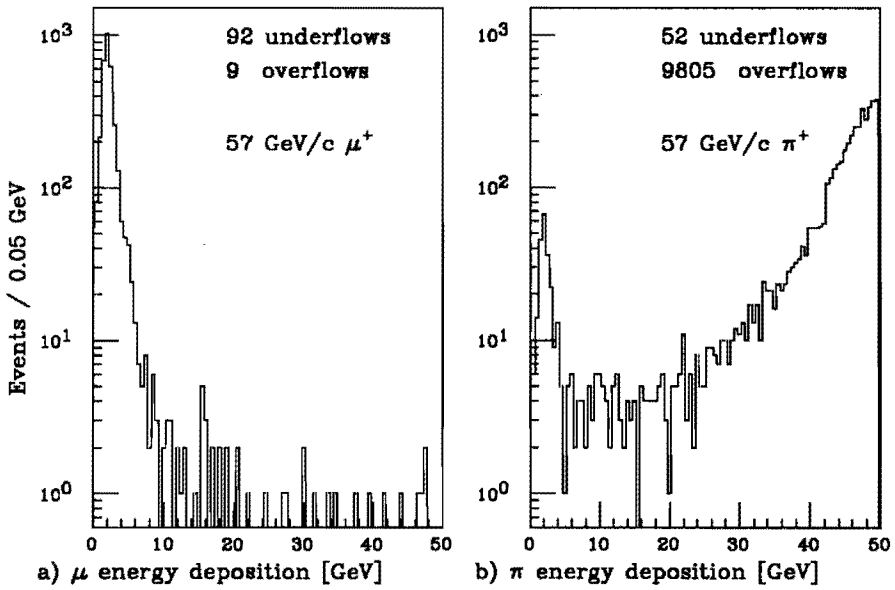

Figure 34: Energy deposited in the CDF calorimeters by a) a 57 GeV/c muon testbeam and b) a 57 GeV/c pion testbeam [29]. The low energy peak of minimum ionizing particles in b) contains the non-interacting pion background. This peak also contains the 3-4% background of muons which contaminate the pion testbeam.

depositions well above the minimum ionizing peak (Fig 35). This is the background from interacting punchthrough. Non-interacting punchthrough is harder to remove. These are pions which leave a minimum ionizing signature in the calorimeters. To remove this background, one uses the fact that the most probable source of energetic pions are jets. Most of these jets will be accompanied by a jet back-to-back in the transverse plane. In Fig. 36 is plotted the p_t spectrum for those "muons" which have a jet above 5 GeV within 30° of back-to-back with the muon azimuth. The shape of the spectrum is roughly the

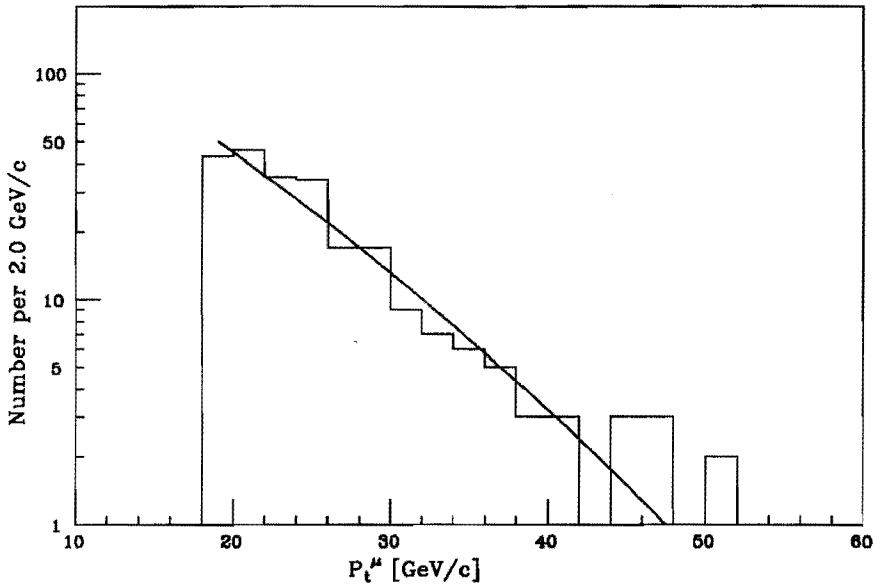

Figure 35: p_t spectrum for "muons" with a total energy deposition in the calorimeters greater than 6 GeV. This is the background from pions which interact in the calorimeter before reaching the muon chambers. Overlaid is the fit of an exponential function to the spectrum.

same as for interacting punchthrough. A typical punchthrough event is shown in Fig. 37.

The high p_t muon background comes mainly from $Z \rightarrow \mu\mu$ decays and cosmic rays (see Fig. 38) which cross the detector in time with $\bar{p}p$ collisions. They can be separated from W decays by identification of both muons from the decay or both legs of the cosmic ray. A typical cosmic ray is shown in Fig. 39. Removing these events is trivial. However, not all cosmic rays and Zs will have both tracks reconstructed. If one of the legs of the Z goes very forward or backward in the detector, it can pass through too few layers of the CTC to allow reconstruction of the track. The same is true of cosmic rays that traverse the detector at a large polar angle (see Figures 40 and 41). We limit the likelihood of this occurring by requiring the z vertex of the interaction to be central in the detector: $| z_{vertex} | < 60$ cm. A further consideration for cosmic rays is that the hit-timing data will be different from that of tracks from $\bar{p}p$ interactions. Not only is the cosmic ray somewhat

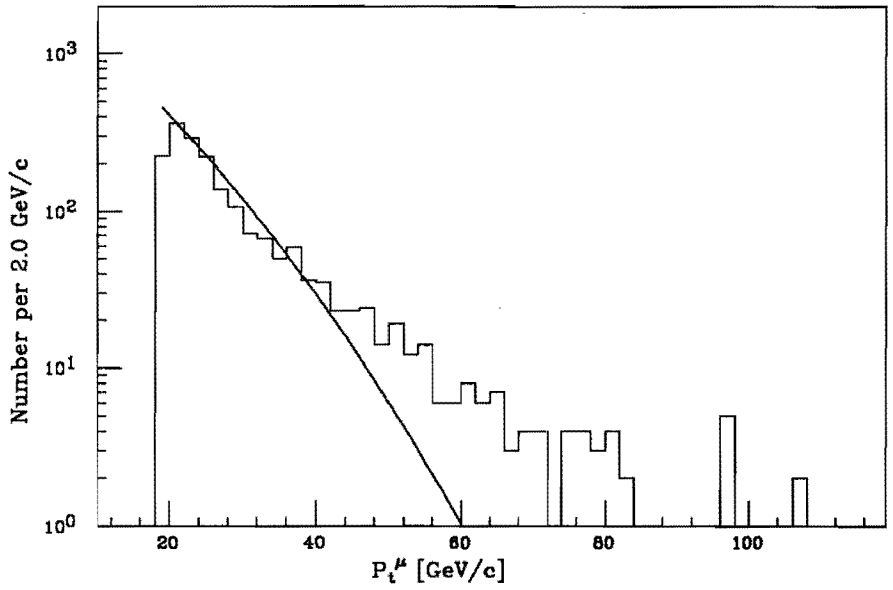

Figure 36: p_t spectrum for muons with a jet above 5 GeV of transverse energy within 30° opposite the muon azimuth. The spectrum for interacting punchthrough is superimposed. The shape of the two spectra are the same at low momenta. At higher momenta, there are relatively more real muons in the sample.

out-of-time with interactions from the $\bar{p}p$ collision; but on half of its trajectory, it will also seem to be going backward in time – one of the two legs will be approaching the interaction point. For these reasons the track may not be reconstructed as well as typical tracks. To find the second leg of a cosmic ray, we relax our criteria for what constitutes a good track. We will typically find that one leg of the cosmic ray will be reconstructed only in the R-ϕ plane, as the more difficult, 3-dimensional reconstruction fails (see Fig. 40).

In the next section we discuss the cuts we apply to the inclusive muon sample described previously to remove these backgrounds and identify a sample of $W \rightarrow \mu\,\nu$ events for measuring the W mass.

9.3 W Mass Sample

To select high quality candidates for $W \rightarrow \mu\,\nu$ decays, we make the following cuts on the inclusive muon sample described in Section 9.1. The muon and neutrino momentum

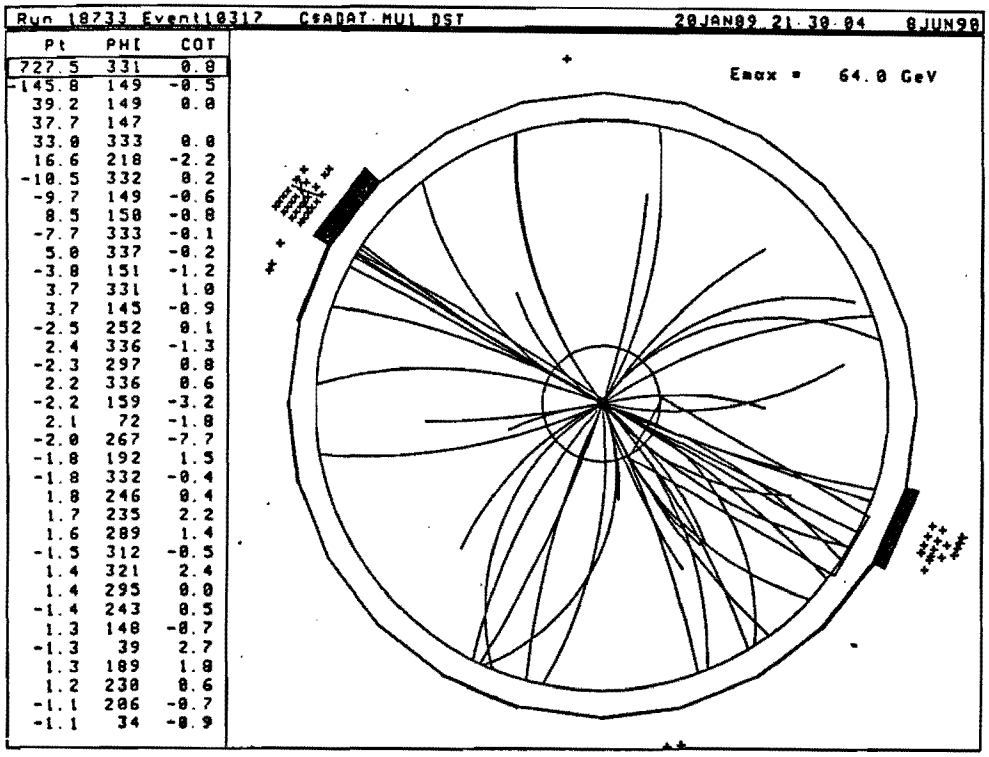

Pt	PHI	COT
727.5	331	0.0
-145.8	149	-0.5
39.2	149	0.0
37.7	147	
33.0	333	0.0
16.6	218	-2.2
-10.5	332	0.2
-9.7	149	-0.6
8.5	158	-0.8
-7.7	333	-0.1
5.0	337	-0.2
-3.8	151	-1.2
3.7	331	1.0
3.7	145	-0.9
-2.5	252	0.1
2.4	336	-1.3
-2.3	297	0.8
2.2	336	0.6
-2.2	159	-3.2
2.1	72	-1.8
-2.0	267	-7.7
-1.8	192	1.5
-1.8	332	-0.4
1.8	246	0.4
1.7	235	2.2
1.6	289	1.4
-1.5	312	-0.5
1.4	321	2.4
1.4	295	0.0
-1.4	243	0.5
1.3	148	-0.7
-1.3	39	2.7
1.3	189	1.8
1.2	230	0.6
-1.1	206	-0.7
-1.1	34	-0.9

Figure 37: A di-jet event. Pions in both of the jets have punched through the calorimeter to the muon chambers. In one of the jets, a track in the muon chambers has been matched to a high p_t track in the CTC. The two jets have transverse energies of 54 and 73 GeV. They are separated in ϕ by 179°. The muon p_t is 146 GeV/c.

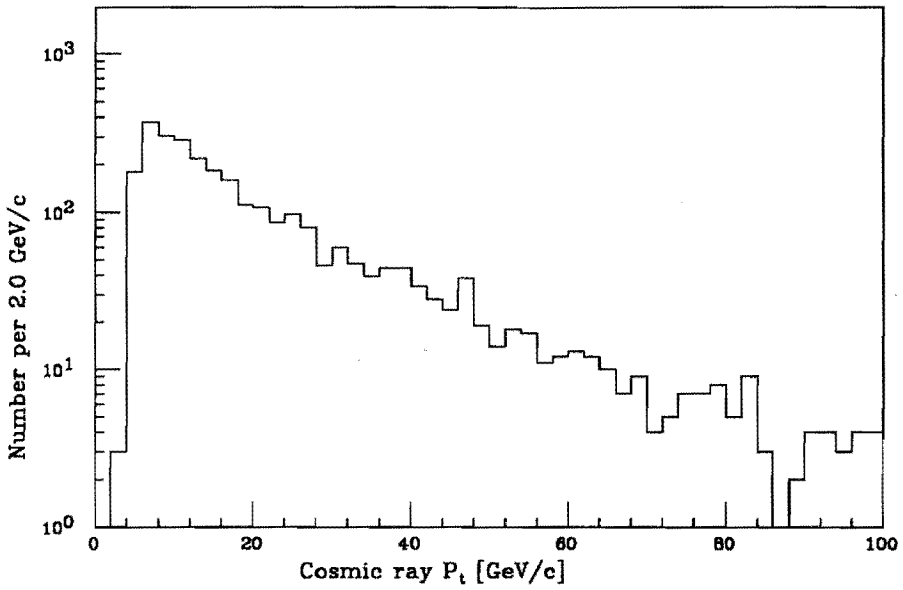

Figure 38: Transverse momentum spectrum of cosmic rays. These cosmic rays are from data taken using a trigger requiring a coincidence of hits in superlayers 0 and 2 of the CTC and a hit cluster in the Central Drift Tube array [38]. (This is the CDT-CFT level 0 trigger described in Appendix B.) No other trigger requirement was made.

spectra for the inclusive events are plotted in Fig. 42.

The distance, ΔX (plotted in Fig. 43 for inclusive muons), between the intercept of the extrapolated CTC track and the muon stub at the lowest plane of muon chamber sense wires is computed. (X=0 is defined as the midpoint of the three chambers in a wedge.) The expected mismatch due to multiple scattering for 110 cm of steel equivalent is $\sigma_{\Delta X} = \frac{12}{P}$ cm, where P is the particle momentum in GeV/c [25]. For a track of 25 GeV/c, $\sigma_{\Delta X}$ is 0.5 cm. We make a loose matching requirement that $\Delta X \leq 1.5$ cm.

The energy deposited by muons selected for the inclusive sample is plotted in Fig. 44. Having made significant improvements in the measurements of the muon track and calorimeter energy, we impose a stricter cut on the energy deposited in the calorimeter tower pointed to by the muon track. We require less than 3.5 GeV of total energy in this tower. The analysis of candidates for J/Ψ decays to muons show that 95% of

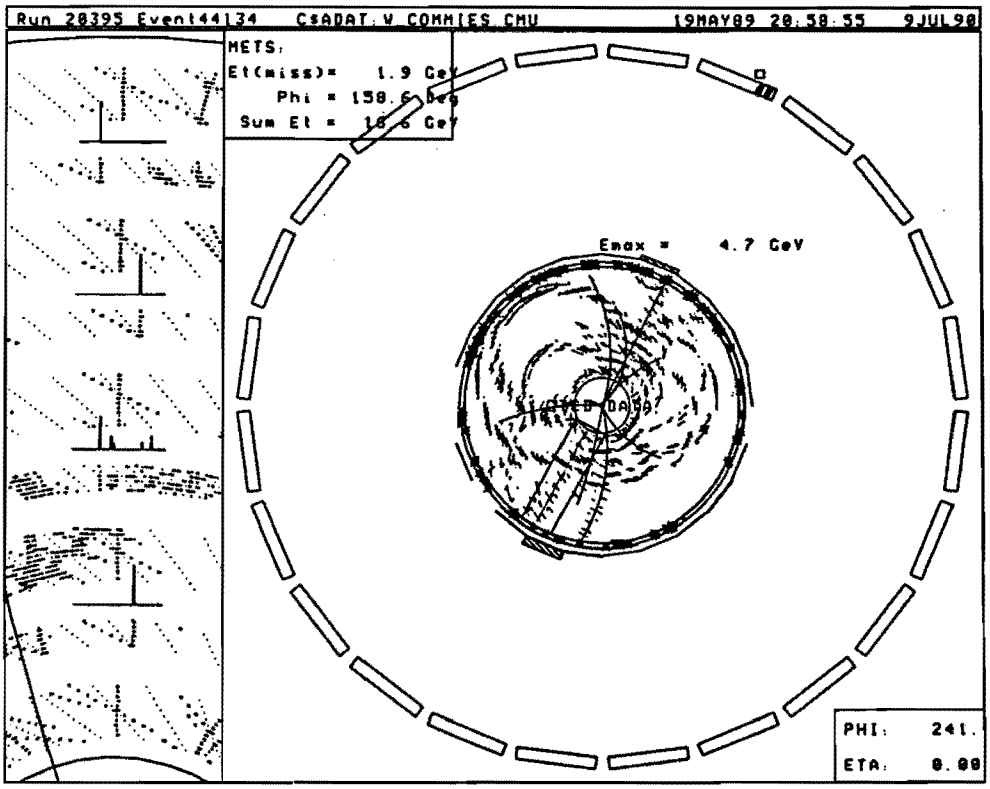

Figure 39: A typical cosmic ray in coincidence with a $\bar{p}p$ collision. Both the incoming and outgoing tracks were found. The outgoing track has no stereo reconstruction. (The track presumably entered from the top of the detector.) The insert on the left shows an enlarged view of the area circumscribed by the box in the main display.

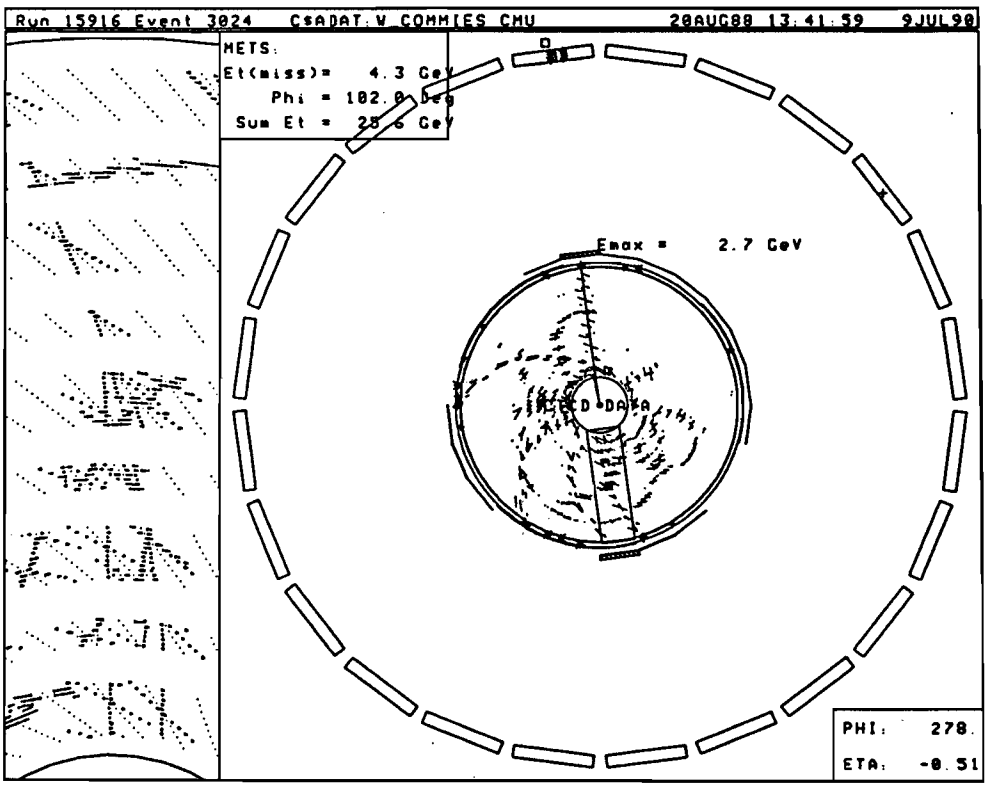

Figure 40: A cosmic ray with only one leg reconstructed, faking a W decay. Only one leg was found because of the minimal number of wire layers in the CTC through which it passed. From the insert on the left, we see that the track traversed only the first five superlayers of the CTC. An R-z view of this event is shown in Fig. 41.

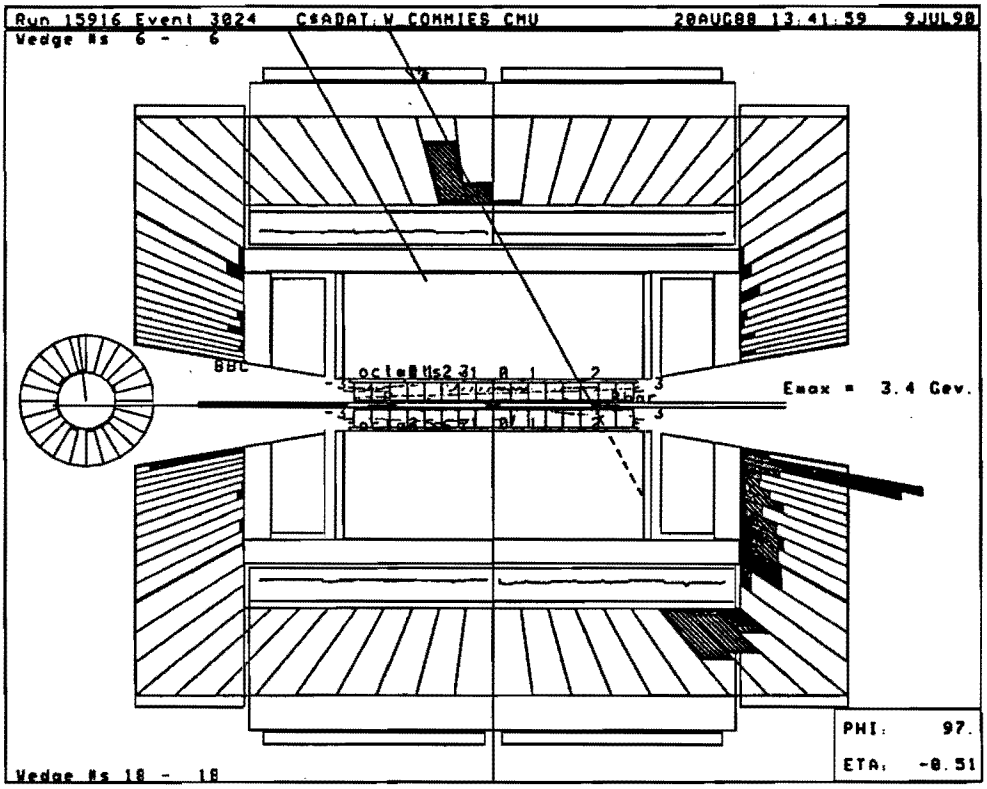

Figure 41: A side view of the cosmic ray shown in Fig. 40. The track passed through so few layers of the CTC due to the large polar angle with which the cosmic ray passed through the detector and the large z at which it crossed the beam axis.

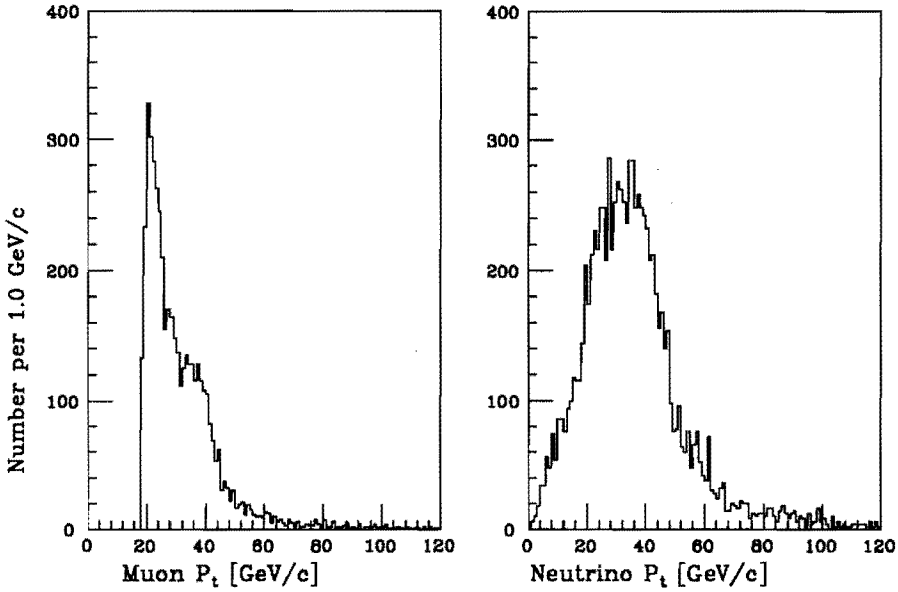

Figure 42: a) The muon transverse momentum distribution in the inclusive muon sample. b) The distribution of neutrino transverse momenta reconstructed in the sample. Not all these events contain a real neutrino.

all muons will pass these cuts (see Fig.15).[8] This eliminates the pion background from interacting punchthrough described in Section 9.2. To remove the background from non-interacting punchthrough, we reject events with jets of E_t greater than 5 GeV within 30° of back-to-back in azimuth with the muon track, believing the "muon" to be an energetic pion.

The cosmic ray and $Z \rightarrow \mu\mu$ background is removed by the following cuts. To reduce the probability that the second leg of a $Z \rightarrow \mu\mu$ decay or cosmic ray passes through too few layers of the CTC to be reconstructed, we accept only events with a z vertex within 60 cm (2σ) of the nominal $p\bar{p}$ interaction point (see Fig. 10). We also require the muon track to pass within 2.5 mm of the event primary vertex in the transverse plane. We eliminate events with more than one track with p_t greater than 15 GeV/c. This will eliminate most of the cosmic rays. We recognize that some fraction of the cosmic rays will not

[8]We measure the efficiency of this cut with the J/Ψ sample. For testbeam muons, 95% of all muons are below 5 GeV [29]. The discrepancy between the two numbers is most likely due to the pion contamination of the testbeam, which increases the number of events in the tail of the distribution.

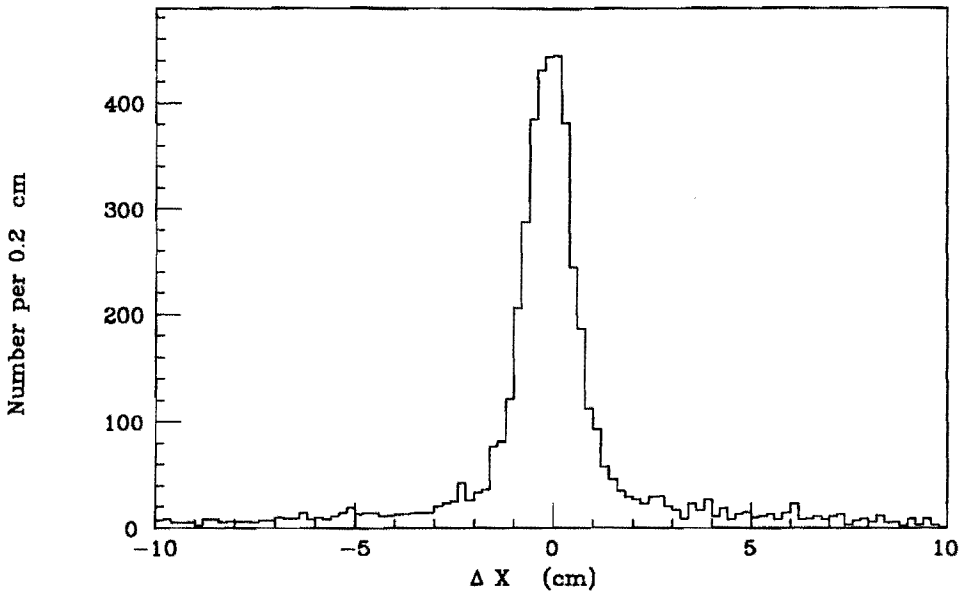

Figure 43: The match between the CTC and muon chamber tracks in R-ϕ for the inclusive sample of high p_t muons.

have two 3-dimensional track reconstructed. If the cosmic ray is sufficiently out-of-time with the rest of the event, it is possible that the track reconstruction algorithm will not reconstruct the track in stereo. This will also occur when the track passes through too few stereo layers of the CTC to permit full 3-dimensional reconstruction. The latter is true of tracks in Z decays as well as cosmic rays. We allow for these pathologies by relaxing our track quality criteria and looking for a track back-to-back with the muon. We do not require full stereo reconstruction for these tracks, only that the track be reconstructed in the R-ϕ view. We match only the ϕ angle of the two tracks and make a minimal p_t requirement for the back-to-back track, recognizing that the momentum and charge of the second track may not be accurately determined. Thus, we reject events with a track of p_t greater than 10 GeV/c within 3° in ϕ of the direction opposite the muon. As additional protection against pathologies in tracking, we make two additional cuts. First, we remove events with two muon stubs consistent with a cosmic ray. These stubs must have opposite slope and point at the same vertex. Second we require that the vertex of

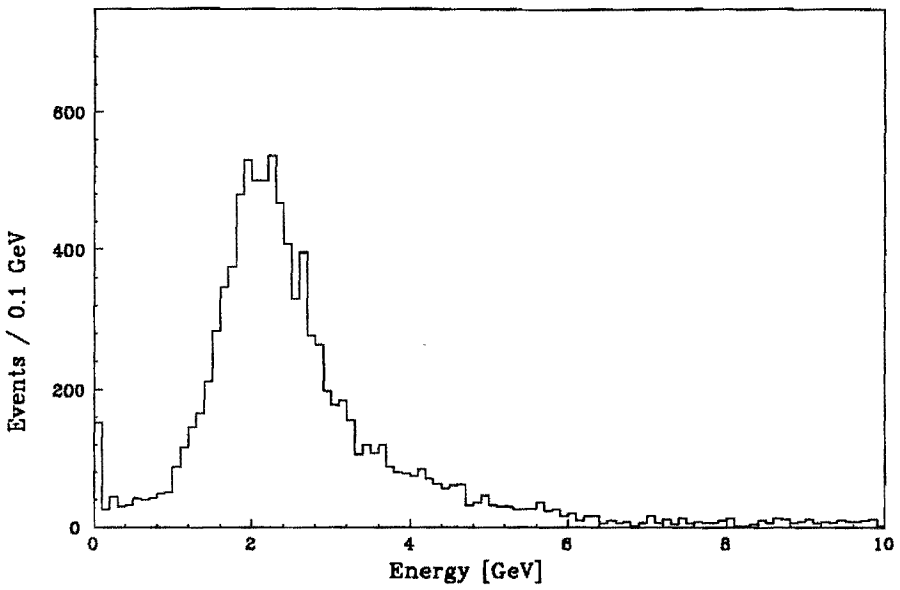

Figure 44: Total (electromagnetic + hadronic) energy deposited in the central calorimeters by muons in the inclusive muon sample.

the event as determined by the VTPC have track multiplicity greater than two. This removes cosmic rays which do not overlap with a $\bar{p}p$ interaction vertex. These cuts for removing cosmic rays and Zs are not exclusive. Events which fail one cut will probably fail others. However, high p_t muons from these processes could have a substantial impact on this analysis, and we wish to remove as many of them as possible. We will estimate of size of the remaining background and its effect on the W mass measurement in Section 15.2.

The calorimeter measurement of $\not\!\!E_t$ is a major component of the overall measurement resolution. We restrict ourselves to more accurately measured, relatively clean events by requiring no calorimeter energy cluster above 7 GeV (before applying k_ν^0 to correct for calorimeter nonlinearities). This also simplifies the simulation of W decays, as we do not need to model the response of the calorimeter to high energy jets. The distribution of jet energy for the inclusive muon sample is shown in Fig. 45.

Finally, to reduce backgrounds at low p_t, we require p_t^μ and and $p_t^\nu \geq 25$ GeV/c. This removes some real W candidates but far more background. Furthermore, as we shall

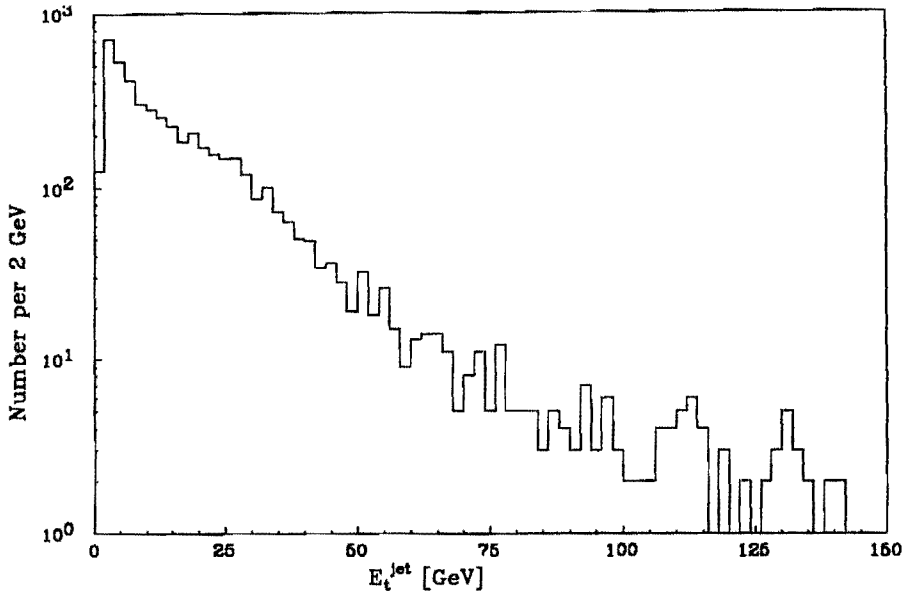

Figure 45: The jet raw E_t spectrum associated with inclusive muons. High energy jets in these events degrade the resolution of the measured neutrino momentum. We remove all events with jets above 7 GeV of E_t. Our jet clustering threshold is about 5 GeV.

learn in the next section, it is the peak and falling edge of the Jacobian in the kinematic distributions that constrains the W mass. The low transverse mass Ws removed by this cut will not significantly change the measured value of the W mass.

The cuts used in selecting the W mass sample are summarized in Table 3. In our discussion of the event selection above, we grouped the cuts logically by the type of background they were intended to remove. Chronologically, they were imposed in two passes. We first selected an initial sample of W decay candidates from the inclusive muon sample with cuts 1-5 and 10 (as identified in Table 3). After studying this sample, we imposed additional cuts to remove residual Z decay and cosmic ray backgrounds (cuts 6-9) and a p_t cut of 25 GeV/c for both muon and neutrino. The fraction of events removed by the cuts and the overlap between cuts is summarized in Table 4 for those cuts which were used to select the initial W decay sample.

We are left with 592 $W \rightarrow \mu\ \nu$ decay candidates. We will discuss the size of the remaining background in this sample and and its effect on the W mass measurement in

	Cut	Description
1	Track match	$\Delta X < 1.5$ cm
2	Remove QCD background	Total energy < 3.5 GeV in the muon tower
3		No jet of $E_t > 5$ GeV within 30° opposite ϕ^μ
4	Veto Z^0s and cosmics	One and only one 3-d track with $p_t > 15$ GeV/c
5		CTC impact parameter < 2.5 mm
6		$\mid z_{vertex} \mid < 60$ cm
7		No track of $p_t > 10$ GeV/c within 3° opposite ϕ^μ
8		No two muon chamber tracks consistent with a cosmic ray or Z
9		VTPC vertex track multiplicity > 2
10	Clean sample	No jet of $E_t > 7$ GeV
11	Remove low p_t background	$p_t^\mu > 25$ GeV/c, $p_t^\nu > 25$ GeV/c

Table 3: Cuts used to select a W decay sample.
Cuts used in the selection of $W \rightarrow \mu\nu$ decay candidates for measuring the W mass. Cuts 6-9 were applied to remove residual cosmic rays and Z decays after studying the sample selected by the other cuts.

Section 15.2.

10 Analysis

As was discussed in Section 7, the longitudinal component of the neutrino momentum is not measured; and this analysis is carried out entirely in the plane of the detector transverse to the beam. The mass and width of the W are found by comparing distributions of kinematic variables in the W candidate sample to Monte Carlo predictions of these distributions for different masses and widths of the W. The following transverse-plane variables are used: transverse momentum of the muon and neutrino, and transverse mass of the muon-neutrino system:

$$p_t^\mu, \qquad p_t^\nu, \qquad m_t \equiv \sqrt{2p_t^\mu p_t^\nu [1 - cos(\phi^\mu - \phi^\nu)]} \quad . \tag{13}$$

All three of these distributions exhibit the Jacobian shape characteristic of W decays (see Section 3). The upper edges of the distributions are constrained by the mass of the

4	3	10	1	2	5	Events	Fraction (%)
						10385	100
X						5007	48.2
	X	X				1635	15.7
	X	X		X		1619	15.6
	X	X	X			1388	13.4
X	X	X				1174	11.3
			X	X	X	2746	26.4
X			X	X	X	2252	21.7
X	X		X	X	X	1350	13.0
X		X	X	X	X	945	9.1
	X	X	X	X	X	1134	10.9
X	X	X	X	X	X	892	8.6

Table 4: This matrix summarizes the effect of the cuts made in selecting the W decay sample. A X indicates use of the cut. Cuts are identified by their position in Table 3. Since cuts 6-9 and 11 were applied after selection of an initial sample, they are not included.

W. There is no corresponding constraint on the lower edges of the distributions which reflect the fraction of W momentum in the longitudinal direction. Thus, most of the sensitivity of the comparison between data and Monte Carlo is in the position of the peak of the Jacobian and the slope of the falling edge above the peak (see Fig. 46). The width of the distribution reflects several effects, among them parton distribution functions and detector resolution. In addition, the width of the p_t spectra is smeared by the p_t of the W. (High p_t leptons come from the boost imparted to them by high transverse momentum Ws.) The p_t spectrum of the W is determined by initial state radiation. In our particular sample of W decays, it depends on the specific cuts made in selecting the sample. Our removal of events with jets of energy greater than 7 GeV is a *de facto* cut on the p_t of the W. We take the p_t for the Monte Carlo from that given in the data, but we recognize that the computation of p_t^W is relatively poor, mostly due to the poor resolution of the neutrino momentum measurement. The m_t spectrum has the advantage that to first order it is unaffected by p_t^W [39]. We will determine m_W from

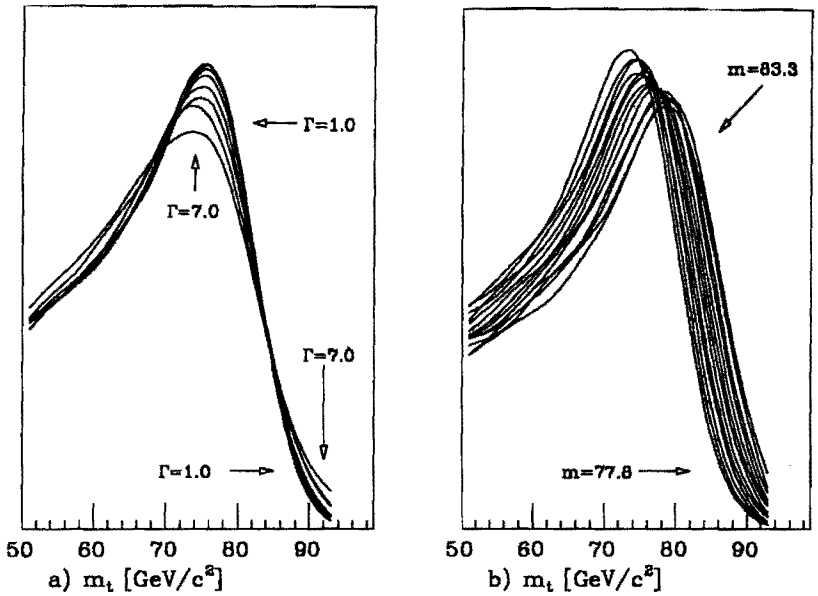

Figure 46: The predicted m_t distribution for a) several choices of m_W with Γ_W = 2.250 GeV and b) several choices of Γ_W with m_W = 79.8 GeV/c^2. Nominal parameter values were used in the simulation described in Section 11; 200 000 events were generated. Note the dependence of the peak of the distribution on m_W and the slope of the falling edge on Γ_W.

the comparison of the m_t distribution in the data to the Monte Carlo and regard the comparison of the p_t spectra as consistency checks.

We generate Monte Carlo predictions of the distributions of m_t, p_t^μ, and p_t^ν for various combinations of mass, m_W, and width, Γ_W, of the W. Predictions are generated at masses between 77.8 and 82.3 GeV/c^2 in steps of 0.5 GeV/c^2 and at widths between 0.375 and 2.250 GeV in steps of 0.375 GeV and between 2.25 and 6.00 in steps of 0.75 GeV (see Fig. 47). A total of 374 000 000 events were generated, 3 400 000 at each m_W, Γ_W combination. This would have been impossible using a Monte Carlo which includes a full detector simulation. Not only did we generate over 10^8 events, but we also did this several times as our understanding of the analysis increased. In addition, we went through many iterations that involved smaller numbers of events to study the systematics of the model. This required a fast Monte Carlo – one in which we could change parameters and get

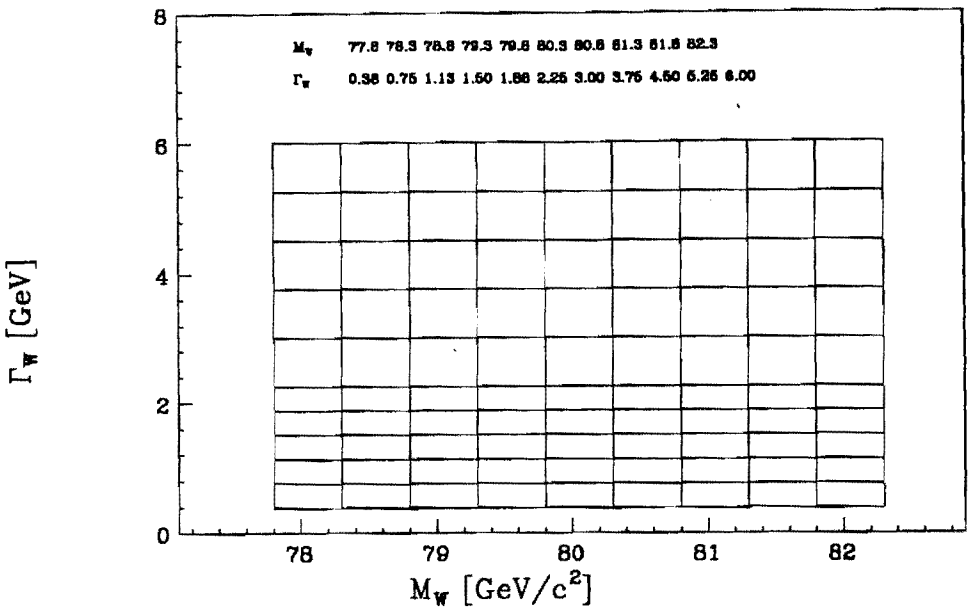

Figure 47: The mass-width fitting grid. Monte Carlo predictions of the distributions of m_t, p_t^μ, and p_t^ν were generated using as inputs m_W and Γ_W at each grid point.

immediate feedback. The simulation we used is the topic of the next section.

11 Simulation of W Production and Decay

We use Standard Model predictions for the production of Ws in $\bar{p}p$ collisions and their subsequent decay to leptons. We then simulate the response of the detector to these decays in the measurement of the muon and neutrino transverse momenta. The description of the Monte Carlo lends itself to division into two parts. We first generate Ws from the quarks and antiquarks in the proton and antiproton and decay the Ws thus produced into muon-neutrino pairs. At this point we are left with the four-vectors of the leptons in the laboratory frame of reference. We then include resolution-like effects. We adopt a relatively simple phenomenological model for how the detector responds to real leptons and hadrons. Perhaps more importantly, the parameters of the model can be constrained by our $\bar{p}p$ data. We include sufficient degrees of freedom to reflect the relevant uncertainties in W generation and detector response. We include various parton distribution

functions, the non-zero p_t of the W, the varying event vertex, detector geometry, the resolution of the measurement of the track momentum, the response of the detector to the uncorrelated event due to spectator hadrons and the directed energy flow of the recoil against the W, and the net energy balance in the event. We will discuss each of these degrees of freedom, the constraints which may be applied, and the systematic effects on the W mass they entail.

11.1 Generation and Decay of Ws

The Monte Carlo program generates W decays to muons from the lowest-order QCD production process:

$$q\overline{q'} \rightarrow W. \tag{14}$$

The program includes the W polarization in the decay

$$W \rightarrow \mu\,\nu. \tag{15}$$

A general discussion of the production and decay of Ws was given in Section 3; specific details are given here. The simulation begins by generating the W rapidity, mass and polarization distributions for the mass, m_W, width, Γ_W, and parton density being simulated. Parton density is discussed in Section 12.1. The rapidity distribution reflects the fraction of momentum which is longitudinal, which in turn reflects the the parton distribution functions used to model the initial $\bar{p}p$ collision (see Equation 5). The mass distribution reflects the convolution of the parton luminosities (Equation 8) with an approximately [40] relativistic Breit-Wigner line shape:

$$\frac{dn}{dm_W} \sim \frac{s}{(s-m_W^2)^2 + s^2\Gamma_W^2/m_W^2}. \tag{16}$$

To reduce the time required to simulate W production, we model only that part of the Breit-Wigner that is within seven total widths (Γ_W) of each nominal W mass. This is an adequate modelling of the total shape. The polarization distribution (see Section 3)

includes W^+s coming from u quarks in the antiproton (or W^-s from $\bar{u}$ quarks in the proton) which have the opposite helicity of the more plentiful W^+s coming from u quarks in the proton. This was discussed in Section 3. From these distributions, rapidity, y_i, mass, m_i, and polarization, P_i, are chosen for the W by rejection. The decay angle of the muon ($\hat{\theta}_i$), in the rest frame of the W, is generated according to a $(1 + P_i \cos\hat{\theta}_i)^2$ distribution. Finally a random decay azimuth, $\hat{o}_i$, is generated. The muon and neutrino four-vectors in the laboratory frame are calculated from m_i, y_i, $\hat{\theta}_i$ and $\hat{o}_i$.

11.2 Finite p_t^W

Higher order diagrams for the creation of the W (see Fig. 3) give the W a non-zero p_t. This "initial-state" radiation of one or more gluons imparts a component of transverse momentum to the quark which it will then pass on to the W created by its annihilation. These processes are calculable in the context of *QCD* theory. However, we have for other reasons (discussed in Section 9.3) limited ourselves to a sample of Ws with small p_t, where these *QCD* calculations break down [41]. The p_t of the W and the detector resolution both act to broaden the width of the kinematic distributions. Detector effects are at least as large an effect as the W p_t. We treat the p_t^W used in our simulation phenomenologically. We choose as a basis for the p_t^W the distribution found in our data sample. To reduce the effects of statistical fluctuations in the data, we use the distribution found in the larger sample of $W \rightarrow e\,\nu$ decays and assume that Ws in the $W \rightarrow \mu\,\nu$ decays are similar. We parametrize the distribution

$$\frac{dn}{dp_t^2}(p_t^2)$$

as a sum of exponentials (see Fig. 48). We sculpt the distribution (equivalent to adding a few events in the tail) so that when it is used as the input to the simulation the p_t^W distribution reconstructed in the Monte Carlo agrees with the distribution in the data. We are not making a measurement of p_t^W, only requiring internal consistency between our model and the data. The systematic uncertainty this procedure introduces in the W

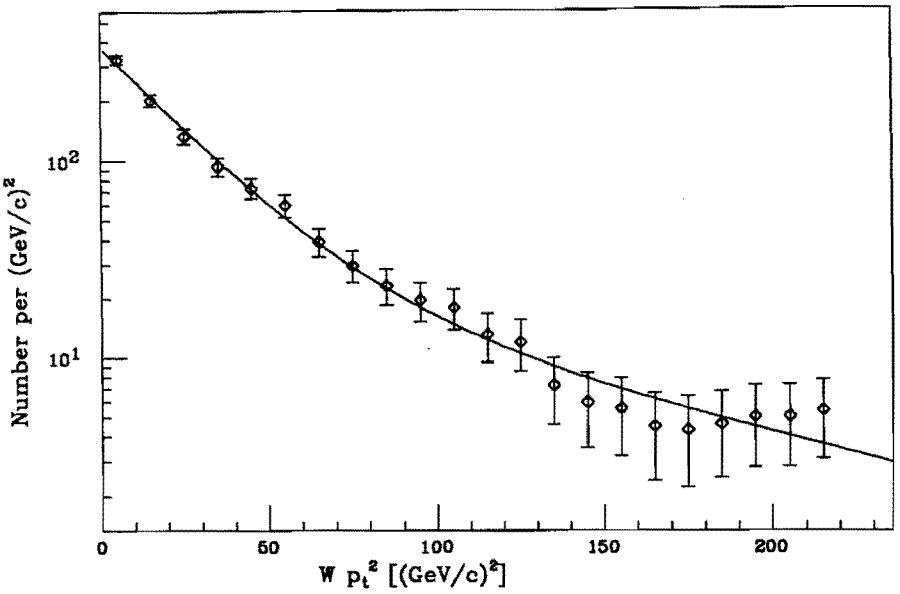

Figure 48: The distribution of $\frac{dn}{dp_t^2}$ found in the $W \rightarrow e\,\nu$ sample. The solid line is the parametrization of this distribution as the sum of two exponentials.
$\frac{dn}{dp_t^2} = A(e^{-b\,p_t^2} + e^{-c\,p_t^2})$

mass measurement is the subject of Section 12.2.

We choose from this distribution a random p_t^W for the Monte Carlo event and boost the leptons in the transverse plane accordingly.

11.3 Detector Response

A z vertex for the Monte Carlo event is chosen at random from a Gaussian distribution of sigma 30 cm truncated at $\pm$ 60 cm to agree with the distribution found in the data (see Fig. 10) and the cut imposed in selecting the sample of W decays. We propagate the muon from this vertex to the inner radius of the muon chambers where we determine if the muon hits the muon detector. We simulate only the detector's η coverage, assuming that there is no dependence of p_t on azimuthal angle in W decays. The fiducial cuts for the 90° crack and the limited η ($\mid \eta \mid < .63$) coverage effect the kinematical properties of Ws which produce a muon which entering the data sample. The p_t distribution is given

in Fig. 49 before and after fiducial cuts.

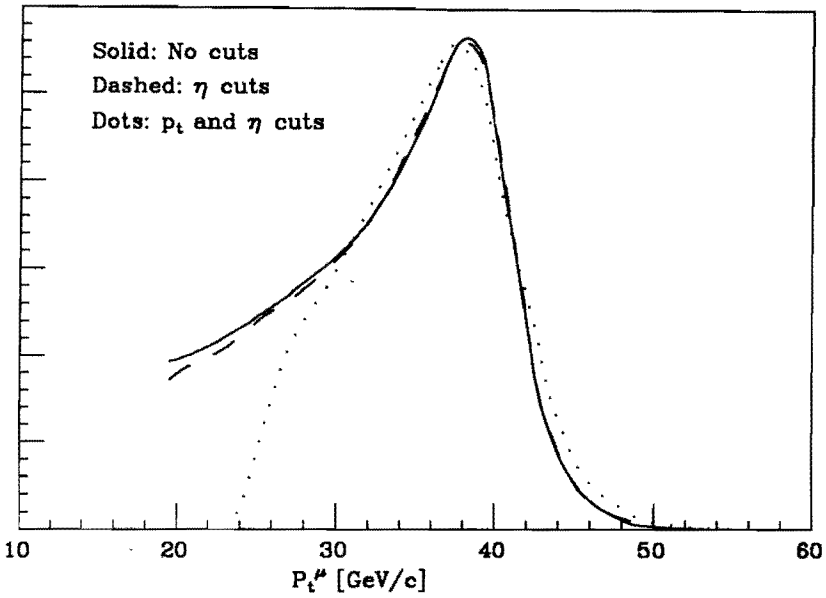

Figure 49: The shape of the p_t distribution before (solid) and after (dashed) fiducial cuts in the Monte Carlo. The fiducial cut changes the shape of the spectrum below 25 GeV/c. The p_t spectrum after simulating detector resolution and cutting at $p_t = 25$ GeV/c is also plotted (dots).

11.3.1 Resolution of the Muon Momentum Measurement

As discussed in Section 7, the resolution of the measurement of p_t in the CTC is described by $\frac{\sigma_{p_t}}{p_t^2} = 0.11\%$. Thus, the distribution of $1/p_t$ is described by a Gaussian of sigma 0.0011 $(\mathrm{GeV/c})^{-1}$.[9] Given p_t^μ, we choose a random smearing factor $\delta(\frac{1}{p_t})$ from a gaussian of width 0.0011 and construct the p_t measured in the tracking chamber.

$$\tilde{p}_t = p_t^\mu + \frac{1}{\delta(\frac{1}{p_t})} \quad .$$

We assume that any mismeasurement of the muon azimuthal direction is negligible, as the CTC's pointing resolution is less than 0.5 mrad [42].

[9]This reflects the fact that the measurement made in the CTC is actually of curvature, k. ($k \sim \frac{1}{p_t}$.)

11.3.2 The Underlying Event Model

Our model of the detector response in the neutrino momentum measurement breaks down into three parts: 1) the directed energy flow of the recoil balancing the W p_t, 2) the uncorrelated event from spectator hadrons, and 3) the energy balance in the event with respect to the muon direction.

We begin with the p_t of the W. Momentum conservation requires that there be a balancing energy flow opposite the W in the transverse plane. We know that not all the energy of this "jet" will be measured by the calorimeter due to nonlinearities at low energy and the effect of the magnetic field on low momentum particles (discussed in Section 7). We simulate these effects with a p_t-dependent degradation factor $k_{\not p}$ (see Fig. 50). The coherent energy flow in the model, $\vec{p}_t^{\,jet}$, is given by Equation 17.

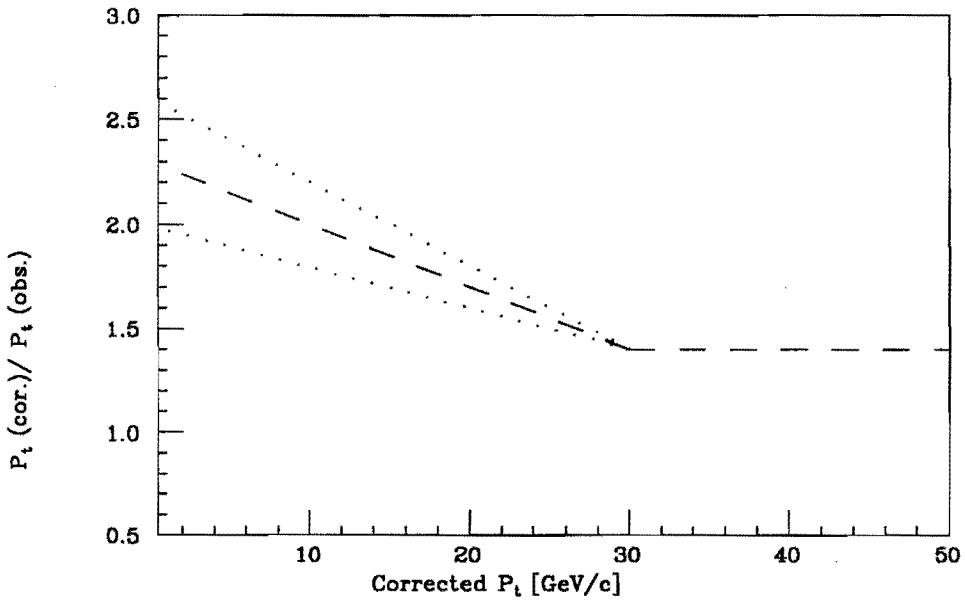

Figure 50: The degradation factor $k_{\not p}$ used in our model to simulate the effect of calorimeter nonlinearities and magnetic sweeping. Above 30 GeV/c we use a constant factor of 1.4 to account for calorimeter nonlinearities. The extrapolation to lower p_t is constrained by the measurement of the energy recoil in decays of Zs (see Section 12.2). The dotted lines indicate the upper and lower constraints on this factor from the Z data.

$$\vec{p}_t^{jet} = \frac{-\vec{p}_t^W}{k_\psi(p_t^W)} \quad . \tag{17}$$

We include the effect of the jet energy measurement resolution,

$$\sigma_{p_t^{jet}} = 0.85 \times \sqrt{p_t^{jet}} \quad , \tag{18}$$

by smearing the jet with a smearing factor taken from a Gaussian of width $\sigma_{p_t^{jet}}$ to get the first component of our underlying event, $\tilde{\vec{p}}_t^{jet}$.

For the uncorrelated event from spectator hadrons, we assume isotropic energy flow in the transverse plane, again due to momentum conservation. Thus, any anisotropy is due to random fluctuations in the calorimeter energy measurement, described by the resolution of the missing energy measurement. The resolution is studied in minimum-bias events and can be parameterized as a constant times the square-root of the total scalar transverse energy, $\sum E_t$, observed in the event as shown in Fig. 51:

$$\sigma_{\not\!\!E_{x,y}} = (0.47 \pm 0.01)\sqrt{\sum E_t} \quad . \tag{19}$$

We choose a $\sum E_t$ for the event from the distribution (Fig. 52) found in the W decay data. As with p_t^W, we use the distribution found in the more numerous $W \rightarrow e\,\nu$ sample. In order for this $\sum E_t$ to correspond to that found in minimum-bias events, we make two corrections on an event-by-event basis. We first remove the energy deposition of the electron from the raw $\sum E_t$. The $\sum E_t$ in W decays also contains a component due to the recoil energy against the W which is not present in minimum-bias events. We take the E_t associated with the recoil to be a factor of 1.4 larger than the reconstructed p_t^W to compensate for calorimeter effects (see Section 8, Fig. 53) and subtract $1.4 \times p_t^W$ from the raw transverse energy sum in making the distribution plotted in Fig. 52. Choosing a $\sum E_t$ from this distribution, we allow independent fluctuations, u_x, u_y, in the two transverse directions, taking the fluctuations from Gaussians of width $\sigma_{\not\!\!E_{x,y}}$ given by Equation 19, and construct the uncorrelated part of the underlying event:

$$\tilde{\vec{u}} = \vec{u}_x + \vec{u}_y \quad . \tag{20}$$

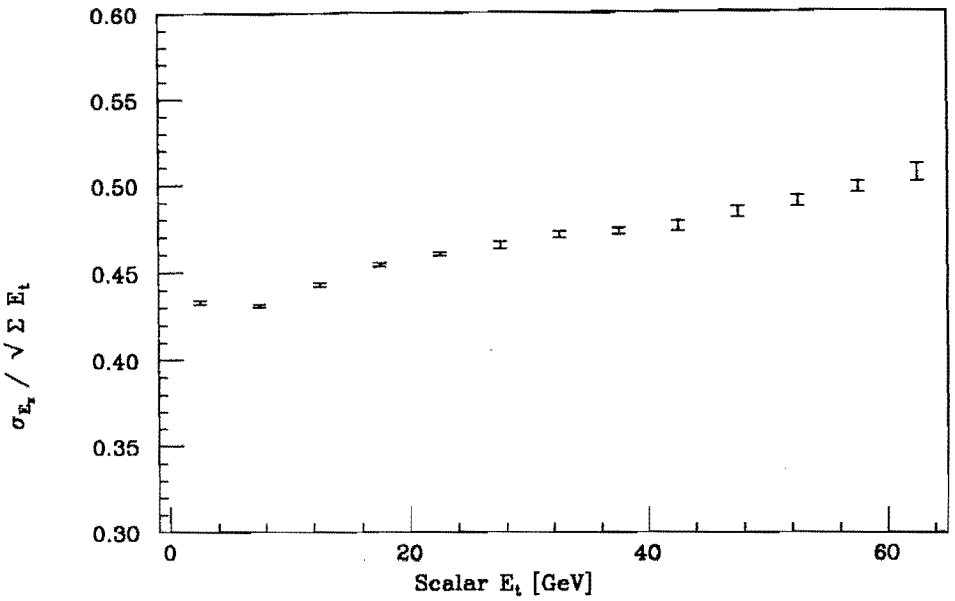

Figure 51: The dependence of $S \equiv \not{E}_x/\sqrt{\sum E_t}$, a neutrino-resolution variable, on the total scalar E_t observed in the event. Over the range of $\sum E_t$ in the W decay candidates (see Fig. 52), the constant of proportionality is approximately 0.47.

There is one further effect which must be simulated. The di-jet cut used in selecting events in our W decay sample (no cluster of energy greater than 5 GeV within 30° in ϕ of back-to-back with the muon) preferentially removes energy opposite the muon. Energy fluctuations in the direction of the muon will not be removed, while those opposite the muon will be. We measure the size of this effect with the projections of the underlying event energy,[10] $\not{u}$, parallel and perpendicular to the muon, $\not{u}_{\parallel}$ and $\not{u}_{\perp}$. Distributions of these projections are shown in Fig. 54. The offset from 0 in the parallel component distribution is -115 ± 150 MeV. This offset opposite the muon direction enters directly into the neutrino p_t. We thus force the Monte Carlo to reproduce this effect by adding a constant offset, $\vec{\not{u}}_{\parallel}^{off}$, to the Monte Carlo underlying event energy.

The full underlying event in the model, $\vec{\not{u}}$, is given by Equation 21:

$$\vec{\not{u}} = \tilde{\vec{u}} + \tilde{\vec{p}}_t^{jet} + \vec{\not{u}}_{\parallel}^{off} \quad . \tag{21}$$

[10]The underlying event energy is defined as $\not{E}_t$ with the energy deposited by the muon removed.

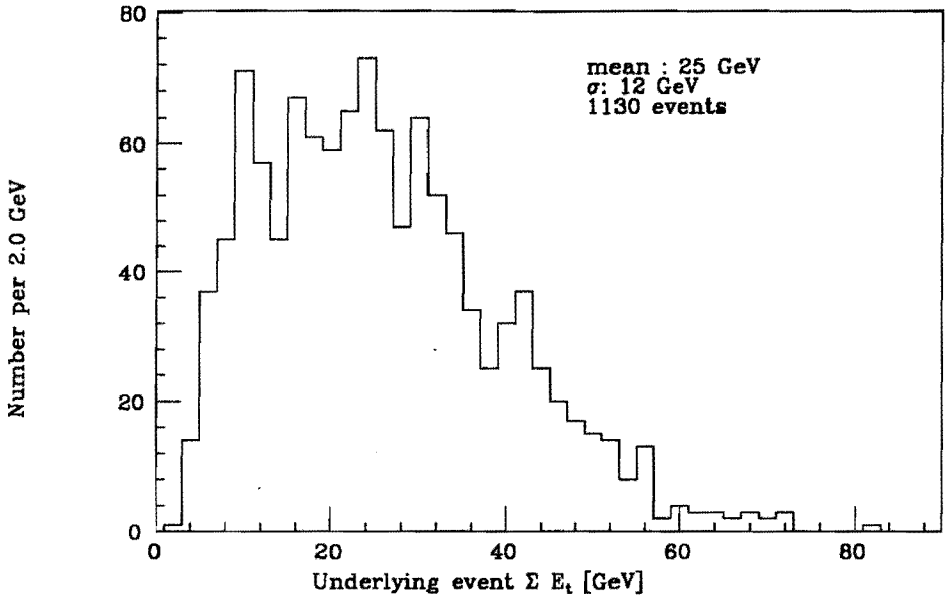

Figure 52: The total scalar transverse energy observed in $W \rightarrow e\nu$ decay candidate events after the electron energy and the recoil energy opposite the W have been removed. This distribution is used as an input to the Monte Carlo for modeling detector effects in the neutrino momentum measurement resolution.

From this, we reconstruct the neutrino transverse momentum

$$\vec{\nu} = \vec{\not{p}} - \vec{p}_t^{\,\mu}$$

and the μ-ν transverse mass. We require p_t^μ and $p_t^\nu \geq 25$ GeV/c^2 as we did in our selection of W decays.

12 Constraints on and Systematics of the Model

We discuss constraints on the parameters of our simulation of W events and the systematic uncertainty in the W mass measurement due to the simulation. We constrain these parameters using CDF data: W decays, Z decays, minimum-bias events and jet data. The CDF analysis of W decays to muons and electrons are intertwined since they use the same model of the calorimeter response to the event underlying the W. Because the geometric coverage of the central calorimeter is greater than that of the muon chambers,

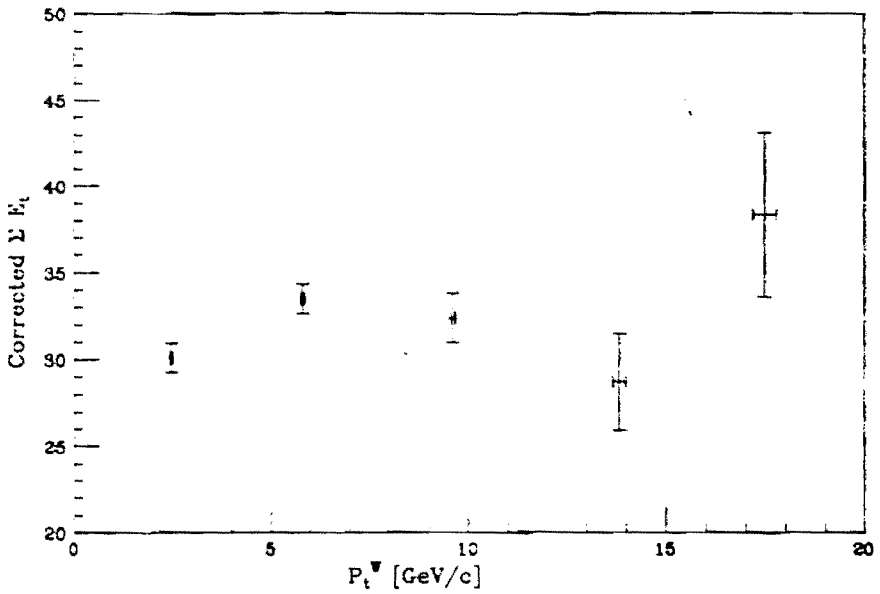

Figure 53: A plot of the relationship between the W p_t in $W \rightarrow e\,\nu$ decay candidate events and the total scalar transverse energy, $\sum E_t$, after $\sum E_t$ has been corrected for the electron energy in the event and for the recoil energy opposite the W. ($E_t^{recoil} = 1.4 \times p_t^W$.) Removing this correlation between p_t^W and $\sum E_t$ allows use of the distribution of Fig. 52 in the parametrization of $\not\!\!E_t$ resolution from minimum-bias events.

the sample of W decays to electrons (1130 events) is nearly twice as large as that of W decays to muons (592 events). The size of many of our systematic uncertainties will be established by the statistical uncertainties on the constraints we measure. Thus we study the calorimeter response to the recoil against the W in $Z \rightarrow e^+ e^-$ decays. Also, as was stated in the last section, where the simulation requires input from the data (p_t^W and $\sum E_t$ spectra), we use the spectra from the electron sample to reduce the effects of statistical fluctuations. We will need to keep track of which systematic uncertainties are common to both electron and muon analyses, since in the end we will combine the measurements of the W mass to arrive at a single measurement for CDF. Systematics of the electron analysis are discussed in greater detail in [42].

Many of the systematic effects are measured as follows. We determine from data the constraints on parameters in our simulation. We then vary the parameters one at a

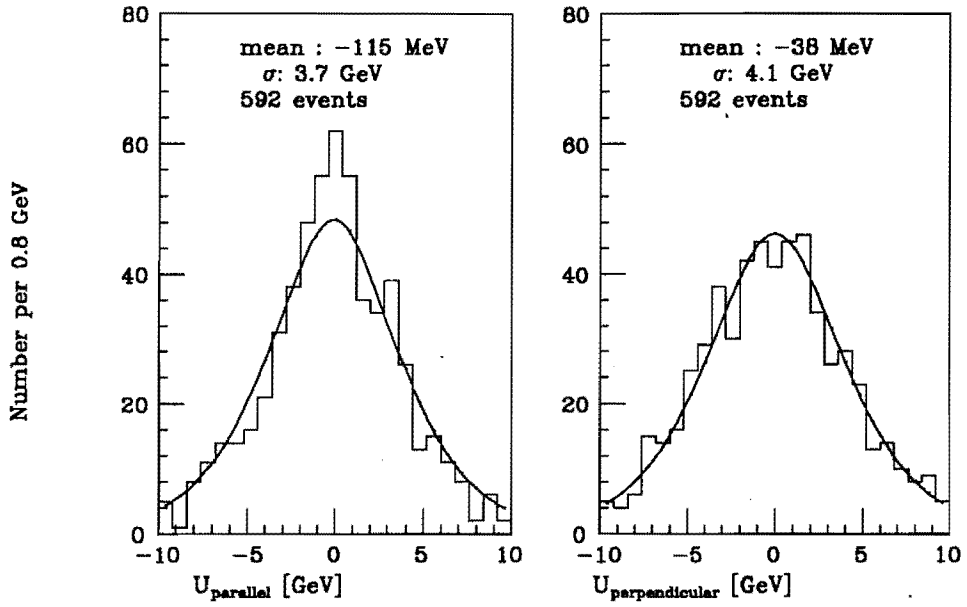

Figure 54: a) The projection of the underlying event onto the muon direction ($\not{u}_{||}$) The curves are the prediction of the model. b) The projection of the underlying event perpendicular to the muon direction ($\not{u}_{\perp}$).

time and establish the effect on the measured W mass of a one sigma variation in the parameter as follows. We generate a large sample of Monte Carlo events (100 000) with a single parameter changed. We then determine the W mass for this sample when fit (see Section 13) to our nominal set of Monte Carlo distributions[11] and compare the fit mass to the W mass used in generating the sample. This reduces the impact of the systematic uncertainty in the fitting procedure on the determination of other systematics.

12.1 Parton Distribution Functions

Several "standard" choices of parton distribution functions are used to simulate W production. We use EHLQ-1[43], DO-1, DO-2[44], DFLM-1, DFLM-2, DFLM-3[45], MRS-B and MRS-E [15] as a sample of the different possible assumptions we could make. MRS-B is the standard choice. There is little difference between it and more recent parton

[11]We will also refer to these distributions as "lineshapes", since when fitting the W mass, we use only the relative shape of the Monte Carlo distributions.

distribution functions – MRS-E and the DFLMs – which were created expressly for the purpose of studying weak boson production at the colliders [15].

Varying the assumed structure of the proton changes the W longitudinal momentum distribution. As the fraction of W momentum that is longitudinal changes, the fraction

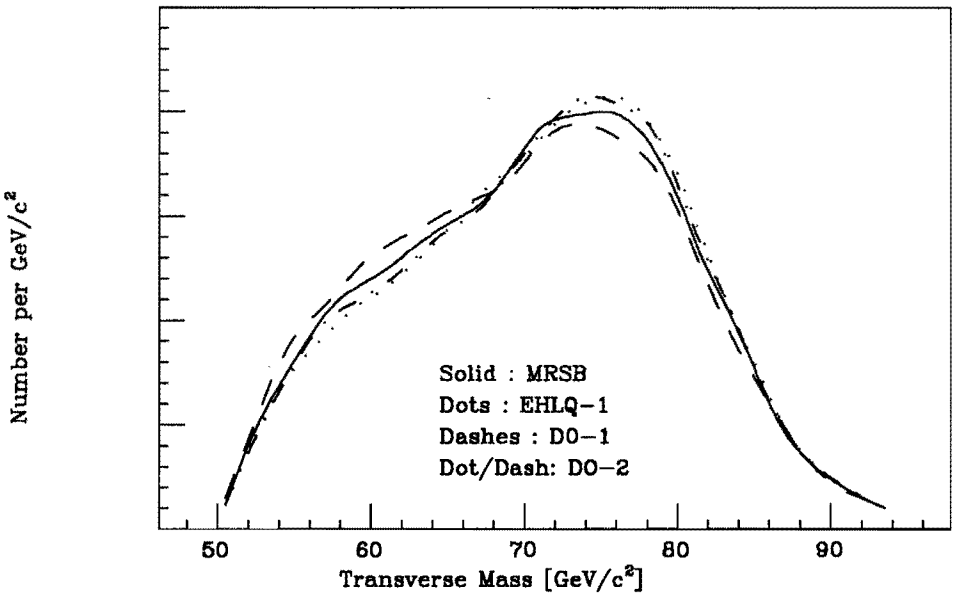

Figure 55: The predicted m_t distribution for several choices of parton distribution function.

of lepton momentum that is longitudinal changes. The change in the transverse mass distribution with differing parton distribution functions is shown in Fig. 55. In addition, the assumed relative abundance of sea and valence quarks will change the polarization distribution of the Ws.

To measure the systematic uncertainty, we generate one Monte Carlo sample (with $m_W = 80.0$ GeV/c^2) for each of the parton distributions tested. Other parameters in the model are unchanged. We fit these samples to our nominal set of Monte Carlo distributions. From Fig. 55, we see that the largest effect of the differing proton structure is at low transverse mass. In Table 5, we list the fit mass variation with the choice of lower cutoff. We choose 65 GeV/c^2 as a lower limit to our fit range to limit our sensitivity

Lower cutoff	MRS-B	EHLQ-1	DO-1	DFLM-2
55 GeV	80.01 ± 0.03	79.92 ± 0.03	80.07 ± 0.03	79.94 ± 0.03
60 GeV	80.02 ± 0.03	79.94 ± 0.03	80.06 ± 0.03	79.96 ± 0.03
65 GeV(nom.)	80.01 ± 0.03	79.94 ± 0.04	80.00 ± 0.03	79.94 ± 0.04
70 GeV	80.03 ± 0.04	79.93 ± 0.04	79.95 ± 0.04	79.94 ± 0.04

Table 5: Comparison of fit mass values for various choices of lower cutoff of the fit range. The upper cutoff is 94 GeV/c^2. All masses listed are in units of GeV/c^2. Monte Carlo samples are fit using a grid generated with the nominal MRS-B parton distribution functions.

to the choice of parton distribution functions and to further reduce the background in our data (see Section 9.2). The fit mass found from the transverse mass spectrum over our nominal fit range of 65 to 94 GeV/c^2 is given for each of the proton distribution functions in Table 6. The largest deviation from the input mass is 60 MeV/c^2. We take 100 MeV/c^2 as a conservative[12] estimate of the uncertainty in the W mass measurement due to parton distribution functions.

12.2 Resolution and p_t^W

The parametrization of the muon momentum resolution, the response of the calorimeter to the uncorrelated underlying event and the recoil against the W, and the assumed input p_t^W distribution all contribute to the overall resolution entering into the kinematic distributions. We constrain all parameters except the input p_t^W distribution using other data, adjusting the latter to obtain consistency with the observed W data. We determine each uncertainty by varying the parameter within its constraints with all other parameters fixed. Although there are correlations between the parameters, we take the uncertainties to be independent when computing the overall systematic effect.

For a given set of model parameters, we adjust the input p_t^W distribution until the

[12]We assume all parton distribution functions are equally valid.

PDF choice	Monte Carlo
MRS-B (nominal)	80.01 ± 0.03
MRS-E	80.00 ± 0.03
DFLM-1	79.96 ± 0.03
DFLM-2	79.94 ± 0.04
DFLM-3	79.97 ± 0.03
DO-1	80.00 ± 0.03
DO-2	79.99 ± 0.03
EHLQ1	79.94 ± 0.04

Table 6: Comparison of mass fit to Monte Carlo samples generated using different parton distribution functions for the nominal fit range of 65-94 GeV/c^2. All masses listed are in units of GeV/c^2. The fitting grid was generated with MRS-B parton distribution functions.

output distribution from the Monte Carlo agrees in first and second moment – mean and rms – with the observed p_t^W distribution as shown in Fig. 56. This constrains the average of the input p_t distribution to $\pm 4\%$. Shifts of the average input p_t by more than 4% cause disagreements of greater than one sigma between the moments of the distributions predicted by the Monte Carlo and found in the data. This is the only constraint in our Monte Carlo which is taken directly from the W data. Varying the mean of the assumed input p_t^W distribution by $\pm 4\%$ leads to 50 MeV/c^2 shifts in fit mass.

The resolution of the measurement of muon momentum is described by

$$\frac{\sigma^{\mu}_{p_t}}{p_t^2} = 0.11\%. \tag{22}$$

which is Gaussian in $1/p_t$. The resolution of the measurement of electron energy is given by

$$\frac{\sigma_E}{E} = \sqrt{(\frac{a}{\sqrt{E_t}})^2 + b^2} \qquad a = 13.5\% \qquad b = 2.0\%. \tag{23}$$

The distribution of the ratio of calorimeter energy to track momentum for electrons from $W \rightarrow e\,\nu$ decays is plotted in Fig. 57. The width of the distribution is a convolution of

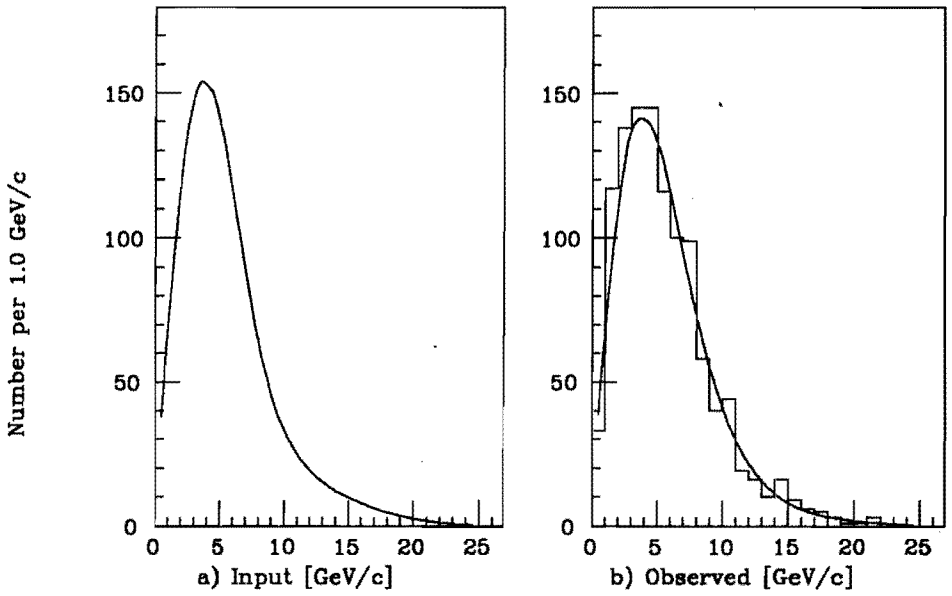

Figure 56: a) The input p_t distribution of the W candidates used in the Monte Carlo. b) The agreement between the observed W p_t distribution (histogram) and the output of the simulation (line) when the input of a) is used.

the resolutions of the tracking chamber measurement of curvature and the calorimeter measurement of electromagnetic energy given by Equation 22 and Equation 23. The tail is due to radiation of collinear photons by the electron during the decay. Since the photons are collinear with the election, photon energy is clustered with that of the electron. Thus, the calorimeter measures the energy of the electron-photon system while the tracking chamber measures only the momentum of the electron. From the width of the E/p distribution – excluding the tail – and the allowed variation in electron resolution (measured elsewhere, see [42]), the possible variation in the tracking chamber resolution is determined to be $\pm 10\%$ [31]. We generate samples of 100 000 Monte Carlo events with a W mass of 80.0 GeV/c^2 and width of 2.2 GeV with a tracking chamber resolution of 0.0012, differing from the nominal 0.0011 by 10%. The fit mass is 80.078 GeV/c^2. To check for possible pathologies, we change the resolution by 20% to 0.0013 and generate another sample. The fit mass of this sample is 80.160 GeV/c^2. From the mass shifts

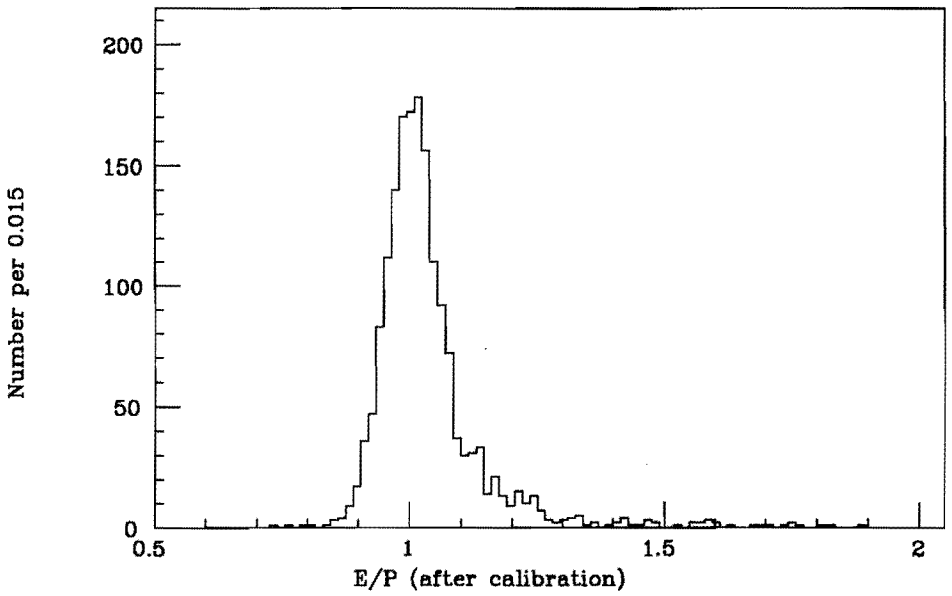

Figure 57: The E/P distribution for W decay electrons. The width of the distribution is a convolution of Gaussian distributions in $1/p_t$ and energy. The tail of the distribution is due to the radiation of collinear photons from the electron, included in the measurement of the electron energy, but not in the measurement of momentum.

of 80 and 160 MeV/c^2 for changes in resolution of 10 and 20%, we conclude that there are no such pathologies and that the systematic uncertainty on the W mass due to the tracking chamber resolution assumed in the simulation is 80 MeV/c^2.

We now turn to the uncorrelated part of the underlying event. The $\not\!\!E_t$ resolution is parametrized as $(0.47 \pm 0.01)\sqrt{\sum E_t}$. We generate 100 000 Monte Carlo events with the constant varied from -3 sigma to +3 sigma and compare the mass found by fitting to the nominal lineshapes to that used in generating the sample. We find that the variation scales linearly with sigma and that the one sigma variation is 30 MeV/c^2. Our underlying event model assumes that a linear parametrization ($0.47\sqrt{\sum E_t}$) adequately describes the data when it is clear from Fig. 51 that there is some nonlinearity. More sophisticated parametrizations show that this effect is negligible [46]. We also correct the $\sum E_t$ distribution used as an input to the simulation by correcting event-by-event for the E_t associated with the W recoil momentum (see Section 11.3.2). We assume the

associated E_t to be 1.4 times the actual p_t^W. Varying this multiplier from 1.2 to 1.8 ($\pm$ 1 sigma) changes the fit mass by 20 MeV/c^2.

High p_t Ws are balanced by recoil energy in the form of jets. The observed recoil energy is lower than the true recoil energy. For jets of raw cluster energy 20 GeV, the energy scale is depressed by a factor of 1.4 [21]. Response to the 3-5 GeV recoil energy typical of the W sample is further depressed by magnetic field effects. Charged particles with transverse momentum below 400 MeV/c will curl up in the magnetic field and not reach the central calorimeter. Furthermore, those with p_t less than 800 MeV/c will arrive at the calorimeter at significantly different azimuth than that at which they started, defeating the projective nature of the calorimeter towers and degrading the energy measurement.

The parameters describing the response at low values of p_t^W are obtained from the study of transverse momentum balance in Z events. Since the momentum of both leptons is well-measured compared to the neutrino momentum in W decays, the Z momentum is well-determined. We study the p_t[13] balance along the angular bisector in the azimuthal projection of the Z event. As shown in Fig. 58, this quantity, p_η, is largely dependent on the measurement of the electron angles, not their energies, and is, thus, less biased for studying the calorimeter energy response than p_t. By looking at the recoil in the η instead of the ξ direction (see Fig. 58), we minimize the effects of calorimeter energy resolution. The energy deposited by the electron smears the p_ξ component of the Z momentum. The energy observed in each calorimeter tower is scaled until the calorimeter measurement of p_η matches that determined from the energies of the two electrons. From this we determine that the calorimeter measures only an average of half the recoil momentum (Fig. 59). Since the p_t spectrum of the W and Z differ little for the low transverse

[13]In this particular instance, we label as momenta quantities which are actually energies measured in the calorimeter. The masses of the leptons are negligible. By using the calorimeter measurement of energy, we minimize the effect of final state radiation on the measurement of the momentum balance. Thus, we use the Z decays to electrons and not to muons. In the latter case, the momentum measurement in the tracking chamber can be reduced by a radiated photon.

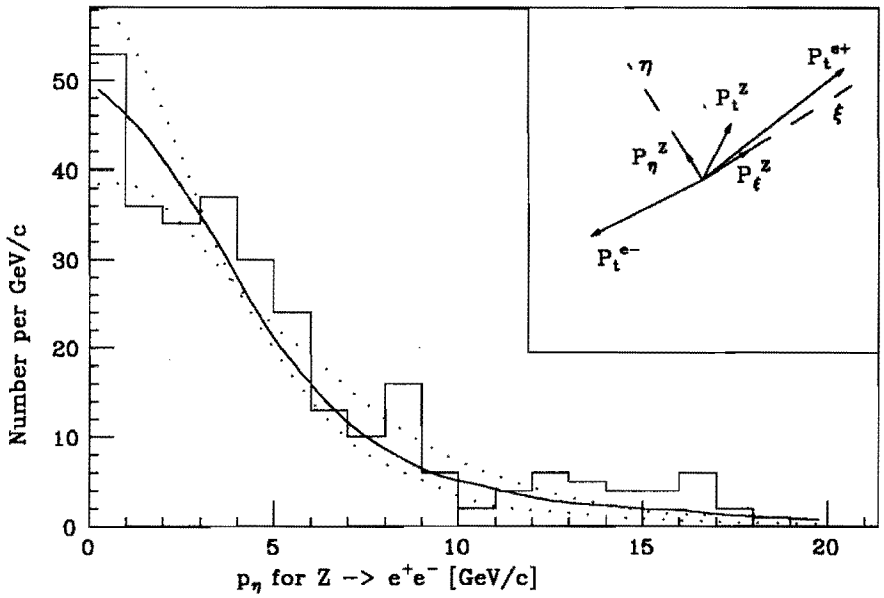

Figure 58: The di-lepton p_η observed in Z events compared to our model's prediction (solid line). The dotted lines show the relatively normalized predictions for 1σ variations of $k_{u'}$ in the model. The insert defines the η-ξ coordinate system. Since the leptons tend to be back-to-back, p_η is largely determined by track angles.

momentum Ws used in this analysis, we assume that this applies for Ws as well. This scale factor is an average over all Zs. We make two additional assumptions to extract the p_t-dependent degradation factor, $k_{u'}$, used in the model of recoil. First, we assume that the factor must match the known jet correction above $p_t = 30$ GeV/c [20]. (Note that none of our Ws have p_t this large.) We also assume that it changes linearly below 30 GeV/c. Given these constraints and that the degradation factor convolved with the p_t spectrum of the Zs must produce an average degradation of 2, we determine that $k_{u'}(p_t = 0) = 2.3 \pm 0.3$. This completely determines the degradation factor $k_{u'}$ plotted in Fig. 50. The uncertainty of ± 0.3 is determined by the point where the agreement between the Z data and the model (the dotted lines in Fig. 58) differ by more than one sigma. We generate samples of 100 000 events with $k_{u'}$ varied from -3 to 3 sigma and fit the W mass. We find that the uncertainty in the parametrization of the degradation corresponds to a 50 MeV/c^2 uncertainty in the W mass.

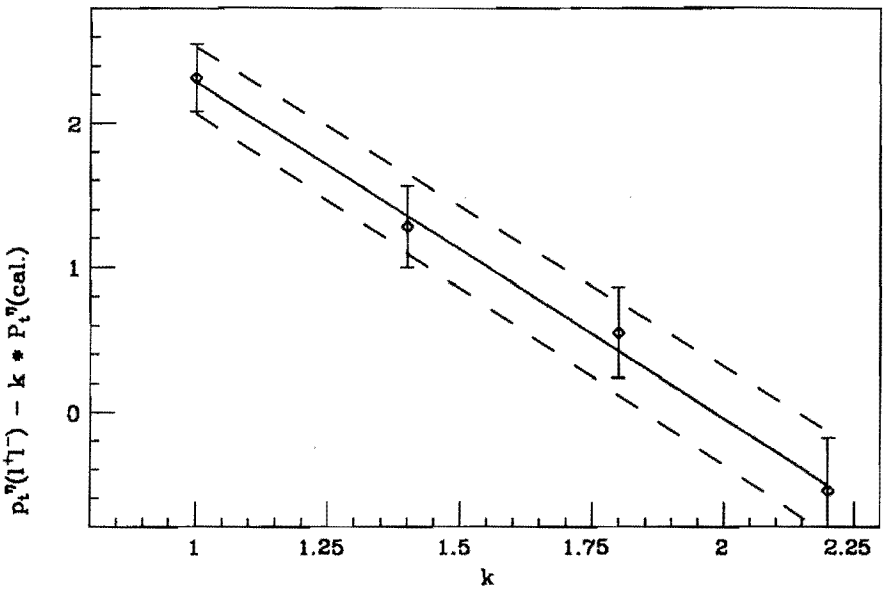

Figure 59: The average difference between the di-lepton p_η and the measured recoil p_η for $Z \rightarrow e^+e^-$ events as a function of the scaling factor applied to calorimeter energy. Balance is achieved for a scaling factor of 1.99 ± 0.14. The scaling accounts for calorimeter nonlinearities and magnetic field effects which reduce the observed recoil energy.

We assume that the jet-like recoil energy behaves like higher energy jets with $\sigma_{recoil} = 0.85\sqrt{p_t^{jet}}$. We constrain σ_{recoil} by unfolding the underlying event contribution[14] to the resolution in the measurement of p_η in Z events. In these events we have a true measurement of the recoil p_t^{jet} from the decay di-leptons. After removing the underlying event resolution (in quadrature), the spread on p_t^{jet} limits the constant factor to $0.85^{+0.3}_{-0.2}$. Generating 100 000 event samples with the jet resolution varied by $\pm 1\sigma$, we find the uncertainty in W mass due to jet resolution is 60 MeV/c^2.

The overall systematic uncertainty due to uncertainty in resolutions and p_t^W distribution, adding all these contributions in quadrature, is 130 MeV/c^2 (Table 7). That portion of it (100 MeV/c^2) coming from the simulation of underlying event energy and resolution and recoil response and resolution, and the allowed variation of the input p_t^W

[14]The underlying event is just a minimum-bias event. The resolution is that of the $\not\!\!E_t$ measurement measured in minimum-bias events.

distribution is common to the measurement of the mass using the $W \rightarrow e\nu$ decay sample.

Uncertainty	Muons	Common
Average p_t^W constraint	50	50
Uncertainty in track momentum resolution	80	
Uncertainty in $\not\!\!E_t$ resolution	30	30
Correction to $\sum E_t$ ($E_t^{recoil} = 1.4 \times p_t^W$)	20	20
Uncertainty in k_u	50	50
Jet resolution uncertainty	60	60
Total	130	100

Table 7: Uncertainties in the W mass due to p_t^W and the simulation of the calorimeter response to the underlying event. All uncertainties are quoted in units of MeV/c^2. The uncertainties which are the same for both electron and muon analyses are listed as common.

12.3 Parallel Energy Balance

The offset in the projection of the background event energy parallel to the muon, $\not\!\!u_{||}$, is -115 ± 150 MeV. This offset in $\not\!\!u_{||}$ is consistent with the di-jet requirement. We test this consistency by removing events with jets above 5 GeV between 60 and 120° of the muon (a di-jet cut perpendicular to the muon) and measuring the change in $\not\!\!u_{\perp}$. The mean $\not\!\!u_{\perp}$ changes by 60±240 MeV, consistent with the measured offset in $\not\!\!u_{||}$. The offset in $\not\!\!u_{||}$ is also sensitive to the way in which the energy deposition of the muon is extracted from the $\not\!\!E_t$ measurement. It is difficult to make any quantitative statement about these effects due to the relative imprecision with which the offset is measured. We match the average $\not\!\!u_{||}$ in the model to the data by adding a constant offset to $\not\!\!u_{||}$. To prevent the tails of the distribution from biasing the result, the offsets are computed using a ±10 GeV window about $\not\!\!u_{||} = 0$. For wider windows, shifts of order 300 MeV are observed and the trend is reproduced by the model. Fig. 60 shows that the offset depends on range of m_t included in its determination. The trend of the offset with m_t is well reproduced by the model.

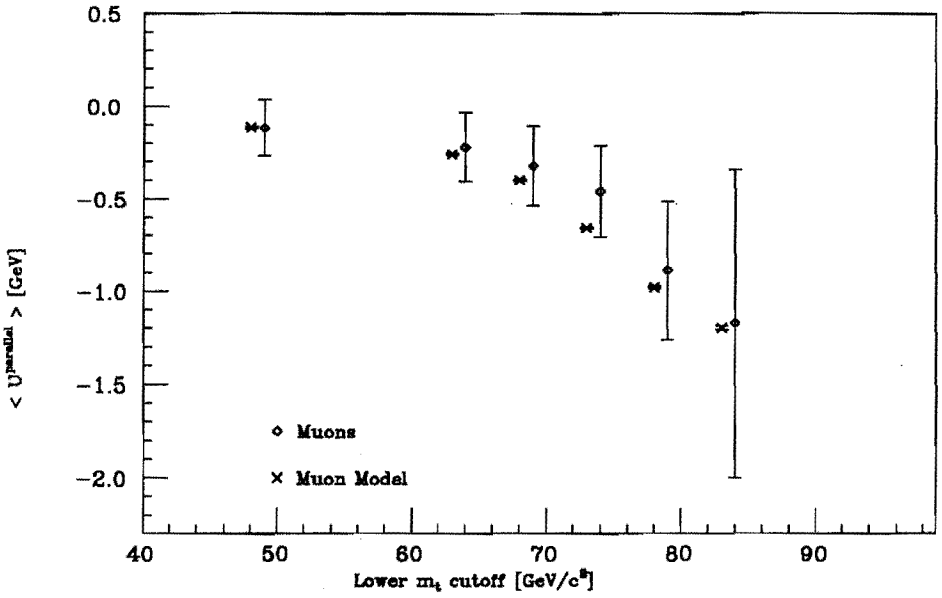

Figure 60: The average $\not\!\!E_t$ along the muon direction ($< \not\!\!u_{||} >$) as a function of the m_t range of events used in the computation. The x-axis gives the minimum m_t used, the maximum is 94 GeV/c^2. The simulation reproduces this trend.

Since the muon and neutrino are back-to-back to first order, $\not\!\!u_{||}$ enters directly into the momentum of the neutrino and, thus, into the transverse mass. This is only a problem if the Monte Carlo and data are not matched, but the offset is poorly measured in the data. This uncertainty in $\not\!\!u_{||}$ translates directly into an uncertainty in p_t^ν and, thus, m_t. To allow for possible systematic error, we assume that only events with $m_t > 70$ GeV/c^2 influence the W mass measurement. Using only these events, the statistical uncertainty of the $\not\!\!u_{||}$ measurement is 215 MeV. This translates into an uncertainty of 240 MeV/c^2 in the W mass measurement.

12.4 Summary of Uncertainties of the Model

The contributions to the uncertainty of the W mass due to systematic uncertainties in the model are summarized in Table 8.

Uncertainty	Muons	Common
Parton distribution functions	100	100
Underlying event resolution and p_t^W	100	100
Resolution of the measurement of p_t^μ	80	
Calorimeter parallel energy balance	240	

Table 8: Uncertainties in the W mass due to the simulation of W production and decay. All uncertainties are quoted in units of MeV/c^2. The uncertainties which are the same for both electron and muon analyses are listed as common.

13 The Fitting Procedure

The mass of the W is determined by comparing the predictions generated by the Monte Carlo with those in the data. The distributions of p_t^μ, p_t^ν, and m_t ("lineshapes") are generated at the 11 values of Γ_W and 10 values of m_W shown previously in Fig. 47. Roughly 10^6 W decays are used in the prediction of the lineshape for each mass-width combination, which are stored in 1 GeV/c^2 intervals of transverse mass (or 1 GeV/c intervals of transverse momentum). These distributions give the relative probability, $P(m_W, \Gamma_W)$, for any value of m_t or p_t. We compare the simulated line shapes to the data using an event-by-event likelihood. The likelihood function:

$$\begin{aligned} L &= \Pi[P_i(m_W, \Gamma_W)] \\ \ln L &= \sum \ln[P_i(m_W, \Gamma_W)] \end{aligned} \tag{24}$$

is maximized as a function of mass and width with the MINUIT optimization package [47]. The product and sum extend over all events.

Our lineshapes are generated at discrete values of m_W and Γ_W, whereas we wish to fit these variables in a continuous fashion. To determine the lineshape at values of m_W and Γ_W not on the mass-width grid, we interpolate in the two dimensions of m_W and Γ_W from the lineshapes at the grid points to generate a prediction for any mass and width. We use a bicubic spline interpolation [48]; other methods of interpolation give

the same results (see Section 14). The bicubic spline interpolation is as follows. We wish to determine the probability in the n-th bin of m_t, $P^n(m_W, \Gamma_W)$, from the probability in the n-th bin of the distributions at the mass-width grid points. (A view of the $m_W - m_t$ surface is given in Fig. 61). At each of the four grid points surrounding the mass-width

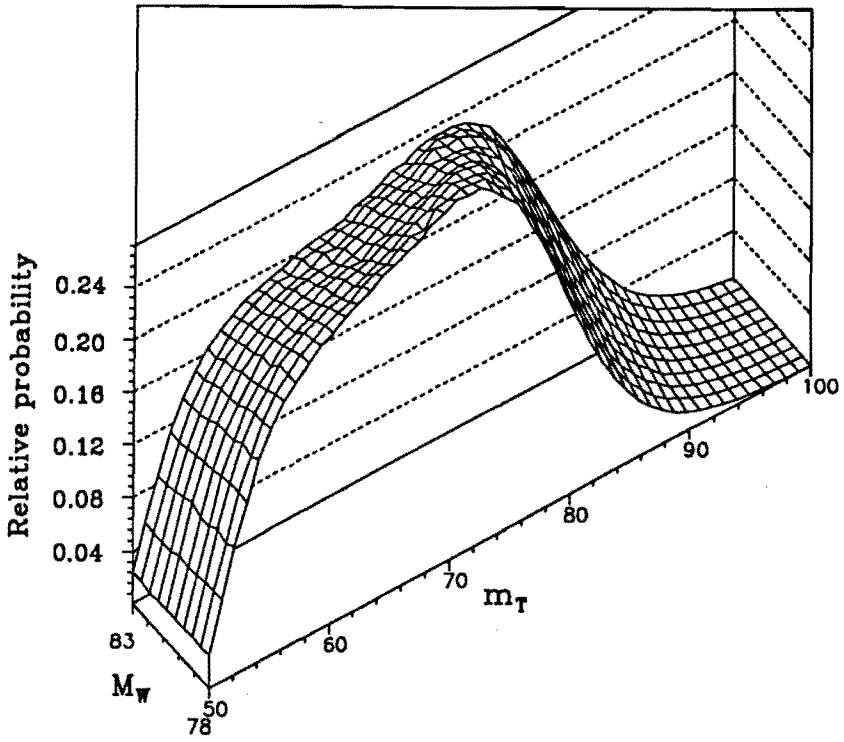

Figure 61: The m_W–m_t surface at $\Gamma_W = 2.250$ GeV. This shows one of the two dimensions in which the interpolation is done. The $\Gamma_W - m_t$ surface at a fixed m_W is similar.

point, the probability, $P^n(m_W, \Gamma_W)$, the derivative in each direction ($\frac{\partial}{\partial m_W}$ and $\frac{\partial}{\partial \Gamma_W}$), and the cross derivative ($\frac{\partial^2}{\partial m_W \partial \Gamma_W}$) are specified. The derivatives at the grid points are determined by fitting one-dimensional splines to the grid points in each dimension. The values of the function and the gradients at the grid points are sufficient to fully constrain the coefficients of a cubic polynomial. This polynomial is then used to find a value for the probability in each bin of m_t at the desired m_W and Γ_W. This interpolation ensures smoothness of the interpolated surface. The function, P^n, and the derivatives change continuously from grid point to grid point and are exactly reproduced at the grid points.

Having determined the lineshape for a given mass and width, we must compute the probability, $P_i(m_W, \Gamma_W)$, of any m_t. The probabilities are stored in 1 GeV bins. Because of the rapidly falling trailing edge of the distribution, we determine the probability of a given transverse mass (or momentum) using a linear interpolation between the the probabilities stored in the bin containing m_t and the nearest adjacent bin (see Fig 62). Once again, the details of the interpolating procedure do not change the answer.

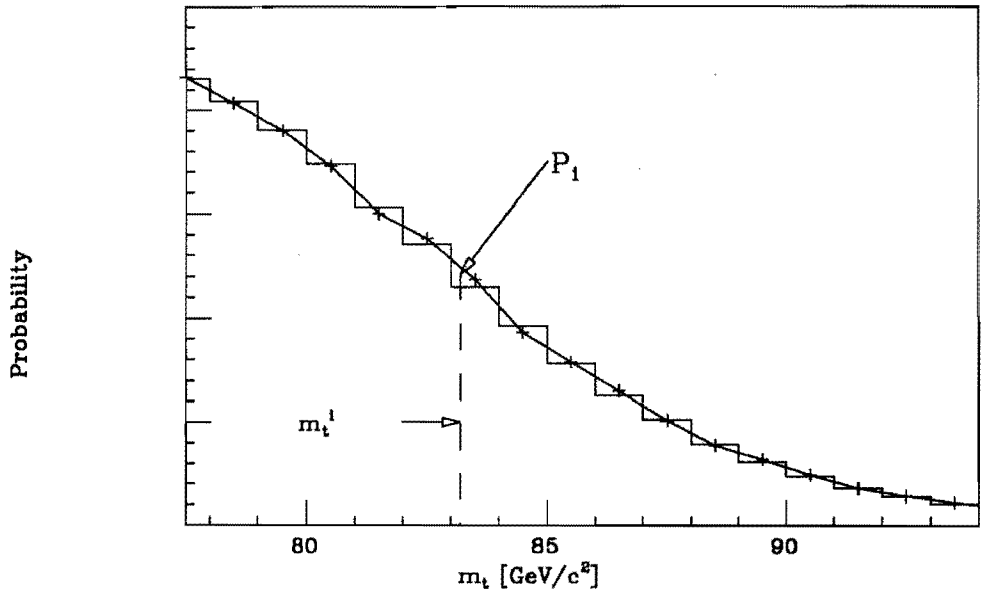

Figure 62: Details of the interpolation between bins of the kinematic distribution (m_t in this case). If m_t is below the bin center, the linear interpolation is with the next lowest bin; if above, with the next highest.

We fit only the shape of the distribution and not the number of events. The stored probabilities, P, are related to the absolute probabilities, P^{absolute}, by an interval normalization, P^{interval}. This normalization enters as a constant offset in $\ln L$ as follows:

$$\begin{aligned} \ln L &= \sum \ln(P_i^{\text{absolute}}/P^{\text{interval}}) \\ &= \sum (\ln(P_i^{\text{absolute}}) - \ln(P^{\text{interval}})) \\ \ln L &= \sum \ln(P_i^{\text{absolute}}) - \text{Constant} \quad . \end{aligned} \tag{25}$$

The absolute probability is what determines the shape of the likelihood function ($\ln L$).

The constant – related to our choice of storage interval in the lineshape predictions – plays no role in the fit. The MINUIT package controls the optimization as a function of m_W and Γ_W and determines the statistical uncertainties.[15]

14 Systematics of the Fitting Procedure

The fitting procedure is not simple. It is especially complicated by the need to simultaneously fit the mass and width in a continuous fashion when lineshapes have been generated at discrete values of these variables. In this section, we discus the systematics of fitting. We check the mechanics of fitting for pathologies, make various consistency checks and discuss other questions related to the fit.

14.1 Fitter "Jitter"

Fluctuations in the relatively small data sample (592 events) can interact with those in the larger Monte Carlo samples generated at each value of the fitting grid. When the W mass is found by fitting identical data samples to Monte Carlo lineshapes which differ only in the random number seed used in the simulation, the answers differ. We examine this "jitter" [49] in the data by comparing the fit mass from independently generated sets of lineshapes. Tables 9, 10, and 11 summarize the results from fitting the data sample to independent sets of lineshapes with approximately one-half, one-third, and one-quarter the statistics in our final set of lineshapes. Our interpretation of this as a statistical effect is supported by the scaling of the spread in fit masses by $\frac{1}{\sqrt{n}}$ where n is the number of events in the lineshape. Scaling the spread to the statistics in the final set of lineshapes ($\sigma_0 = \sigma_i \times \sqrt{\frac{n_0}{n_i}}$ where the subscripts i and 0 identify the sub-sample and final lineshape set respectively) indicates that this jitter introduces a 100 MeV/c^2 fitting uncertainty to

[15]The statistical uncertainty of a parameter is determined by searching in that dimension for the point where the log-likelihood changes by one-half from its maximum value.

m_W	Before smoothing	After smoothing
m_1	$79.76 + 0.51 - 0.43$	$79.79 + 0.53 - 0.52$
m_2	$79.96 + 0.50 - 0.76$	$79.79 + 0.54 - 0.53$
m_3	$79.77 + 0.37 - 0.39$	$79.78 + 0.54 - 0.52$
m_4	$80.08 + 0.34 - 0.96$	$79.78 + 0.54 - 0.52$
	mean $= 79.89 \pm 0.07$ $\sigma = 0.14 \pm 0.05$	mean $= 79.78 \pm 0.02$ $\sigma = 0.04 \pm 0.01$

Table 9: Fit mass with the muon data fit to lineshapes with approximately half (53%) of the statistics of the final set of lineshapes. All masses are in GeV/c^2.

m_W	Before smoothing	After smoothing
m_1	$79.59 + 0.69 - 0.35$	$79.77 + 0.54 - 0.52$
m_2	$79.81 + 0.42 - 0.36$	$79.78 + 0.55 - 0.53$
m_3	$80.10 + 0.43 - 0.92$	$79.77 + 0.54 - 0.53$
m_4	$79.75 + 0.40 - 0.38$	$79.78 + 0.54 - 0.52$
m_5	$79.93 + 0.42 - 0.61$	$79.80 + 0.54 - 0.52$
m_6	$80.01 + 0.41 - 0.99$	$79.79 + 0.54 - 0.52$
	mean $= 79.86 \pm 0.07$ $\sigma = 0.17 \pm 0.05$	mean $= 79.78 \pm 0.004$ $\sigma = 0.009 \pm 0.003$

Table 10: Fit mass with the muon data fit to lineshapes with approximately a third (35%) of the statistics of the final set of lineshapes. All masses are in GeV/c^2.

the W mass measurement.[16]

We minimize these fluctuations by smoothing the lineshapes. We parametrize the contours in m_W at constant m_t and Γ_W by a second-degree polynomial, using a least-squares fit to the probability at the 10 W mass points at each transverse mass. The probability at each W mass is then replaced by the value predicted by the polynomial. The contours before smoothing are plotted in Fig. 63 for $\Gamma_W = 2.25$ GeV. Repeating the tests summarized in Tables 9, 10, and 11, we find that the size of the jitter is now less than 20 MeV/c^2. We also note that the asymmetry between the statistical uncertainty

[16]The effect is 70 MeV/c^2 in the electron sample with its 1130 events. It is this $\frac{1}{\sqrt{n}}$ scaling with the number of events in the data sample that leads us to conclude that the jitter is due to fluctuations in the data as well as the lineshapes.

m_W	Before smoothing	After smoothing
m_1	$79.59 + 0.70 - 0.35$	$79.78 + 0.53 - 0.52$
m_2	$79.88 + 0.42 - 0.44$	$79.80 + 0.54 - 0.53$
m_3	$79.73 + 0.43 - 0.37$	$79.75 + 0.54 - 0.52$
m_4	$80.15 + 0.42 - 1.08$	$79.78 + 0.54 - 0.52$
m_5	$79.92 + 0.53 - 0.49$	$79.78 + 0.54 - 0.52$
m_6	$79.69 + 0.36 - 0.37$	$79.80 + 0.54 - 0.53$
m_7	$79.85 + 0.43 - 0.53$	$79.77 + 0.55 - 0.53$
m_8	$80.07 + 0.33 - 0.54$	$79.79 + 0.55 - 0.53$
m_9	$79.38 + 0.99 - 0.36$	$79.79 + 0.54 - 0.52$
	mean $= 79.81 \pm 0.07$	mean $= 79.78 \pm 0.005$
	$\sigma = 0.22 \pm 0.05$	$\sigma = 0.014 \pm 0.003$

Table 11: Fit mass with the muon data fit to lineshapes with approximately a quarter (24%) of the statistics of the final set of lineshapes. All masses are in GeV/c^2.

measured in the positive and negative directions is reduced.

14.2 Fit Range

We discussed previously the choice of the lower limit to the fit range, which reduces the effect of low p_t backgrounds and parton distribution functions. We take up here the choice of an upper limit. We expect non-gaussian tails in our resolutions. To reduce the effect of these tails, which are not included in the Monte Carlo simulation, on the result, we fit only transverse masses below 94 GeV/c^2. Above 94 GeV/c^2, we observe 15 events in the data, while the Monte Carlo predicts 3 for the nominal fit m_W. In addition to the effects of the tails in the momentum and $\not\!\!E_t$ measurement resolutions, these events could also be real W events in which the energy of the jet recoiling against the W is not fully measured. The requirement that there be no jet greater than 7 GeV in the events in the final sample imposes a *de facto* cut on the p_t of the W, since high p_t Ws, which produce high p_t muons in their decay, are accompanied by high E_t jets. High p_t Ws, where the jet escapes through fiducial cracks in detector coverage, can contribute events to the high transverse mass tail. The effect of the choice of upper limit of the fit range on the W mass

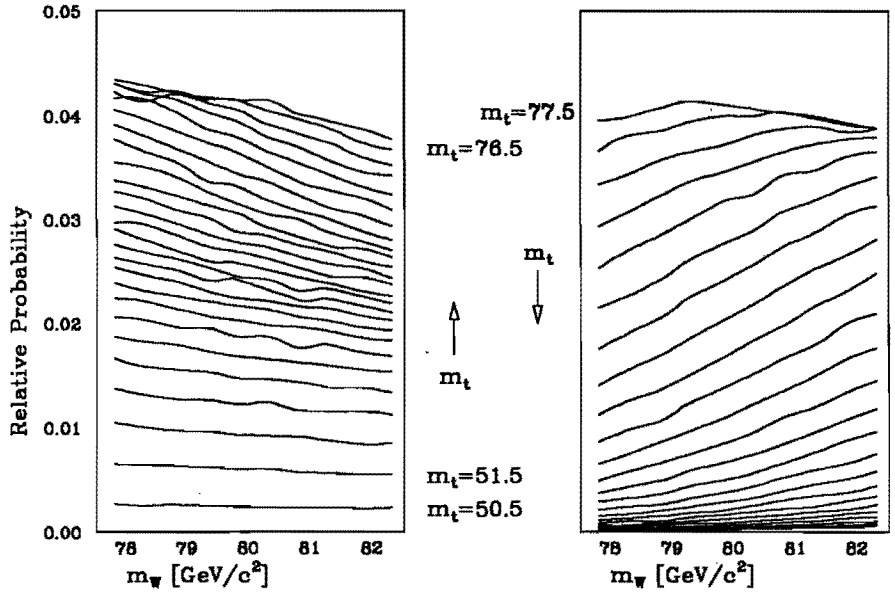

Figure 63: Contours of probability as a function of m_W at constant m_t for the surface plotted in Fig. 61. The plot is divided in half to show the effect as we move over the peak and down the falling edge of the Jacobian (right plot). The contours in constant m_t are parametrized by second-degree polynomials. m_W and m_t are given in units of GeV/c^2.

measurement is summarized in Table 12. From the fits to both m_W and Γ_W, one can see that the effect of varying the fit range is primarily on the width. Increasing the upper cutoff above the nominal value includes more of the tail of the distribution, implying a larger width. This produces a lower mass due to the coupling between mass and width (see below). The size of this effect can be limited by fixing Γ_W to the Standard Model value of 2.1 GeV and fitting only the mass. As the upper limit is lowered below the nominal value, we begin to see the effect of throwing away information. It is the falling edge of the spectrum that is most important in determining the mass and width. If we discard too much information, the fitting procedure begins to loose its resolving power, the determination of the W width becomes problematic; and the statistical uncertainty unreliable.

Width Floated				
Cutoff (GeV/^{2})	Fit to Data (m_W; Γ_W)	χ^2/dof		Fit to Monte Carlo
98	79.46 ± 0.64 ; 3.4 ± 1.0	34.2/30		80.01 ± 0.04 ; 2.19 ± 0.05
96	79.69 ± 0.65 ; 2.3 ± 1.0	29.7/28		80.01 ± 0.05 ; 2.18 ± 0.06
94 (nominal)	79.69 ± 0.65 ; 2.3 ± 1.1	29.3/26		80.00 ± 0.04 ; 2.18 ± 0.07
92	79.90 ± 0.25 ; 0.4 ± 1.5	25.9/24		80.01 ± 0.04 ; 2.17 ± 0.07
90	79.97 ± 0.61 ; 0.4 ± 2.3	25.9/22		80.00 ± 0.04 ; 2.28 ± 0.07
Width Constrained				
Cutoff (GeV/c^2)	Fit to Data (m_W)	χ^2/dof		Fit to Monte Carlo
98	80.06 ± 0.52	33.8/31		80.00 ± 0.04
96	79.76 ± 0.52	29.6/29		80.00 ± 0.04
94 (nominal)	79.78 ± 0.53	29.1/27		80.00 ± 0.04
92	79.54 ± 0.54	26.5/25		80.00 ± 0.04
90	79.69 ± 0.57	26.1/23		80.02 ± 0.04

Table 12: The comparison of mass and width fit values for various choices of upper cutoff of the fit range. All masses are listed in GeV/c^2 and widths in GeV. The Monte Carlo samples had $m_W = 80$ GeV/c^2 and $\Gamma_W = 2.2$ GeV and contained 110 000 events.

14.3 Tests

We use Monte Carlo samples to check the consistency of our results and to look for pathologies in our fitting procedure. These tests are of two kinds. Both use Monte Carlo samples generated at a specific mass of the W and at $\Gamma_W = 2.2$ GeV. To reduce the effect of statistical fluctuations on the measurements, we first fit samples of approximately 100 000 events. Then, to explore the statistical properties of the procedures, we generate many (~ 200) samples of the same size as the W decay data sample.

We first explore the mechanics of the interpolations used in the fit. In Fig. 64 is plotted the difference between the mass and width used in generating the sample (m_W = 79.5 GeV/c^2, Γ_W = 2.2 GeV) and the fit mass and width for different interpolation algorithms. Uncertainties plotted are those from the fit to the mass or width. (The

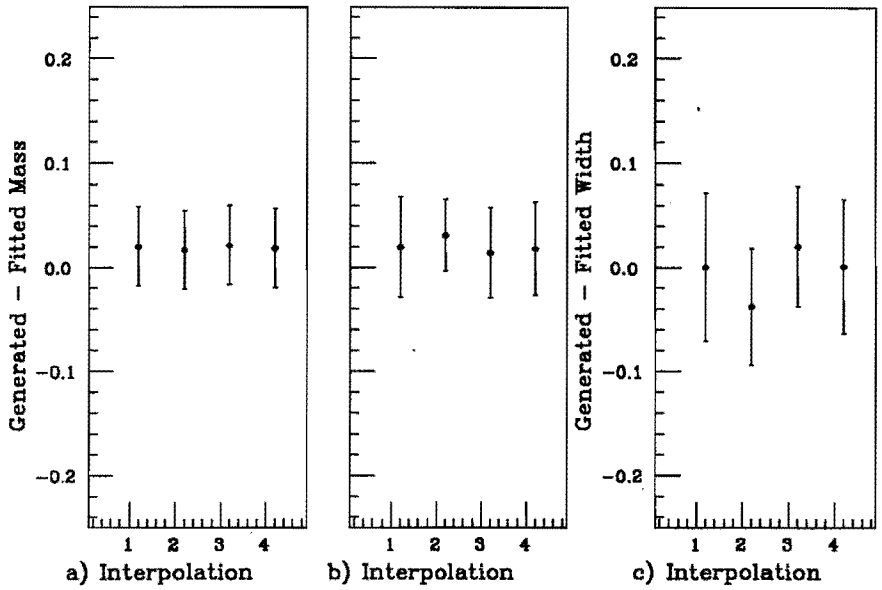

Figure 64: Difference between a) generated and fit m_W with Γ_W fixed to the generator input, b) generated and fit m_W with Γ_W floated, and c) generated and fit Γ_W. These are plotted as a function of the interpolation used to interpolate between grid points: (1) linear, (2) bilinear, (3) bicubic, and (4) bicubic spline [50]. Uncertainties are those from the fit to the mass or width. The sample was generated with a mass of 79.5 GeV/c^2 and width of 2.2 GeV. Masses are given in units of GeV/c^2 and widths in GeV.

generated mass or width has no error.) The differences between the fit mass and the input to the Monte Carlo for each of the 4 algorithms used to interpolate between grid points are scattered about 0. The scatter is less than 10 MeV/c^2 if the width is fixed to the generated value; 20 MeV/c^2, if it isn't; and no systematic offset is seen when the nominal linear interpolation between transverse mass bins is used. If a cubic spline algorithm [51] is used for the interpolation between transverse mass bins (Fig. 65), the fit mass is systematically higher than the value found using the linear interpolation by 30 to 40 Mev/c^2. It is also farther away from the mass used to generate the sample. We thus use the linear interpolation between transverse mass bins as the default.

We check for pathologies related to grid points in the same manner. We generate samples with W masses from 79.3 to 80.3 GeV/c^2 in 100 MeV/c^2 steps. (Grid points are at 79.3, 79.8 and 80.3 GeV/c^2.) In Fig. 66 are plotted the difference between generated

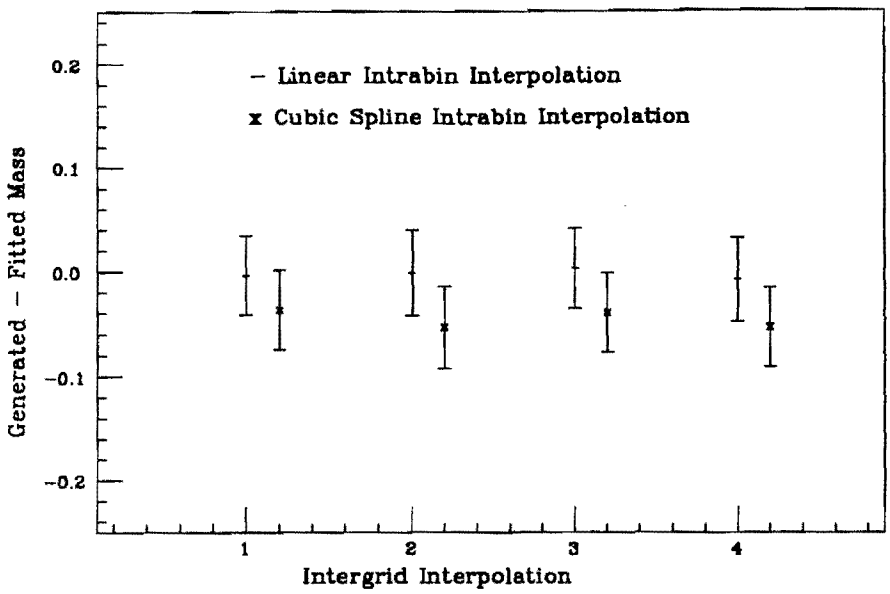

Figure 65: Difference between generated and fit m_W with Γ_W fixed to the generator input for each of the 4 intergrid interpolations with either a linear or cubic spline intrabin interpolation. This sample was generated with a mass of 80.0 GeV/c^2 and width of 2.2 GeV. The lineshapes for this test were not smoothed. Masses are given in units of GeV/c^2 and widths in GeV.

and fit mass for fits with the width fixed to the generated value and with the width floated. In the latter case, we also plot the difference between generated and fit width. We find no evidence for systematic offsets related to the grid points. Instead, we see a scatter about 0 of 50 and 100 GeV/c^2 for the fixed and floating width fits respectively.

We now turn to the second class of tests. We generate 182 samples of 600 events [52]. We fit each. Fig. 67 shows the distribution of fit masses and statistical uncertainties when the width is fixed to the generated value. The mean of the distribution of masses is another test of the reliability of the fitting procedure. The spread in fit masses should reflect the statistical precision possible with our data sample. Finally, the mean uncertainty of the fits and the spread in fit masses should be consistent with each other. Table 13 summarizes the results. The agreement between mean fit mass and width and the W mass and width used to generate the samples is excellent, and the various mea-

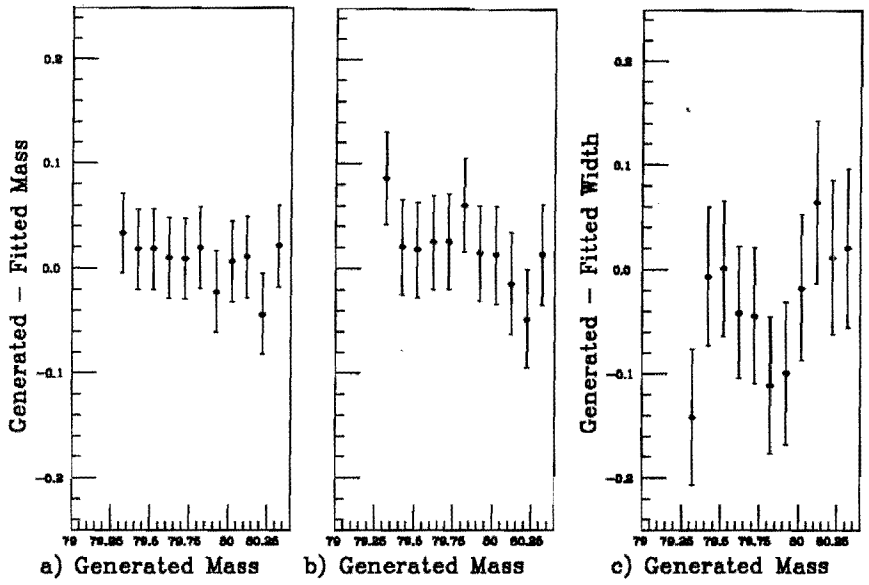

Figure 66: Difference between a) generated and fit m_W with Γ_W fixed to the generator input, b) generated and fit m_W with Γ_W floated, and c) generated and fit Γ_W. These are plotted as a function of the generated m_W. Masses are given in units of GeV/c^2 and widths in GeV.

sures of uncertainty are also consistent (especially after smoothing the lineshapes). We will also find that the statistical uncertainties from the fits to the W decay data sample are consistent with these results (Section 15).

As a final check of our smoothing procedure, we fit each of these samples to two independent lineshapes and compare the fit masses and widths. These results are summarized in Table 14. We see, as before, that smoothing removes the jitter. The spread in the distribution of the difference in fit mass from the two sets of lineshapes is reduced from 178 to 15 MeV/c^2.

Although this discussion has concentrated on the measurement of m_W with Γ_W fixed, the statements made are true for simultaneous fits to the two parameters. The size of various effects is larger. The statistical uncertainties on the measurements for the two parameter fits are larger than that for a single parameter fit. The statistical precision with which Γ_W is determined is especially poor. Given the statistical uncertainties of the

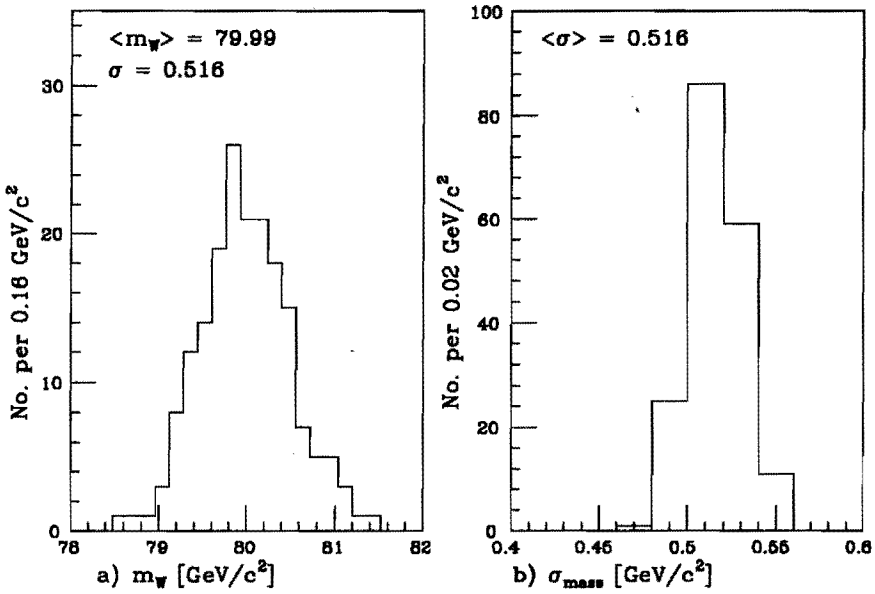

Figure 67: Distribution of a) fit m_W with Γ_W fixed to the generator input and b) statistical uncertainty on m_W from the fit. The distribution contains 182 samples of 600 events generated with $m_W = 80.0$ GeV/c^2 and $\Gamma_W = 2.2$ GeV.

measurements, we can make the same statements for the fits to the W width that we made for the fits to the mass. There are no systematic offsets inherent in the fit to the width. The statistical properties of fits to many Monte Carlo samples are consistent with each other. The fit widths agree with that used in generating the Monte Carlo samples. After smoothing the lineshapes, the jitter is gone.

14.4 Correlation between Mass, Width, and Resolution

Fig. 68 shows the coupling between the fit mass and width. We measure $\frac{\Delta m_W^{fit}}{\Delta \Gamma_W^{constrained}} = -0.33$ (m_W in GeV/c^2 and Γ_W in GeV). It is important to remember that the fit "width" reflects the width of the kinematic distributions. As such, it is a convolution of several effects. The detector resolution, the distribution of p_t^W, and the Standard Model width of the W in the Breit-Wigner all contribute to the overall width of the distributions. It is, perhaps, false advertising to call the fit parameter Γ_W. (It is, however, convenient.) Any mismeasurement of the detector resolution or p_t^W couples to the width of the distribution

	Unsmoothed		Smoothed	
	Mean	σ	Mean	σ
m_W; Γ_W fixed	79.99 ± 0.039	0.522 ± 0.027	79.99 ± 0.038	0.516 ± 0.027
Error on m_W	0.502 ± 0.003	0.045	0.516 ± 0.001	0.015
m_W; Γ_W floated	79.96 ± 0.045	0.602 ± 0.032	79.98 ± 0.044	0.593 ± 0.031
Error on m_W	0.552 ± 0.008	0.111	0.589 ± 0.007	0.091
Γ_W	2.38 ± 0.076	1.03 ± 0.054	2.44 ± 0.072	0.97 ± 0.051
Error on Γ_W	1.03 ± 0.029	0.387	1.08 ± 0.024	0.319

Table 13: Comparison of fit masses and widths of 182 Monte Carlo samples with statistics comparable to that in the data with and without smoothing. All masses are given in units of GeV/c^2 and widths in GeV.

	Unsmoothed		Smoothed	
	Mean	σ	Mean	σ
Difference in m_W; Γ_W fixed	0.008	0.178	-0.008	0.015
Difference in m_W; Γ_W floated	-0.020	0.220	-0.007	0.099
Difference in Γ_W	0.035	0.395	0.025	0.235

Table 14: Comparison of fit masses and widths found for lineshapes generated with different random number seeds. Fits are done to the 182 Monte Carlo samples with and without smoothing. All masses are given in units of GeV/c^2 and widths in GeV.

which couples to the mass through the W width, Γ_W. We limit this effect on our final answer by fixing Γ_W to the Standard Model value of 2.1 GeV.

14.5 Summary of Fitting Systematics

At the level of 20 MeV/c^2, we find no systematic offsets in the W mass associated with the mechanics of fitting, nor is there any evidence for jitter. When fitting large Monte Carlo samples, only a residual scatter of 50 MeV/c^2 about the W mass used to generate the samples remains. The varying of the fit mass with fit range is not an additional systematic; it merely reflects the statistical fluctuations inherent in adding or subtracting events in the tail of the distribution. We thus assign a 50 MeV/c^2 uncertainty due to the

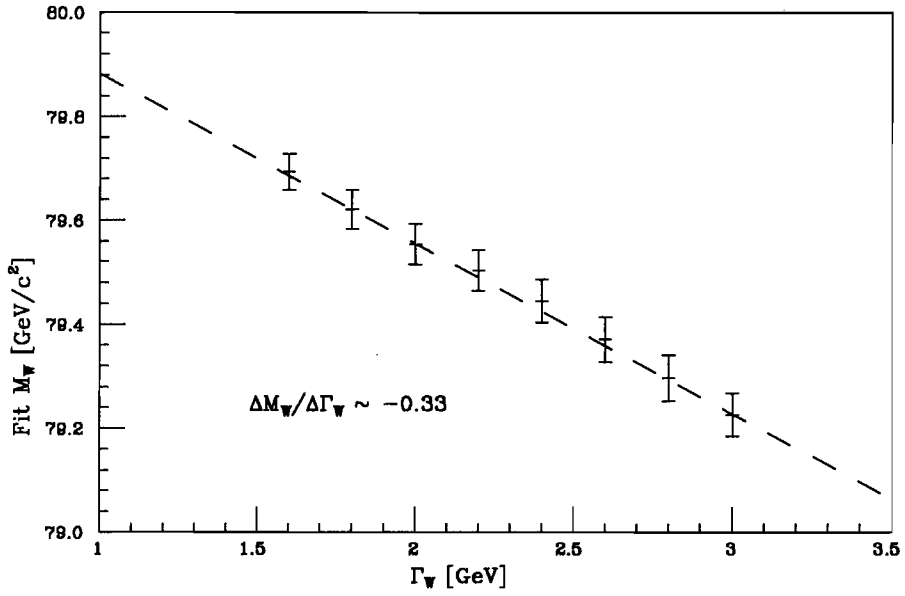

Figure 68: Fit mass as a function of the width. The sample was generated with a mass of 79.5 GeV/c^2 and width of 2.2 GeV. Γ_W was then constrained to various values and the mass alone was fit. The dashed line is a linear least-squares fit to the data. The slope is $-0.33\frac{GeV/c^2}{MeV}$.

characteristics of the fitter.

15 Results, Corrections and Systematics

The result of the fit to the transverse mass distribution of Fig. 69 with Γ_W constrained to 2.1 GeV is 79.78±0.53 GeV/c^2. If both mass and width are fit, m_W = 79.69 ± 0.65 GeV/c^2 and $\Gamma_W = 2.3 \pm 1.1$ GeV. The uncertainties given are statistical uncertainties only. Note that these uncertainties are consistent with those observed in the distributions of the fits to many Monte Carlo samples described in Section 14.3.

15.1 Corrections

These results need to be corrected for inner bremsstrahlung. The muon, accelerated during the decay of the W, will radiate a photon with some probability. This QED process is calculable [53]. The photon energies are typically small, but the effect is non-

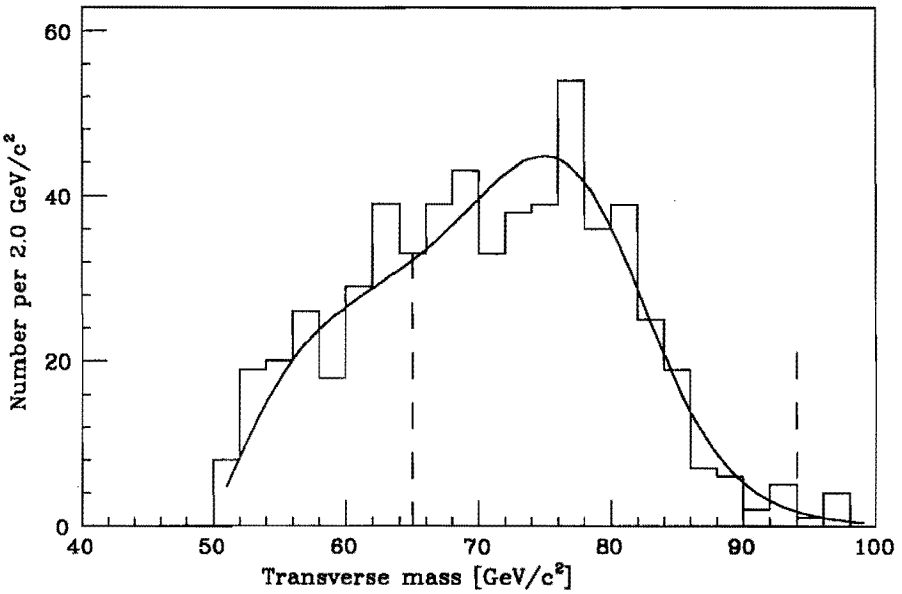

Figure 69: The transverse mass distribution for all W $\rightarrow \mu\,\nu$ candidates. Overlaid is the best fit to the data. Indicated with dashes is the range of transverse mass used in the fit. The transverse momentum spectra for muon and neutrino are plotted in Fig. 75.

negligible. The momentum of the muon as measured in the tracking chamber will be smaller than the momentum of the muon-photon system produced by the W decay. The measured muon momentum spectrum is correspondingly softened – leading to a small shift in the observed W mass. A Monte Carlo simulation [54] is used to predict the angles and energies of radiated photons. We simulate the effect of the cuts imposed during W decay candidate selection. This has one important consequence. The largest effect on the p_t of the muon occurs if the radiated photon is collinear with the muon. These events are preferentially rejected by our cut on the total energy in the muon tower: the larger the photon energy and the more collinear with the muon, the greater the probability that the event is not included in the W decay sample. This reduces the effect of final state radiation on the W mass measurement. For events which pass the data selection cuts, the difference between muon and photon azimuthal and polar angles is plotted in Fig. 70, while the photon energy spectrum is plotted in Fig. 71. We measure the difference between the invariant mass of the muon-photon-neutrino and the muon-neutrino system.

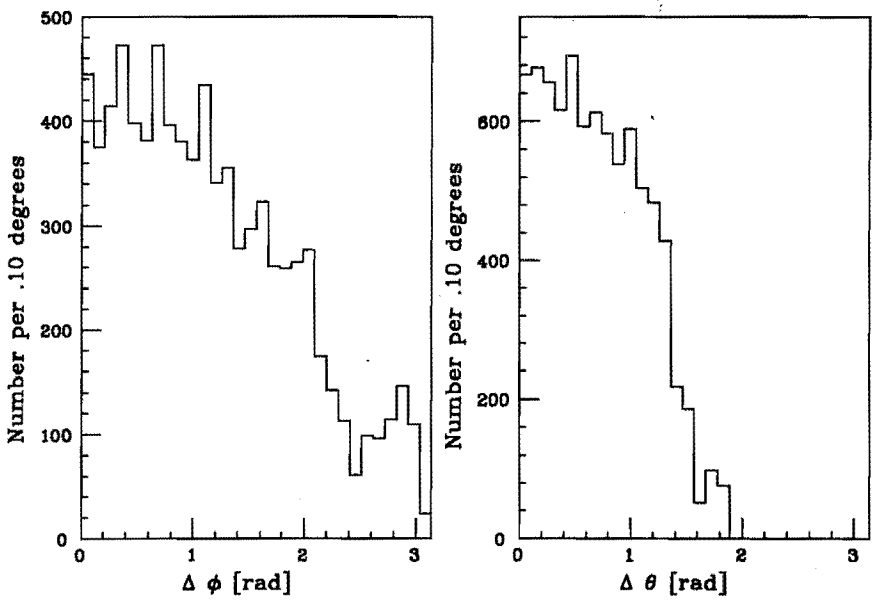

Figure 70: Simulated distributions of the difference in a) ϕ and b) θ between the muon and photon directions predicted by our simulation of inner bremsstrahlung. Note that these distributions are for events which pass the data selection cuts. Thus, the most collinear photons are excluded.

We also measure the difference in m_t, p_t^μ and p_t^ν. Results are summarized in Table 15.

15.2 Backgrounds

In Section 9.2, we discussed the background in the W sample. We now need to estimate the effect of this background on the W mass measurement.

The sequential decay of τs from Ws ($W^+ \rightarrow \tau^+ \nu_\tau$; $\tau^+ \rightarrow \mu^+ \nu_\mu \bar{\nu}_\tau$) into muons mimics the direct decay of $W \rightarrow \mu\nu$. However, the resulting m_t distribution is softer (see Fig. 33) because the average p_t of the muon from the decay of a τ is much smaller than that of the muon from the decay of a W. Although high p_t backgrounds have a larger impact on the W mass measurement, a softening of the kinematic spectra of the $W \rightarrow \mu\,\nu$ sample due to the addition of muons from the sequential decay of τs could lower the measured W mass. This effect was measured in [42] for the CDF electron analysis. A Monte Carlo simulation of the process leads to an estimate of 4 events in the 1130 event $W \rightarrow e\,\nu$

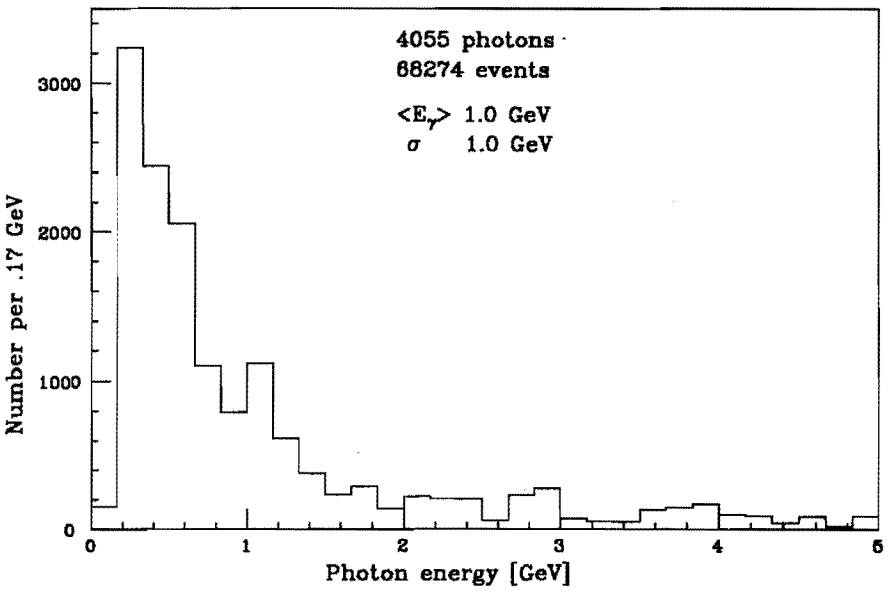

Figure 71: Simulated distribution of energies of the radiated photons passing the data selection cuts.

decay sample. Only 1.5 events are in the fit range ($m_t \geq 65$ GeV/c^2), producing to a 4 MeV shift in W mass. The small difference between electron and muon masses relative to the tau mass allows us to extrapolate this measurement to the muon analysis. The p_t spectra of muons from sequential decays will be little different from that of electrons. The acceptance for these sequential decays is even smaller for muons. The effect of this background on the W mass measurement for muons is, therefore, negligible.

Our belief that there is little low p_t background in our decay sample is supported by the agreement between the kinematic distributions predicted by the Monte Carlo and those of the W decay sample below the fit range (see, for example, the p_t spectra of the muon and neutrino plotted in Fig. 75). This region was not included in the fit; and the Monte Carlo does not include any simulation of background; yet there is no evidence for excess events.

Z events, where one of the muons is not found, mimic W events. This background could have a large effect on the W mass, as the muons from Z decay can have higher

Variable	Mean Shift in Variable	Correction to Fit Mass
m	123 $\pm$ .003 (stat.) MeV/c^2	
m_t	102 $\pm$ .002 (stat.) MeV/c^2	123 $\pm$ 12 MeV/c^2
p_t^μ	66.7 $\pm$ .002 (stat.) MeV/c^2	80 $\pm$ 8 MeV/c^2
p_t^ν	36.1 $\pm$ .001 (stat.) MeV/c^2	44 $\pm$ 4 MeV/c^2

Table 15: Effect of inner bremsstrahlung on the kinematic variables in this analysis. The softening of the m_t spectrum translates into a shift in the measured mass of the decaying W. From the shift in the invariant mass, we conclude that a 102 MeV/c^2 shift in the mean m_t requires a correction to the mass found by fitting the m_t spectrum of 123 $\pm$ 5 MeV/c^2. For the other two kinematic variables, we assume the mean shift in the variable must be scaled by the same ratio to find the correction to the W mass found by fitting that variable. We assign an overall uncertainty of 10% to our calculation.

momentum than those from W decays. This could effect the characteristics of the falling edge of the kinematic spectra. However, the cross section for Z decay is 10 times lower than that for W decay [55]. The cross sections for W and Z decay to electrons are plotted in Fig. 72.

To simulate the background from $Z \rightarrow \mu\mu$, we simulate the production of Zs and their decay to muons and require that one muon hit the muon chambers ($|\ \eta\ | < 0.63$). We then make the conservative assumption that the second track will be found if it passes through all layers of the CTC. The background consists of those events where the second track is not found ($|\ \eta\ | > 1.0$). From this we infer the shape of the background spectrum, which is plotted in Fig. 73. The efficiency for finding one muon (estimated from our W Monte Carlo) is 20%. An upper limit on the efficiency for finding either muon from the Z is 40%. Convolving this with the difference in cross section, we estimate that no more than 4% of our W sample is Zs. The Zs which survive tend to have a soft m_t distribution similar to that of the τs, minimizing the effect on the W mass measurement. The soft Z background is due to the requirement that one decay muon go forward or backward in the detector. This implies a low m_t Z. We add a 4% background consistent with the shape of the Zs to the W decay sample and find that this changes the fit mass by 20 MeV/c^2.

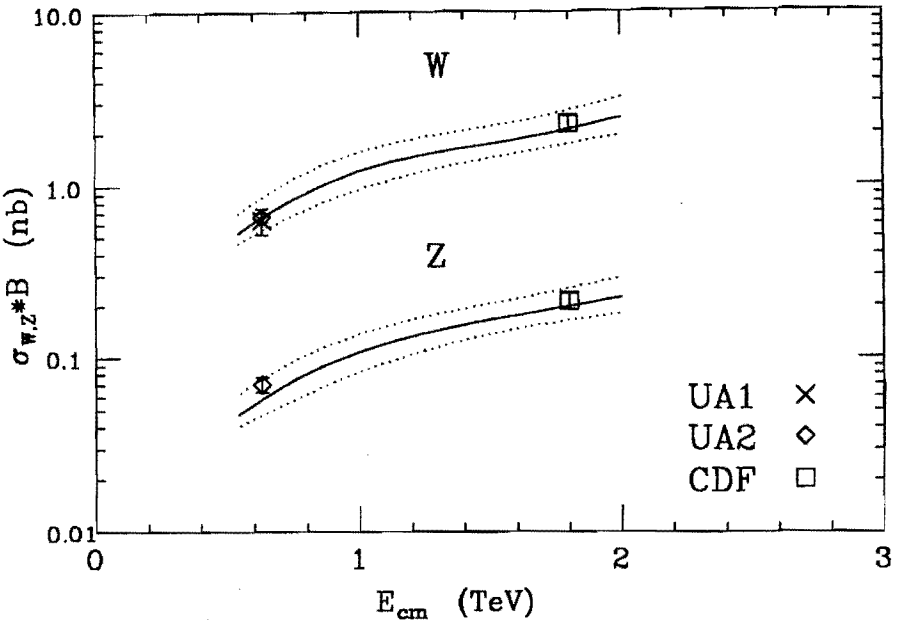

Figure 72: The cross section for W and Z decay to electrons measured at CDF [56]. The cross sections are $\sigma_W = 2.26 \pm 0.04 \pm 0.23$ and $\sigma_Z = 0.211 \pm 0.012 \pm 0.018$. The first uncertainty is statistical and second systematic. Theoretical predictions are superimposed.

Cosmic rays are also a significant background to the muon sample. We examine the efficiency of our cuts designed to remove cosmic rays using real cosmic ray data. We estimate that the number of cosmic rays which remain in the muon sample is less than 0.3. The spectrum of cosmic rays which are selected by the cuts we impose in selecting W decays is roughly flat (see Fig. 74) as opposed to the rapidly falling $1/E^2$ spectrum of generic cosmic rays (see Fig. 38). We estimate an upper limit to the effect of the cosmic ray background by adding a 1% flat background to the muon sample. This increases the fit W mass by 110 MeV/c^2. This is a conservative estimate. The spectrum is not flat, and 1% is 20 times the estimated cosmic ray background. This does allow for uncertainties in the estimate of the cosmic ray removal efficiency and for any residual backgrounds which have not been explicitly analyzed. We take 110 MeV/c^2 as the uncertainty in the W mass due to background in the muon sample.

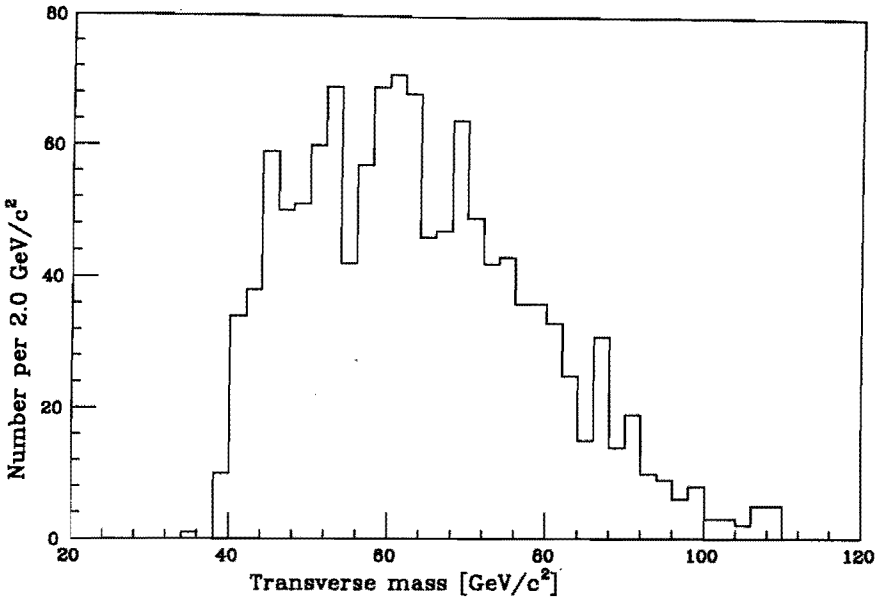

Figure 73: p_t spectrum of simulated Zs with one leg in the central region, $|\eta| < 0.63$, and one not passing entirely through the tracking chamber, $|\eta| > 1.0$. This is the shape of the Z background in the W sample.

15.3 Summary of Uncertainties

The nontrivial uncertainties for the W mass determination are summarized in Table 16. The statistical uncertainty is 530 MeV/c^2. The uncertainty due to the momentum scale is 160 MeV/c^2 and all other systematics are 310 MeV/c^2: 100 MeV/c^2 for parton distribution functions, 130 MeV/c^2 for the underlying event model, 240 MeV/c^2 for parallel energy balance, 110 MeV/c^2 for background, and 50 MeV/c^2 for fitter systematic.

15.4 Systematic Checks

As a check we also measure the W mass from the fits to the muon and neutrino p_t spectra in the $W \rightarrow \mu\nu$ decay sample. These are shown in Fig. 75. The lepton p_t spectra are particularly sensitive to the the input p_t^W distribution. We measure the systematic uncertainty of the W mass measurement from fits to the p_t spectra as described for the measurement from the fit to the m_t spectrum and find systematic uncertainties of

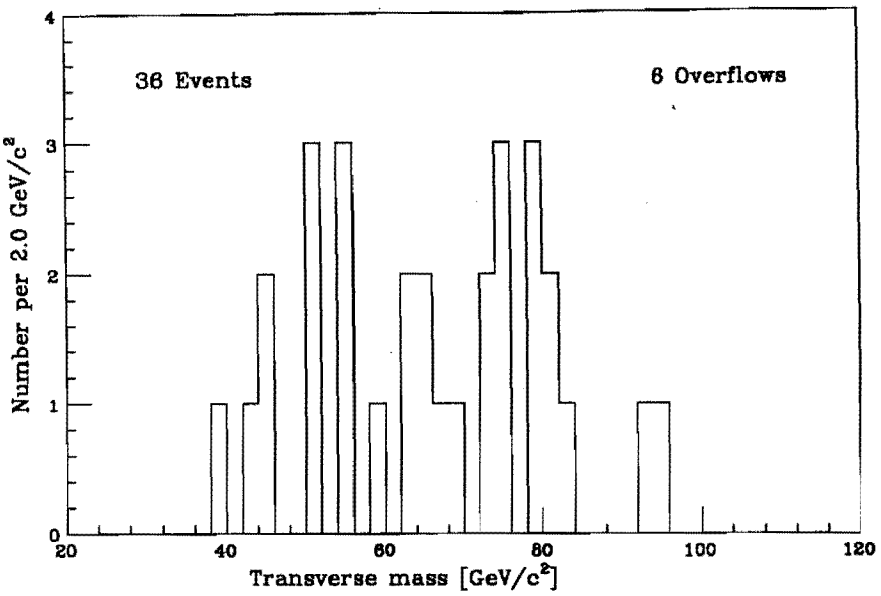

Figure 74: Transverse mass spectrum of cosmic rays removed from the W sample.

250 MeV/c^2 for the fit mass from the muon p_t spectrum and 330 MeV/c^2 for the fit mass from the neutrino p_t spectrum due to variation in the underlying event model and the input p_t^W distribution. The calibration, proton structure, background and fitting uncertainties effect the lepton spectra in the same way as the m_t spectrum, while parallel energy balance does not affect the fits to the muon p_t spectra. We obtain 300 MeV/c^2 overall systematic uncertainty on m_W measured from the fit to the muon p_t spectrum. This fit gives $m_W = 79.44 \pm 0.56(\text{stat.}) \pm 0.30(\text{syst.})$ GeV/c^2. Fitting the neutrino p_t spectrum, we find $m_W = 79.89 \pm 0.78(\text{stat.}) \pm 0.47(\text{syst.})$ GeV/c^2. The neutrino distribution is quite sensitive to the modelling of the underlying event and detector resolution.

The consistency of the W mass found from fits to the m_t, p_t^μ and p_t^ν spectra lend credibility to our results. As discussed in Section 10, we use the fit to the m_t spectrum for our final result. After adding the radiative correction, the final result is

$$m_W^\mu = 79.90 \pm 0.53(\text{stat.}) \pm 0.31(\text{syst.}) \pm 0.16(\text{scale}) \text{ GeV/c}^2 . \quad (26)$$

Uncertainty	Muons	Common
Statistical	530 (650)	
Momentum scale	160	160
Systematics	310	150
1. Proton structure	100	100
2. Resolution, W p_t	130	100
3. Parallel balance	240	
4. Background	110	
5. Fitting	50	50
Overall	640 (740)	

Table 16: Uncertainties in measuring the W mass. All uncertainties are quoted in units of MeV/c^2. In parenthesis are the statistical (and overall) mass uncertainties if Γ_W is determined in the fit as well. The scale uncertainty is in common with the Z mass measurement [5]. The uncertainties which are common to both electron and muon analyses are listed.

16 Implications of the Measurement

The result from the muon analysis can be compared to the result from the CDF analysis of $W \to \ell\nu$ decays [42]:[17]

$$m_W^e = 79.69 \pm 0.35(\text{stat.}) \pm 0.24(\text{syst.}) \pm 0.34(\text{scale}) \text{ GeV/c}^2. \quad (27)$$

The two CDF W mass measurements may be combined. There are common uncertainties in the two analyses which were noted in Table 16. Keeping track of common uncertainties, we combine the two measurements:

$$m_W^{CDF} = 79.78 \pm 0.44 \text{ GeV/c}^2. \quad (28)$$

This can be compared to the recent UA2 result [12]:

$$m_W^{UA2} = 80.79 \pm 0.31(\text{stat.}) \pm 0.21(\text{syst.}) \pm 0.81(\text{scale}) \text{ GeV/c}^2 . \quad (29)$$

[17]The result of [42] has been updated to include smoothing of the lineshapes prior to fitting [52].

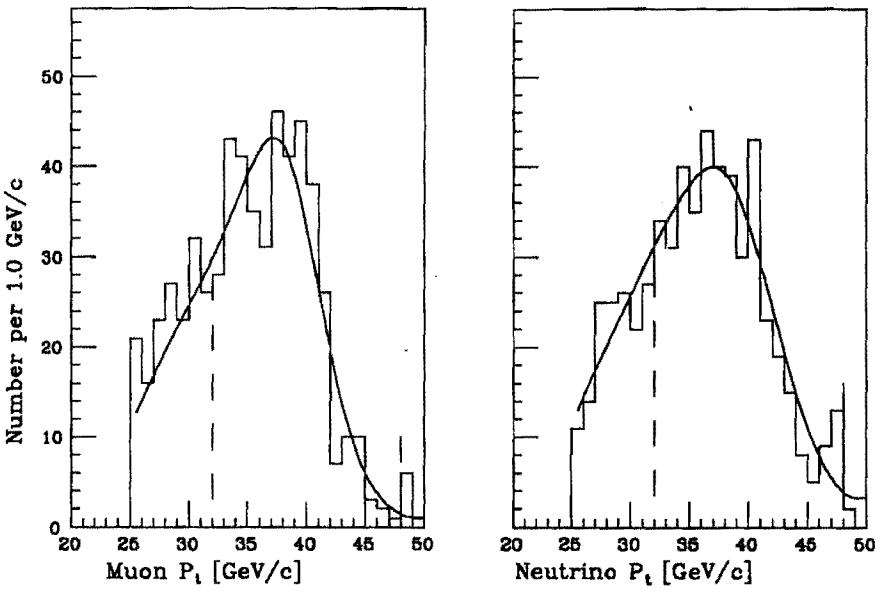

Figure 75: a) The muon p_t distribution selected for measuring the mass. b) The corresponding neutrino p_t distribution. The best fit to the data is overlaid in each case.

The UA2 measurement of the W mass scaled to a LEP/MARK II Z mass value of 91.150 ± 0.032 GeV/c^2 is $m_W = 80.49 \pm 0.49$ GeV/c^2 [12]. For a better comparison to the UA2 measurement, we make the same scaling. Our uncertainties in energy scale cancel, as they are common to both the W and Z mass measurements; however, the statistical uncertainty on our Z mass measurements must be included. The mass, scaled to the LEP Z mass, is $m_W = 79.91 \pm 0.45$ GeV/c^2.

The mass of the W is a sensitive probe of the electroweak sector of physics. The first-order corrections to the W mass are dependent on the masses of the as yet unfound top quark and Higgs particle though radiative loops (see Section 2). The on-shell definition of the electroweak mixing angle as

$$\sin^2 \theta_W \equiv 1 - \frac{m_W^2}{m_Z^2} \tag{30}$$

introduces the masses of the top quark and Higgs boson into the measurement of $\sin^2 \theta_W$ as well. We extract $\sin^2 \theta_W$ separately for electrons and muons to minimize the impact of the respective scale uncertainties. From the definition above and using the CDF

measurement of the Z mass, we obtain 0.235 ± 0.010 and 0.224 ± 0.014 for $\sin^2\theta_W$ from the electron and muon data respectively. The uncertainty in the electron measurement includes (in quadrature) ± 0.0015 as a systematic effect of possible nonlinearity in the calorimeter electron energy measurement. The two results may be combined to give

$$\sin^2\theta_W = 0.231 \pm 0.008 \quad . \tag{31}$$

This may be combined with the UA2 result of 0.220 ± 0.010 [12] to give an overall result from direct mass measurements in hadron collisions of 0.227 ± 0.006.

The implications of this measurement on the masses of the top quark and Higgs particle are summarized in Fig. 76. The collider measurements of the weak mixing angle

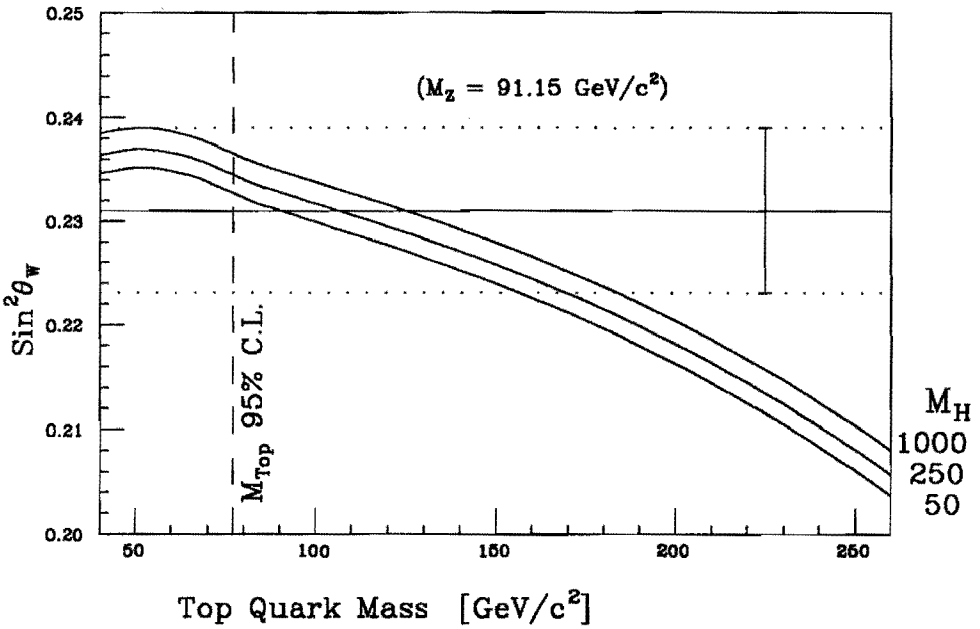

Figure 76: Comparison of the CDF weak mixing angle measurement with radiative predictions [13] using a Z mass of 91.15 GeV/c^2, as a function of assumed mass for the top quark. The lower limit top mass 95% CL is from [57].

are applied to first-order calculations of the radiative corrections to the W mass [13] using a Z mass of 91.15 GeV/c^2. The results are consistent with the absence of top in the CDF searches [57] [58]. The allowed region, for a Higgs mass of 1000 GeV/c^2, corresponds

to a top mass below 230 GeV/c^2 (95% CL) for CDF data alone or for CDF and UA2 combined.

17 The Future

CDF is preparing to take more data in the spring of 1991. The direct search for the top quark will clearly benefit from improved statistics. One can consider what implications more data has for the measurement of m_W.

More data will reduce the statistical error by $\frac{1}{\sqrt{n}}$ where n is the number of events. We expect roughly 4 times as much data as was taken in the last run. This would mean 5 100 $W \rightarrow e\,\nu$ decays from which we would predict a reduction in the statistical error on the W mass measurement from 320 to 150 MeV/c^2. In addition to the increase in data, the muon analysis benefits from an upgrade which increases the coverage from $\mid \eta \mid < 0.63$ to $\mid \eta \mid < 1.0$ and places an additional set of muon chambers behind additional hadronic absorbtion lengths of steel to reduce the problem of punchthrough. From the additional coverage, we predict roughly 7 times as many $W \rightarrow \mu\,\nu$ decays at the end of the next run (4 500 in all) which will reduce the statistical error from 530 to 200 MeV/c^2.

The systematic error will also be reduced by additional statistics. For an analysis done in the same manner, one would expect that more data would lead to improved constraints on the parameters of the Monte Carlo, especially those that come from W or Z decays. (It is unclear what benefit there is in additional jet or minimum bias data.) The input p_t^W, the recoil degradation factor, the jet resolution, and the muon momentum resolution should all be significantly better constrained with more data. We blithely ignore that not all parameters may be equally affected and assume that the systematics of the underlying event model and p_t^W scale with data. The 130 MeV/c^2 uncertainty associated with this aspect of the analysis is reduced to 60 after the next run. The constraint on the parallel energy balance should also scale (240 goes to 90 MeV/c^2), but let us assume that the muon upgrade will eliminate the need to remove pion punchthrough with a di-jet cut.

This systematic then disappears. With the reduction in these errors, one must make a more careful estimate off the remaining background. Additional data does not reduce the size of the uncertainty; however, with some effort, one could probably demonstrate that a 1% flat background is an overestimate of the residual background, perhaps by a factor of 2 to 4. The fitter systematic and the systematic due to choice of proton distribution functions are unchanged by additional data.[18] All of our systematics are now of the order of 50 MeV/c^2. The total systematic, excluding scale uncertainties, is 110 MeV/c^2. These estimates are summarized in Table 17.

Uncertainty	1990	1991
Statistical	530	200
Momentum scale	160	40
Systematics	310	110
1. Proton structure	100	60
2. Resolution, W p_t	130	60
3. Parallel balance	240	0
4. Background	110	60
5. Fitting	50	50
Overall	640	230

Table 17: Uncertainties in the W mass measurement for a $W \rightarrow \mu\,\nu$ decay sample of 4500 Ws (1991). The uncertainties for the analysis presented in this thesis (1990) are repeated for comparison. All uncertainties are quoted in units of MeV/c^2.

One can hope that the scale certainties will be reduced with additional data, but it appears that hard work will achieve that even before more data comes along. Recent work has reduced the energy and momentum scale uncertainties for muons and electrons to 100 and 180 MeV/c^2, respectively. Scaling this for additional data, we would predict 40 and 80 MeV/c^2 for muons and electrons after the next run.

The overall uncertainty on the W mass from muons would then be 230 MeV/c^2; for

[18]We expect these systematics to be reduced. The size of the reduction is difficult to quantify. More powerful computers will reduce the fitter systemic as the number of simulated events increases. We expect our knowledge of the parton distribution functions will improve with time as well.

electrons, 200 MeV/c^2 The uncertainty on the combined W mass measurement would then be 200 MeV/c^2 from which we would deduce a 95% confidence level bound on the mass of the top quark of 150 GeV/c^2.

A The CDT Trigger Electronics

We describe the level 1 trigger card used for the CDF Central Drift Tube array. The design of the level 1 trigger card is such that it is highly versatile. PAL multiplicity logic units on the card are controlled by addressable R/W registers and allow triggering on single ganged drift tube pairs or groups of ganged drift tube pairs anywhere in the 2016-tube CDT array, a feature useful for calibration and debugging purposes. The same registers also allow triggering on prompt signals anywhere in the CDT array from $\bar{p}p$ collisions or from cosmic rays. Thus the CDT level 1 trigger card can be used for physics purposes as well as for monitoring and calibration purposes. The CDT level 1 trigger card was designed entirely on the University of Illinois DAISY CAD/CAE system. It was thoroughly simulated in software before being built. Twenty CDT RABBIT level 1 trigger cards were mass-produced with no prior building or testing of a prototype CDT level 1 trigger card. No problems or difficulties of any significance were encountered in the installation and use of the trigger card.

A.1 Introduction

The CDF Central Drift Tube level 1 trigger is designed for several purposes. The first is to provide for triggering on individual Fe^{55} sources embedded in each tube of the CDT array [19] for calibration. The second is to provide monitoring of drift tube counting rates, hit participations, hit efficiencies, etc. The third is to provide prompt hit information to the level 0, level 1, and level 2 physics triggers for CDF. The use is to enable use of the CDT array as a 90° luminosity monitor for $\bar{p}p$ collisions.

A.2 System Description

The CDF Central Drift Tube array consists of 2016 12.7 mm diameter 3 m long ultra-thin walled stainless steel drift tubes operated in the limited streamer mode [19]. The 2016 drift tubes are arranged in three close-packed layers of 672 tubes per layer. From charge

division and drift time measurements, the CDT array provides high-accuracy $r-\phi-z$ information at a radius of 1.4 m for tracking charged particles inside a 1.5 T magnetic field volume produced in the central region (pseudorapidity range $-1 < \eta < 1$) from $\sqrt{s} = 1.8$ TeV $\bar{p}p$ collisions.

The CDT array is divided into 84 subsections called "HV Pods". Each pod consists of 24 drift tubes in three layers of 8 tubes sharing an HV supply channel. Within a given layer, pairs of drift tubes, separated by a lateral distance of 8 tubes are electrically ganged together[19]. The drift tube signals from 48 tubes in a CDT HV pod pair are sent to three RABBIT ADC/TDC cards [30] via 2, 15 m long, 50-ohm, micro-coaxial 26-conductor flat cables. There are a total of 126 RABBIT ADC/TDC cards in the eight crates of the CDT RABBIT readout system. Pairs of CDT RABBIT crates are located at the four corners of the east endwall of the CDF central detector.

For each ganged drift tube pair in the CDT array, the RABBIT ADC/TDC card will assert a prompt TTL level upon reception of a streamer pulse from the tube pair. The TTL level is a maximum of $1.2\ \mu s$ duration. The leading edge of the TTL level has maximum time jitter of 130 ns relative to e.g. $\bar{p}p$ bunch crossing time due to the variation in arrival times of charge from ionization drifting in to the anode wire. The electron drift velocity is approximately $50 \mu m/ns$ in argon-ethane $50\%-50\%$ gas bubbled through isopropyl alcohol at $+5.0^{\circ}$ Celsius. The TTL levels for hit tubes remain high until a reset pulse (clear and strobe) is issued by the CDF Trigger Supervisor to the entire RABBIT system.

Each RABBIT ADC/TDC card has eight such prompt TTL outputs, servicing eight ganged drift tube pairs. The prompt TTL hit information is sent via a twisted-pair flat cable from the 8-channel front panel connector on the RABBIT ADC/TDC card to an input connector on the CDT level 1 trigger card. Each CDT level 1 trigger card has nine 8-channel prompt TTL hit input sections. There are a total of 16 CDT level 1 trigger

[19]This was done to reduce the number of channels of electronics needed for detector readout.

cards (two per RABBIT crate) for the entire CDT RABBIT readout system.

The 24 ganged drift tube pairs in a CDT HV Pod pair are geometrically clustered into 6 groups of contiguous 4-tube pair clusters, as shown in Fig. 77, for the purposes of

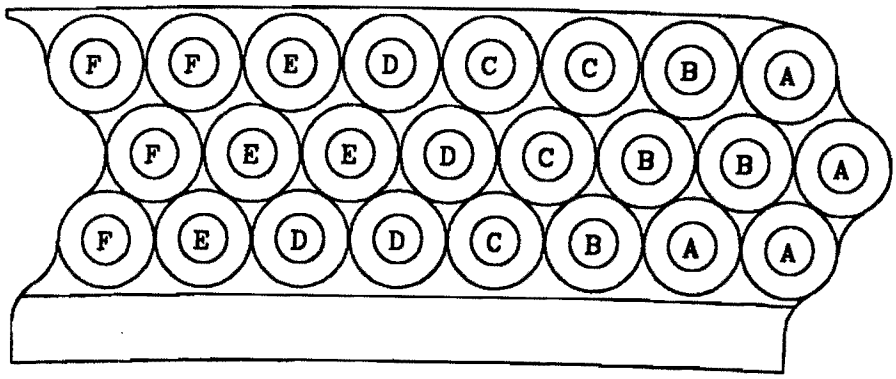

Figure 77: End View of a CDT HV pod. The 4-tube trigger clusters are shaded. Note that the tubes in this pod are ganged with the corresponding tubes in the adjacent pod.

demanding an N/4-fold hit coincidence within a given 4-tube ganged pair cluster. The prompt TTL hits for each 4-tube ganged pair cluster are input to a MMI 16C1 PAL (Programmable Array Logic) integrated circuit [59]. Each individual PAL has 4 input disable lines, one disable line for each prompt TTL input. There are two input control lines to the PAL to define the hit multiplicity requirement per 4-tube ganged pair cluster of ≥ 1, ≥ 2, ≥ 3, or $= 4$ -fold hit coincidences. An additional input control line (global PAL disable) is used to define a test mode for the PAL. One state enables normal operation as described above, while the other disables the normal inputs to the PAL and uses the input disable lines as inputs. This allows the PAL logic to be tested *in situ*. There are 18 PAL's on each CDT RABBIT level 1 trigger card.

As shown in Fig. 78, the nine 8-fold prompt TTL inputs from the CDT RABBIT ADC/TDC card are grouped together in three subsections of 24 prompt TTL inputs on

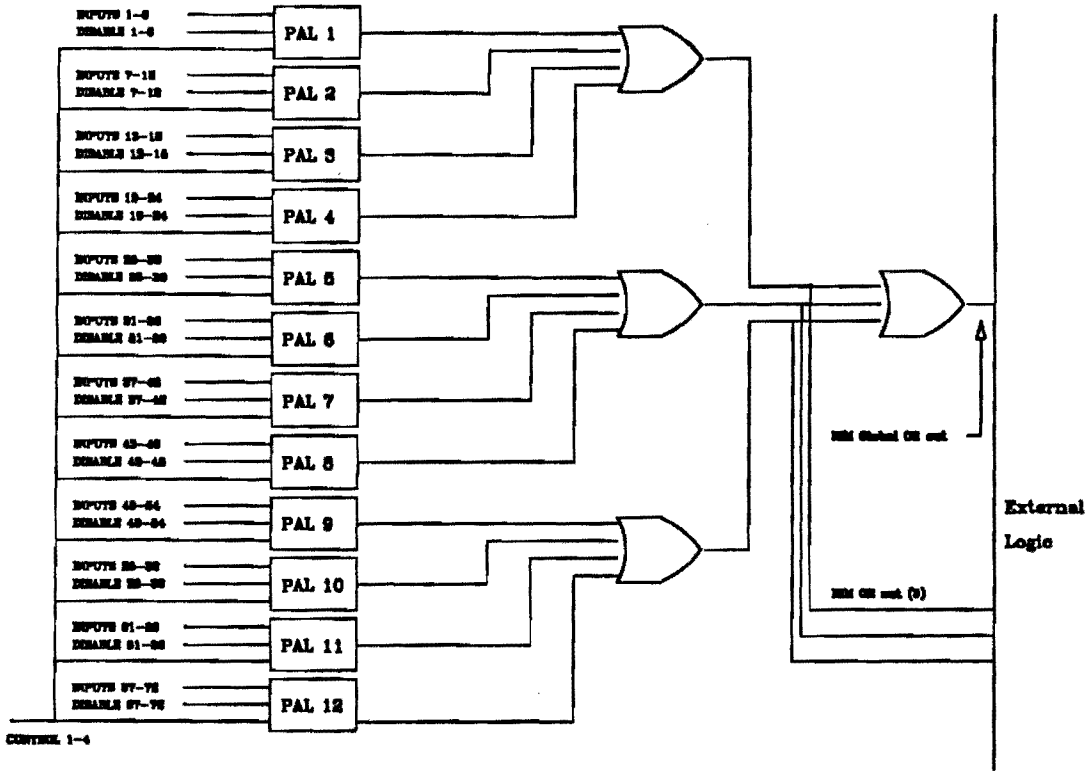

Figure 78: The level 1 trigger card logic.

the CDT RABBIT level 1 trigger card. The hit multiplicity outputs from each of the six PAL's within a given subsection on the trigger card are OR'ed together and have a NIM-level output. In addition, there is also a Global NIM-level OR on the CDT level 1 trigger card consisting of the OR of the three subsection OR's on the card. Thus, there are a total of 42 NIM-level trigger OR outputs, one for each CDT HV Pod pair in the CDT array, and a total of 16 Global NIM-level OR outputs.

There are 45 8-bit registers on the CDT level 1 RABBIT trigger card. The first 32 such registers 0-31 are read-only and contain the contents of 32 8-bit ASCII characters for PROM ID information (containing e.g. RABBIT card type, card serial number, etc.). Register 32 has read/write capability and contains the 8-bit control word for PAL hit multiplicity/Global PAL disable. There are nine control registers 33-41 which have read/write capability and contain the 8-bit control words for PAL input disable lines, one for each prompt TTL input. The three registers, 42-44, are for diagnostic and testing

purposes; they are read-only and contain the logic states of the outputs of the six PALs in each of the three subsections on the trigger card as well as the the logical OR of the 6 outputs.

Fig. 79 shows the intermediate trigger logic between the CDT RABBIT level 1 trigger

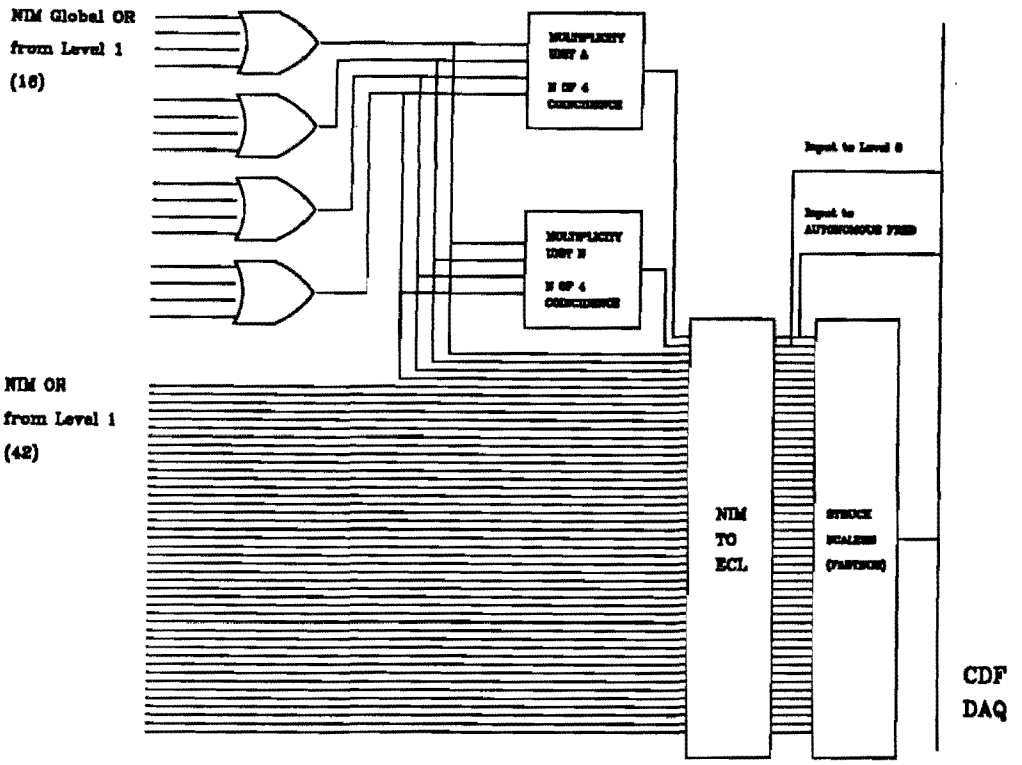

Figure 79: CDT trigger system logic. Outputs from the 42 level 1 cards are used to makes trigger decisions. These decisions are then input to the CDF online trigger system.

cards and the CDF FASTBUS trigger electronics. The 42 NIM-level OR outputs and the 16 NIM level Global OR outputs from the CDT level 1 trigger cards are transported to the CDF trigger counting room via 100 m long RG-58 coaxial cables. The Global NIM OR output signals are input to two LeCroy 429A logic fan-in/fan-out 16 channel modules operated in 2x8 mode. The NIM-level outputs from the four independent 8-fold NIM fan-in subsections (corresponding to approximately 90 degrees in phi) are in turn input to a LeCroy 365AL majority logic NIM module. One half of this NIM module is normally operated in single-fold coincidence mode. This is the CDT L1 trigger and is presently

used for taking Fe^{55} source calibration and pulser data. Operated in the 2, 3, or 4-fold coincidence mode it may also be used for data-taking with $\bar{p}p$ collisions or cosmic ray triggers. The other half of the module is operated in two-fold coincidence mode for use as the CDT L0 trigger. The NIM outputs of the LeCroy 365AL majority logic modules are level-shifted to differential ECL and input to the CDF FASTBUS Trigger Modules Autonomous FRED [26] (CDT L1) and to CDF FRED via the level 0 input board (CDT L0).

The 42 NIM OR CDT level 1 trigger output signals are level-shifted to differential ECL signals via LeCroy 4616 16-channel ECL-NIM-ECL converters and then input to two Struck STR-200 FASTBUS scalers, along with the four level-shifted outputs from the LeCroy 429A logic fan-in/fan-out modules and the outputs of the LeCroy 365AL majority logic modules (CDT L0 and L1). These FASTBUS scalers measure the rates from the CDT trigger system and are read out in the CDF event stream. Although not specifically gated to do so, the scalers, are in fact, counting only hits that occur in the R/S gate. Thus, counts from sources other than $\bar{p}p$ collisions, such as cosmic rays or Fe^{55} sources, are reduced.

The CDT RABBIT level 1 trigger cards are computer controlled via FASTBUS. All control is via digital communication with the card's control and input disable registers. At present the following applications have been implemented.

The level 1 cards are currently downloaded at begin run time with other CDF trigger modules to operate in the single-fold coincidence mode. The CDT L0 trigger output is input to the CDF level 0 board to be used in CDF trigger decisions. The FASTBUS scalers are read out in the event structure as part of the SCLD bank. An Analysis_Control module to decode this information offline exists. A CDT trigger simulation module has also been written.

The CDT L1 trigger has used extensively by the CDT group for calibration. FORTRAN code has been written and installed in Run_Control to take Fe^{55} source calibration

data [31]. Utilizing special MX code and using the input disable lines to enable only selected tubes in the CDT array has substantially reduced the time and expertise needed to do an Fe^{55} source calibration. During the CDF run of 1987 the calibration took on the order of 25 days of nominally 24 hour operation. This was reduced to 14-15 hours.

The CDT pulser system uses the CDT L1 trigger to take the pulser data used for calibration of the CDT TDC channels and monitoring of CDT electronics.

The CDT L1 trigger can also be used independently or in conjunction with other CDF triggers to take cosmic-ray data. This is of limited utility since the trigger does not enter the main CDF trigger module (CDFFRED). Trigger logic must be constructed externally and input to AFRED.

A.3 Results

Fig. 80 shows typical charge-division results obtained from triggering on Fe^{55} sources

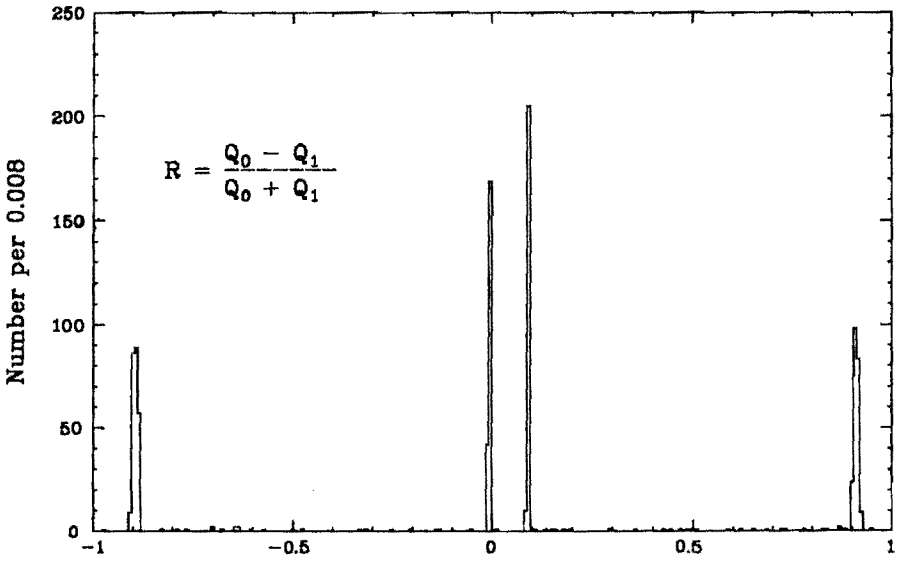

Figure 80: Typical charge-division results from triggering on the Fe^{55} sources of a drift tube pair. This data is used for calibration of the array.

from a single ganged drift tube pair in the CDT array. Typical singles counting rates per

ganged drift tube pair from cosmic rays plus Fe^{55} sources are $\sim$ 60 Hz [19]. In Fig. 81 are plotted typical ≥ 1, ≥ 2, ≥ 3, or $= 4$ -fold coincidence counting rates for each of the 42 OR outputs of the HV Pod pairs in the CDT array obtained during a typical $\bar{p}p$

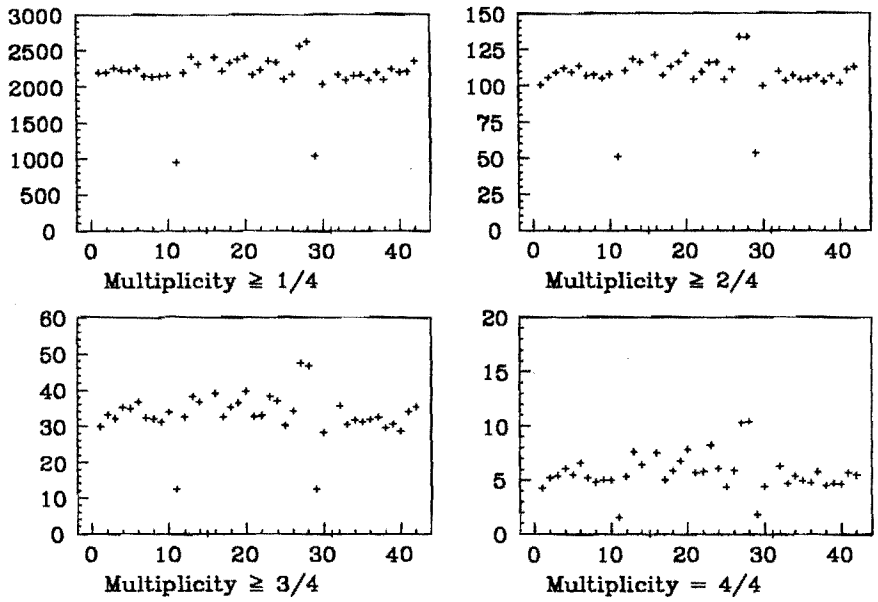

Figure 81: Counting rates from each of the 42 HV pod-pairs during physics data-taking. The rates for each coincidence setting in the level 1 cards are shown. Rates are given in hz.

collider run with luminosity of order $\mathcal{L} \sim 5 \times 10^{28}\ cm^{-2}\ s^{-1}$. These same plots are given in Fig. 82 for cosmic ray/Fe^{55} source data.

A.4 Conclusions

The CDF Central Drift Tube array's RABBIT level 1 trigger card is a versatile tool for use in calibration, monitoring, debugging the CDT array and for triggering purposes. The use of PALs as multiplicity logic units in the design of the CDT RABBIT level 1 trigger card considerably reduces its complexity and overall cost. The PAL multiplicity logic units on the card are simply controlled by addressable R/W registers and enable triggering on single ganged drift tube pairs or groups of ganged drift tube pairs anywhere in the 2016-tube CDT array, a feature useful for calibration and debugging purposes.

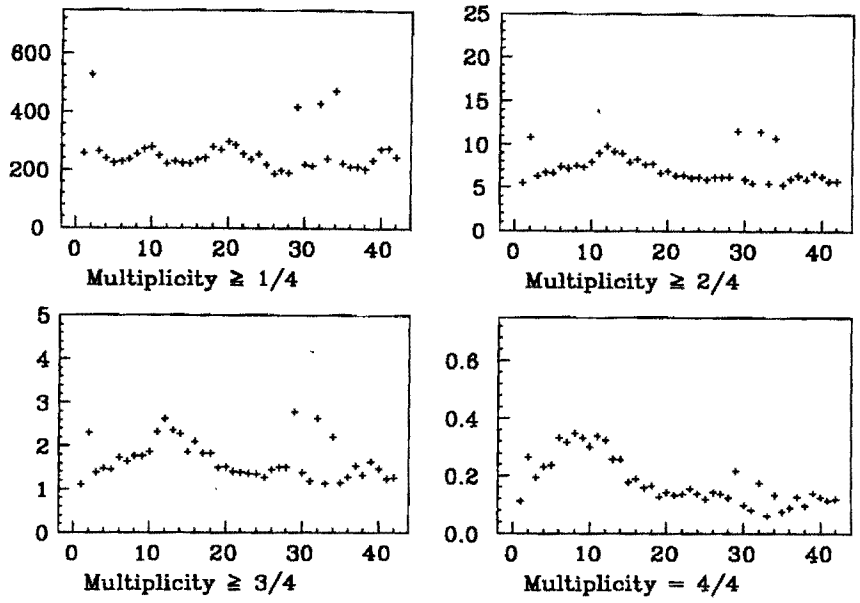

Figure 82: Counting rates from each of the 42 HV pod-pairs with no beam in the Tevatron. These rates are from cosmic rays and Fe^{55} sources. Rates are given in hz.

The same registers also allow triggering on prompt signals anywhere in the CDT array from $\bar{p}p$ collisions or from cosmic rays. Thus the CDT level 1 trigger card can be used for physics purposes as well as for monitoring and calibration purposes.

The CDT level 1 trigger card was designed entirely on the University of Illinois DAISY CAD/CAE system. It was thoroughly simulated in software before being built. Twenty CDT RABBIT level 1 trigger cards were mass-produced with no prior building or testing of a prototype CDT level 1 trigger card. No problems or difficulties of any significance were encountered in the installation and use of the trigger card. These cards have proven themselves to work extremely reliably and effectively at their intended design task.

B The CDT-CFT Level 0 Trigger

The first level of the CDF trigger system, level 0, selected inelastic $\bar{p}p$ collisions from from the background of uninteresting beam crossings: crossings with no $\bar{p}p$ interaction, beam-gas interactions and so on. In the 3.5 μs between crossings, it determined if the event was interesting and if so, inhibited data-taking for the next beam crossing in order for the next level trigger decision to be made. The level 0 trigger for most of the 1988-89 run consisted of a requirements on hits in the beam-beam counters (BBCs). The beam-beam counters consisted of scintillator counters arranged in a rectangular pattern around the beam pipe [16] forward and backward of the central detector. They covered the angular range $.32° < \theta < 4.47°$. In the pseudorapidity variable ($\eta = -\ln\tan(\theta/2)$), they cover $3.2 <\mid \eta \mid < 5.9$. The level 0 trigger required a coincidence of hits in the forward and backward sets of BBCs in-time with a beam-crossing.[20]

The motivation for a second level 0 trigger was the desire for angular coverage in level 0 outside the small forward-backward angular region covered by the BBCs. This was provided by the CDT-CFT level 0 trigger. The CDT-CFT trigger added coverage for the central region of the detector, $\mid \eta \mid < 1$, which does not overlap with the coverage of the BBCs.

The CFT part of the trigger required 1 or more prompt hits in each of the two innermost axial superlayers of the CTC, superlayers 0 and 2. The trigger accessed prompt hit information from the output of the CFT shift-register to make this decision. A description of the CFT is given in [28].

The CDT trigger is described in Appendix A. The requirement was that two of the four quadrants[21] of the CDT array contain 1 or more hit trigger clusters, where a hit

[20]This is an oversimplification. Other signals were used to inhibit data-taking when the Main Ring beam passed above the CDF detector or when detector power was lost. In addition, other beam-beam counter patterns were used to veto on beam-gas interactions. These are unrelated to the motivation for an additional level 0 trigger.

[21]Due to the configuration of the front-end system, the "quadrants" were not of equal size. Quadrants 0 and 2 covered 94.3° in azimuth; quadrants 1 and 3 covered 85.7°. These quadrants correspond to the

cluster consisted of hits in 2 or more of the 4 tubes in a cluster.

The CDT-CFT level 0 trigger was installed during the evening shift of May 22, 1989, nine days before the end of the run. The first run taken with this trigger was 20471 with trigger table Physics_V33$1 (CDF Logbook 54, p. 55). The level 0 cross section increased from 44 to 50 mb. (The beam luminosity for this store was a record low: 0.26×10^{30} cm^{-2}s^{-1}. The nominal level 0 rates are given in Table 18.

Trigger	Rate [hz]	Cross section [μb]
CDT	13100	53100
CTC L0	16100	65000
CTC L2	18200	73700
BBC east	14300	58000
BBC west	12700	51500
BBC_INTIME_INHIBIT	10900	44000
CTC_SL0_CTC_SL2_CDT_2	11700	47200
level 0	.10	.41

Table 18: Nominal rates for the level 0 trigger after installation of the CDT-CFT trigger. The cross section is computed for a beam luminosity of 10^{30} cm^{-2}s^{-1}.

four MXs [30] used to read out the CDT data.

C CDF HV Statistics

I present results from the monitoring of elapsed time and CPU time used by CDF systems during the raising and lowering of voltages and reconfiguration of relays for the gas calorimeters.

C.1 Introduction

Between the beginning of February, 1989, and the end of the 1988-89 run, I logged the elapsed time and CPU used by each CDF detector to turn on, off and to standby. After the middle of March, I monitored the same variables for the procedures used by the gas calorimeters to reconfigure relays. I present results from an analysis of this data.

C.2 Procedure

To raise and lower voltages for all systems except the CTC and to reconfigure relays for the gas calorimetry, subprocesses were spawned from the Alarms and Limits Menu program running on B0SCCC. Each time a subprocess was spawned, two measurements were made:

1) the time elapsed from when the process was spawned until it finished, and

2) the CPU used by the subprocess.

The data was written to a file on the B0 cluster. Files were copied to the University of Illinois High Energy Physics cluster by a server which ran daily.

Monitoring of all processes for the CES, CDT, CMU, FMU, forward, plug, and VTPC detectors began on 7 February and on 13 March for the gas calorimeter processes Start GG and End GG.

C.3 Analysis

I discard all data points which are obviously bad. Entries of elapsed time less than 0.1 minute or CPU less than 1 second are cut. I histogram the remaining data points for

the processes listed in Table 19. With the exception of Start GG and End GG, the

System	Processes
CES	on, off, standby
CDT	on, off, standby
CMU	on, off, standby
Plug/Forward	End GG
FMU	on, off, standby
Forward	on, off, standby
Plug	on, off, standby
Plug/Forward	Start GG
VTPC	on, off, standby

Table 19: List of detectors and processes for which statistics were monitored.

function of these processes is obvious. End GG turns the forward and plug voltages off and reconfigures the forward relays for physics data-taking. Start GG turns the forward and plug voltages off, reconfigures the forward relays for gas gain data-taking, and raises the plug and forward voltages on the chambers to off or standby and on the monitoring tubes to operate.

I present only data for the normal processes for raising and lowering detector voltages and for Start and End GG.

Figures 83 to 89 are histograms of the elapsed time and CPU used for each process. For each histogram I find the mean, standard deviation, and upper limit of the highest occupied bin ("MAX"). To reduce the effect of the tails of distributions, I cut all entries greater than two standard deviations from the mean and again find the upper limit of the highest occupied bin ("MAX (*)"). I also calculate the number of entries in the histogram and the number of entries cut.

Table 20 breaks down turn on time for each system month-by-month. Table 21 does the same for turn off time; Table 22, for turn on CPU; and Table 23, for turn off CPU. Tables 24 and 25 show the elapsed time and CPU for Start GG and End GG.

In Tables 26 and 27, I attempt to answer the question "How long does it really take

to turn CDF on (or off)?" Since the CMU voltages are raised before the shot is squeezed and lowered after the beam is dumped, I do not include it in the analysis. I have ranked the systems from slowest to fastest based on each of the three variables: mean, max and max (*) as described above.

Tables 28 and 29 contain a ranking of systems from most to least CPU used during the times when many subprocesses are spawned and competing for system resources. Table 30 ranks all processes for each of the variables by elapsed time and Table 31 does the same by CPU used.

Most often the systems were powered up or down by spawning processes from two Alarms and Limits Menu programs running concurrently on B0SCCC. Each Menu programs supports four subprocesses so that up to eight could be spawned in parallel. Since there is some evidence that overtaxing system resources contributes to the slowness of Alarms and Limits. I compute how long it would take to turn CDF on (or off) if we used only a single Menu program and spawned subprocesses as they became available. The results are summarized in Tables 32 to 37. It is clear that for lowering CDF voltages, one Menu is as good as two. If releasing system resources increases the speed with which subprocesses run or if, as one might expect, entries in the tails of the distributions are caused by system hangups, there would be gains from running with a single Menu. It is not so clear that this is true for raising the voltages. On the average one Menu is as good as two, but there will be times when it would be better to have both.

	Mean	std. dev.	Max	Max (*)	Tot. Ent.	# Cut
CES Feb.	2.76	0.33	4.25	3.00	20	1
CES Mar.	2.98	0.95	6.75	3.25	22	2
CES Apr.	3.16	0.87	6.50	4.00	23	2
CES All	2.97	0.80	6.75	4.25	65	4
CDT Feb.	5.39	0.74	7.75	6.75	23	1
CDT Mar.	5.52	1.01	8.75	7.00	33	2
CDT Apr.	6.23	1.24	9.50	7.25	27	2
CDT All	5.70	1.08	9.50	7.75	83	4
CMU Feb.	5.14	0.85	7.00	7.00	27	0
CMU Mar.	5.35	0.98	9.75	7.25	36	1
CMU Apr.	5.66	0.77	7.50	7.00	28	1
CMU All	5.38	0.91	9.75	7.25	91	2
FMU Feb.	3.27	1.75	6.50	6.50	32	0
FMU Mar.	3.35	0.59	6.25	4.00	26	1
FMU Apr.	4.19	1.68	8.75	7.75	28	1
FMU All	3.59	1.53	8.75	6.75	86	2
FWD Feb.	3.49	0.83	6.00	4.50	17	1
FWD Mar.	3.90	1.51	9.00	6.75	37	3
FWD Apr.	3.61	1.31	8.50	5.50	36	1
FWD All	3.71	1.33	9.00	6.00	90	5
PLG Feb.	4.74	1.20	8.75	7.25	25	1
PLG Mar.	4.74	0.89	8.25	6.00	23	1
PLG Apr.	5.04	1.14	9.25	6.75	37	2
PLG All	4.87	1.10	9.25	7.25	85	4
VTP Feb.	1.15	0.83	5.50	1.50	29	1
VTP Mar.	1.11	0.80	6.00	1.50	39	1
VTP Apr.	1.42	1.37	7.75	1.75	35	3
VTP All	1.23	1.05	7.75	1.75	103	5

Table 20: Time taken to turn on detector systems (in minutes). "Max (*)" is defined as the maximum entry in the distribution after cutting entries more than two standard deviations from the mean.

	Mean	std. dev.	Max	Max (*)	Tot. Ent.	# Cut
CES Feb.	0.80	0.44	2.75	1.25	21	1
CES Mar.	0.82	0.55	2.75	1.00	24	2
CES Apr.	0.81	0.26	1.75	1.25	25	1
CES All	0.81	0.43	2.75	1.75	70	3
CDT Feb.	4.94	1.00	7.25	6.25	25	1
CDT Mar.	5.17	1.72	9.25	6.75	29	3
CDT Apr.	5.83	1.36	9.25	8.50	39	1
CDT All	5.34	1.46	9.25	8.50	93	4
CMU Feb.	7.18	0.92	8.50	8.50	26	0
CMU Mar.	6.39	1.58	8.50	8.50	43	0
CMU Apr.	7.24	1.50	8.75	8.75	26	0
CMU All	6.86	1.46	8.75	8.75	95	0
FMU Feb.	0.95	0.22	1.50	1.50	22	0
FMU Mar.	1.57	0.95	3.25	3.25	29	0
FMU Apr.	1.69	0.70	3.25	3.25	25	0
FMU All	1.43	0.79	3.25	3.25	76	0
VTP Feb.	0.63	0.18	1.50	1.00	25	1
VTP Mar.	0.66	0.35	2.25	1.50	39	2
VTP Apr.	0.67	0.35	2.25	1.25	37	1
VTP All	0.66	0.31	2.25	1.50	101	3

Table 21: Time taken to turn off detector systems (in minutes).

	Mean	std. dev.	Max	Max (*)	Tot. Ent.	# Cut
CES Feb.	1.37	0.54	5.00	2.50	20	1
CES Mar.	1.25	0.00	2.50	2.50	22	0
CES Apr.	3.10	1.10	5.00	5.00	23	0
CES All	1.94	1.12	5.00	5.00	65	0
CDT Feb.	8.97	1.94	15.00	15.00	23	0
CDT Mar.	8.52	3.22	17.50	15.00	33	2
CDT Apr.	13.38	8.65	42.50	30.00	27	2
CDT All	10.23	5.86	42.50	17.50	83	4
CMU Feb.	9.21	6.56	37.50	17.50	27	1
CMU Mar.	7.78	2.45	15.00	15.00	36	0
CMU Apr.	10.71	3.74	22.50	20.00	28	1
CMU All	9.11	4.58	37.50	20.00	91	2
FMU Feb.	9.84	4.67	22.50	17.50	32	1
FMU Mar.	10.19	1.72	17.50	12.50	26	1
FMU Apr.	14.73	4.74	25.00	25.00	28	0
FMU All	11.54	4.61	25.00	22.50	86	4
FWD Feb.	31.10	13.30	62.50	55.00	17	1
FWD Mar.	46.74	24.66	100.00	90.00	37	1
FWD Apr.	26.25	16.48	65.00	57.50	36	2
FWD All	35.57	21.92	100.00	80.00	90	4
PLG Feb.	53.85	24.31	97.50	97.50	25	0
PLG Mar.	53.32	17.67	100.00	87.50	23	1
PLG Apr.	49.58	20.78	97.50	92.50	37	1
PLG All	51.88	21.22	100.00	92.50	85	3
VTP Feb.	6.59	2.52	15.00	10.00	29	1
VTP Mar.	5.99	2.45	15.00	12.50	39	1
VTP Apr.	11.25	6.15	22.50	22.50	35	0
VTP All	7.95	4.75	22.50	17.50	103	9

Table 22: CPU used to turn on detector systems (in seconds).

	Mean	std. dev.	Max	Max (*)	Tot. Ent.	# Cut
CES Feb.	1.61	0.87	5.00	5.00	21	0
CES Mar.	1.46	0.69	5.00	5.00	24	0
CES Apr.	3.05	1.12	5.00	5.00	25	0
CES All	2.07	1.17	5.00	5.00	70	0
CDT Feb.	8.15	3.62	20.00	15.00	25	1
CDT Mar.	8.06	3.07	15.00	15.00	29	0
CDT Apr.	13.88	8.51	40.00	32.50	39	3
CDT All	10.52	6.71	40.00	20.00	93	5
CMU Feb.	6.25	1.96	12.50	12.50	26	0
CMU Mar.	6.19	1.92	12.50	12.50	39	0
CMU Apr.	8.75	2.45	15.00	15.00	25	0
CMU All	6.92	2.38	15.00	12.50	90	1
FMU Feb.	9.55	1.39	15.00	12.50	22	1
FMU Mar.	9.78	2.41	15.00	15.00	29	0
FMU Apr.	13.35	3.37	17.50	17.50	25	0
FMU All	10.89	3.08	17.50	17.50	76	0
VTP Feb.	4.75	1.73	10.00	10.00	25	0
VTP Mar.	4.13	1.75	10.00	10.00	39	0
VTP Apr.	6.25	3.49	12.50	12.50	37	0
VTP All	5.06	2.69	12.50	12.50	101	0

Table 23: CPU used to turn off detector systems (in seconds).

	Mean	std. dev.	Max	Max (*)	Tot. Ent.	# Cut
EGG Mar.	5.89	1.65	9.50	9.50	18	0
EGG Apr.	6.15	2.18	15.50	10.50	32	1
EGG All	6.05	2.00	15.50	10.50	50	1
SGG Mar.	7.41	3.81	15.50	15.50	19	0
SGG Apr.	8.42	2.86	15.00	11.50	41	1
SGG All	8.10	3.23	15.50	15.00	60	1

Table 24: Time taken to run the relay reconfiguration processes for the gas calorimeters (in minutes).

	Mean	std. dev.	Max	Max (*)	Tot. Ent.	# Cut
EGG Mar.	36.81	11.63	56.25	56.25	18	0
EGG Apr.	46.48	36.21	243.75	62.50	32	1
EGG All	43.00	30.15	243.75	62.50	50	1
SGG Mar.	109.38	64.25	218.75	218.75	19	0
SGG Apr.	114.53	50.45	200.00	200.00	41	0
SGG All	112.87	55.32	218.75	218.75	60	0

Table 25: CPU used to run the relay reconfiguration processes for the gas calorimeters (in seconds).

	Mean		Max		Max (*)
CDT	5.70	CDT	9.50	CDT	7.75
PLG	4.87	PLG	9.25	PLG	7.25
FWD	3.71	FWD	9.00	FMU	6.75
FMU	3.59	FMU	8.75	FWD	6.00
CES	2.97	VTP	7.75	CES	4.25
VTP	1.23	CES	6.75	VTP	1.75

Table 26: The ranking of detectors from longest to shortest turn on times. Times are given in minutes.

	Mean		Max		Max (*)
SGG	8.10	SGG	15.50	SGG	15.00
CDT	5.34	CDT	9.25	CDT	8.50
FMU	1.43	FMU	3.25	FMU	3.25
CES	0.81	CES	2.75	CES	1.75
VTP	0.66	VTP	2.25	VTP	1.50

Table 27: The ranking of detectors from longest to shortest turn off times. Times are given in minutes.

	Mean		Max		Max (*)
PLG	51.88	PLG	100.00	PLG	92.50
FWD	35.57	FWD	100.00	FWD	80.00
FMU	11.54	CDT	42.50	FMU	22.50
CDT	10.23	FMU	25.00	CDT	17.50
VTP	7.95	VTP	22.50	VTP	17.50
CES	1.94	CES	5.00	CES	5.00

Table 28: The ranking of detectors from most to least CPU used during turn on. CPU is given in seconds.

	Mean		Max		Max (*)
SGG	112.87	SGG	218.75	SGG	218.75
FMU	10.89	CDT	40.00	CDT	20.00
CDT	10.52	FMU	17.50	FMU	17.50
VTP	5.06	VTP	12.50	VTP	12.50
CES	2.07	CES	5.00	CES	5.00

Table 29: The ranking of detectors from most to least CPU used during turn off. CPU is given in seconds.

	Mean		Max		Max (*)
SGG	8.10	SGG	15.50	SGG	15.00
CMU Std	6.86	EGG	15.50	EGG	10.50
EGG	6.05	CMU On	9.75	CMU Std	8.75
CDT On	5.70	CDT On	9.50	CDT Std	8.50
CMU On	5.38	CDT Std	9.25	CDT On	7.75
CDT Std	5.34	PLG On	9.25	CMU On	7.25
PLG On	4.87	FWD On	9.00	PLG On	7.25
FMU On	3.59	CMU Std	8.75	FMU On	6.75
FWD On	3.71	FMU On	8.75	FWD On	6.00
CES On	2.97	VTP On	7.75	CES On	4.25
FMU Std	1.43	CES On	6.75	FMU Std	3.25
VTP On	1.23	FMU Std	3.25	VTP On	1.75
CES Std	0.81	CES Std	2.75	CES Std	1.75
VTP Off	0.66	VTP Off	2.25	VTP Off	1.50

Table 30: Time bandits. The ranking of all processes by the time they take to execute (in minutes).

	Mean		Max		Max (*)
SGG	112.87	EGG	243.75	SGG	218.75
PLG On	51.88	SGG	218.75	PLG On	92.50
EGG	43.00	PLG On	100.00	FWD On	80.00
FWD On	35.57	FWD On	100.00	EGG	62.50
FMU On	11.54	CDT On	42.50	FMU On	22.50
FMU Std	10.89	CDT Std	40.00	CMU On	20.00
CDT Std	10.52	CMU On	37.50	CDT Std	20.00
CDT On	10.23	FMU On	25.00	FMU Std	17.50
CMU On	9.11	VTP On	22.50	CDT On	17.50
VTP On	7.95	FMU Std	17.50	VTP On	17.50
CMU Std	6.92	CMU Std	15.00	CMU Std	12.50
VTP Off	5.06	VTP Off	12.50	VTP Off	12.50
CES Std	2.07	CES Std	5.00	CES Std	5.00
CES On	1.94	CES On	5.00	CES On	5.00

Table 31: CPU hogs. The ranking of all processes by the CPU used (in seconds) during their execution.

	Proc. 1		Proc. 2		Proc. 3		Proc. 4
CDT	5.70	PLG	4.87	FWD	3.72	FMU	3.59
				VTP	1.23	CES	2.97
TOTAL	5.70		4.87		4.94		6.56

Table 32: An estimate of the total turn on time using 4 subprocesses. The mean time taken for each system is used for the estimate.

	Proc. 1		Proc. 2		Proc. 3		Proc. 4
CDT	9.50	PLG	9.25	FWD	9.00	FMU	8.75
				CES	6.75	VTP	7.75
TOTAL	9.50		9.25		15.75		16.50

Table 33: An estimate of the total turn on time using 4 subprocesses. The maximum time taken for each system is used for the estimate.

	Proc. 1		Proc. 2		Proc. 3		Proc. 4
CDT	7.75	PLG	7.25	FWD	6.75	FMU	6.00
				CES	1.75	VTP	4.25
TOTAL	7.75		7.25		8.50		10.25

Table 34: An estimate of the total turn on time using 4 subprocesses. The variable max (*) for each system is used for the estimate.

	Proc. 1		Proc. 2		Proc. 3		Proc. 4
SGG	8.10	CDT	5.34	FMU	1.43	CES	.81
						VTP	.66
TOTAL	8.10		5.34		1.43		1.47

Table 35: An estimate of the total turn off time using 4 subprocesses. The mean time taken for each system is used for the estimate.

	Proc. 1		Proc. 2		Proc. 3		Proc. 4
SGG	15.50	CDT	9.25	FMU	3.25	CES	2.75
						VTP	2.25
TOTAL	15.50		9.25		3.25		5.00

Table 36: An estimate of the total turn off time using 4 subprocesses. The maximum time taken for each system is used for the estimate.

	Proc. 1		Proc. 2		Proc. 3		Proc. 4
SGG	15.00	CDT	8.50	FMU	3.25	CES	1.75
						VTP	1.50
TOTAL	15.00		8.50		3.25		3.25

Table 37: An estimate of the total turn off time using 4 subprocesses. The variable max (*) for each system is used for the estimate.

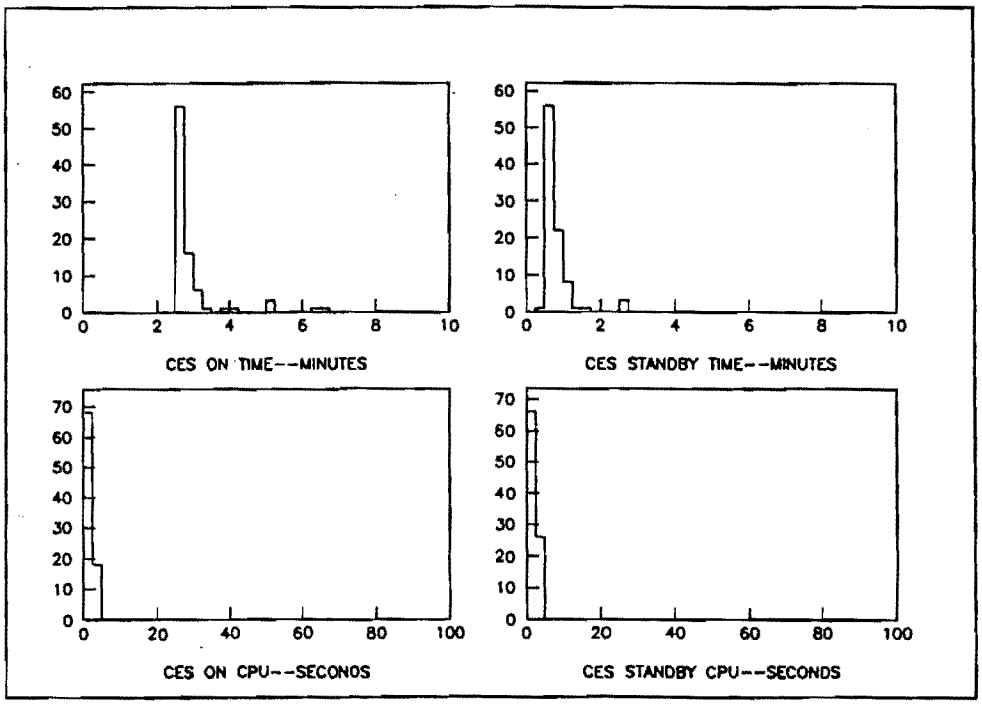

Figure 83: Summary of the analysis for the Central Electromagnetic Strip Detector.

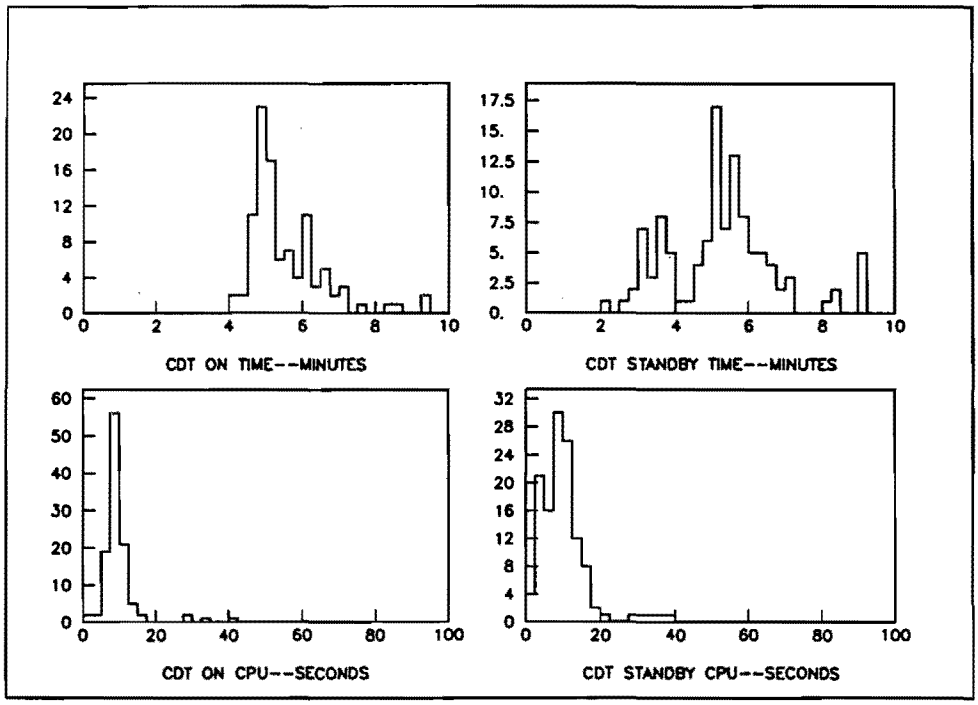

Figure 84: Summary of the analysis for the Central Drift Tube Array.

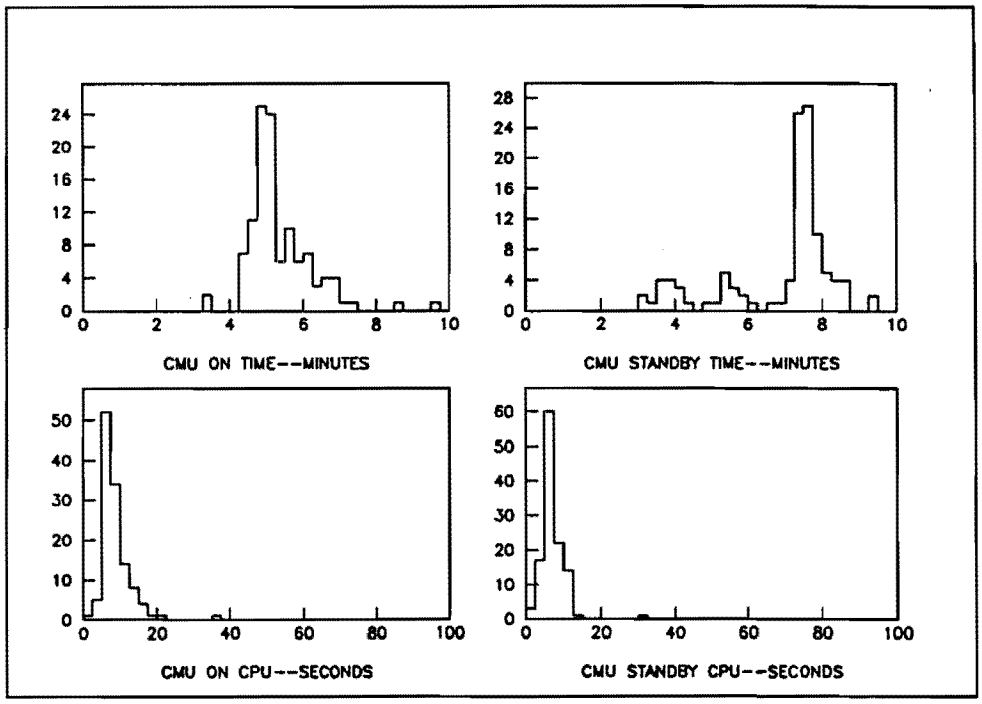

Figure 85: Summary of the analysis for the Central Muon Detector.

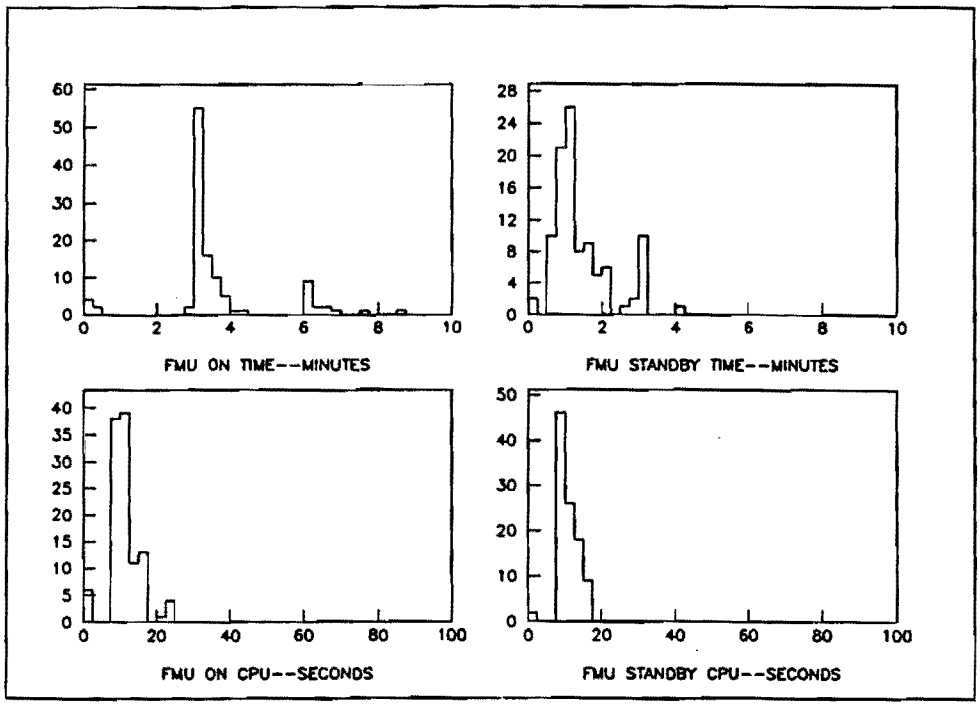

Figure 86: Summary of the analysis for the Forward Muon Detector.

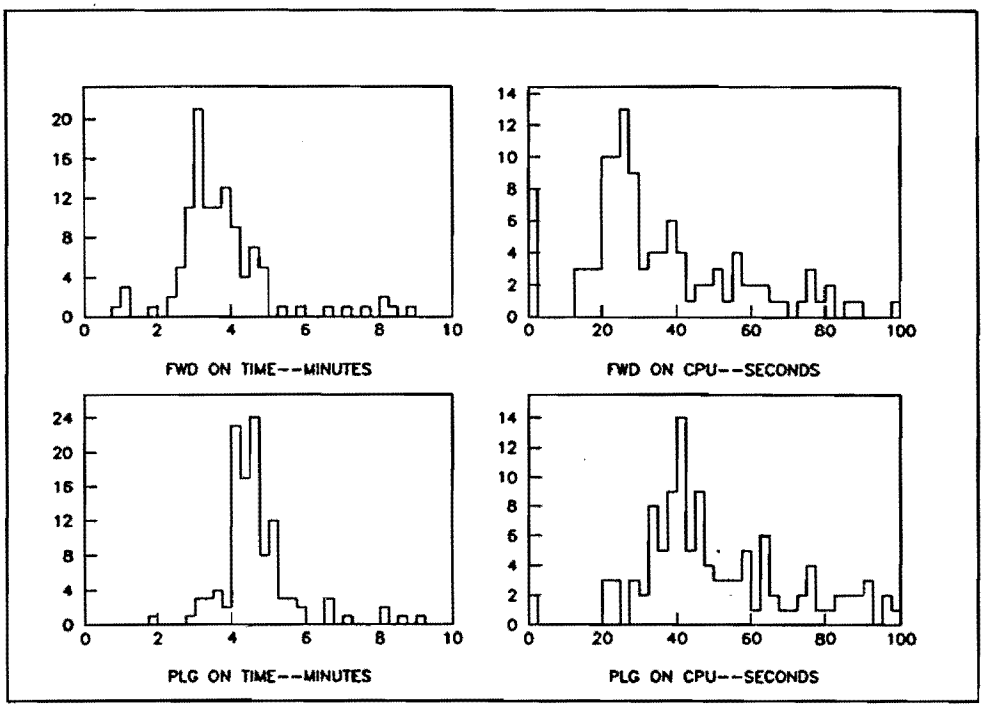

Figure 87: Summary of the analysis for the gas calorimeters.

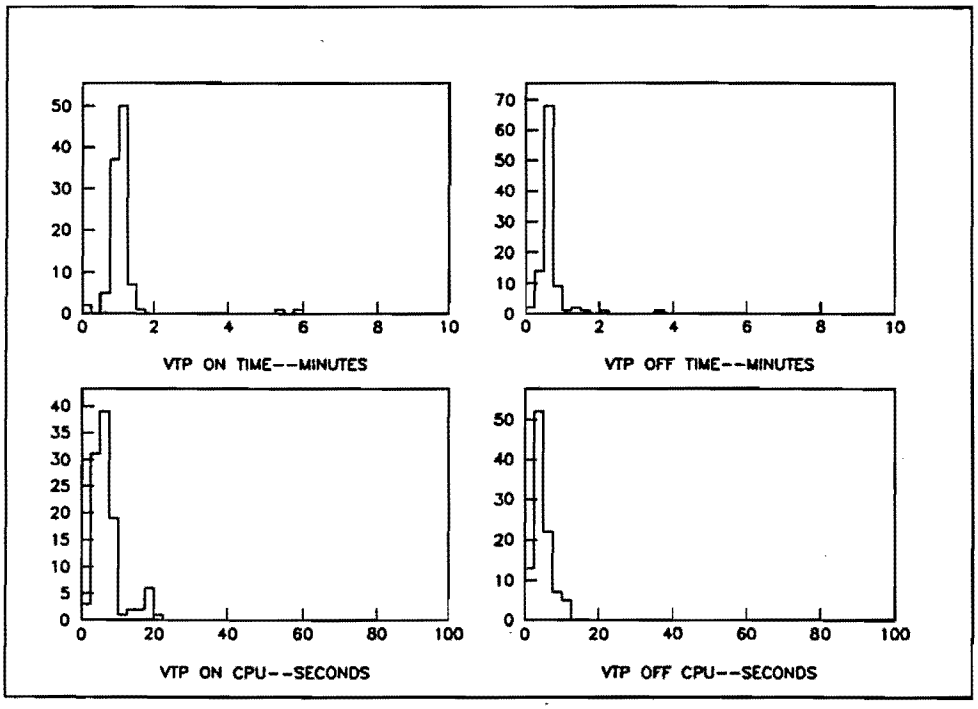

Figure 88: Summary of the analysis for the Vertex Time Projection Chambers.

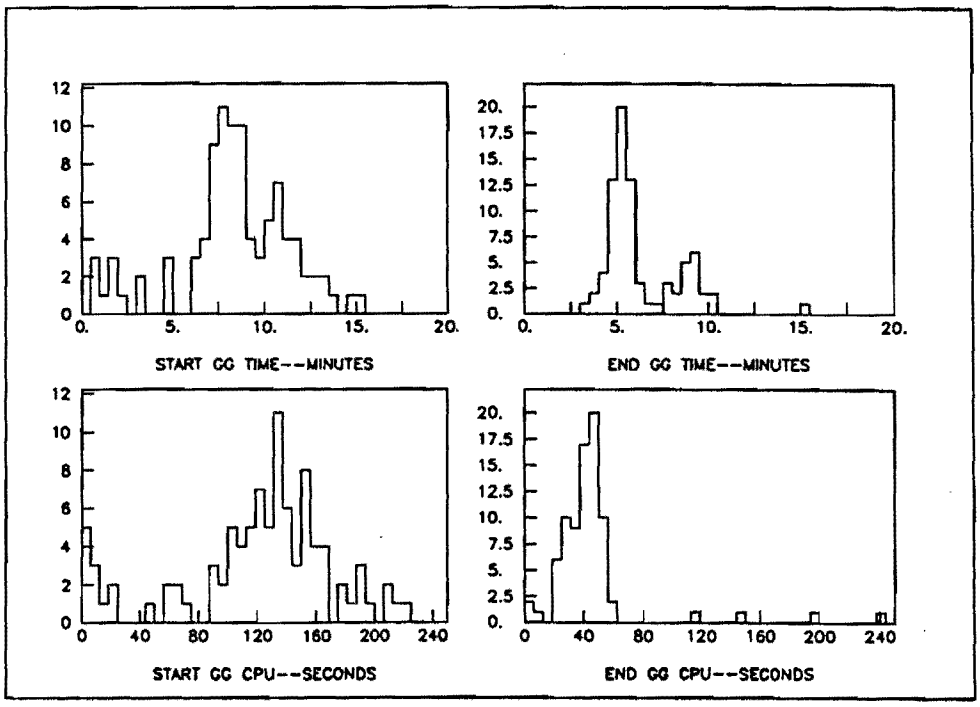

Figure 89: Summary of the analysis for the relay configuration processes used by the gas calorimeters.

D The CMU Readout Electronics

I first describe how the Central Muon Chamber readout system fits into the overall scheme of the CDF front-end system. Then I will describe calibration of the CMU readout electronics.

D.1 CMU in the CDF Front-End System

The primary function of the readout electronics for the Central Muon detector is to measure the charge deposited on the sense wire by the ionized drift electrons in a muon cell and the time at which this charge arrived at the sense wire and convert this measurement to digital information for addition to the event record. The readout electronics thus consists of 2304 charge-to-voltage (QVC) and 1152 time-to-voltage (TVC) conversion circuits (channels). These ADC and TDC channels reside on the muon QVC/TVC (MAT) card, a part of the RABBIT [30] system, the front-end of the CDF data acquisition system. A block diagram of the RABBIT system in given in Fig. 90. There are 144 of these cards in 48 crates on the detector. In addition to the three muon MAT cards, the crates contain two muon level 1 trigger cards (one for single muons, one for di-muons) and cards for reading out and calibrating the central calorimeter. The crates can contain up to 22 cards plus a timing signal generator card (BAT) and crate controller (EWE). All cards share a common backplane which has address lines for selecting each of the channels in the crate, power supply bus lines, timing signals, miscellaneous digital data and control signals, a few analog calibration and test lines, and analog signal (S) and return (R) lines. The voltage signal of a channel is a differential signal computed by comparing S and R.

A simplified schematic of the QVC/TVC channel is given in Fig. 91. The channels are associated in groups of three – two QVCs and one TVC. The QVCs are connected to opposite ends of the ganged sense wire pair.[22] The signals from the two ends are used in

[22]To reduce the number of electronic channels needed for chamber readout, sense wires from alternate

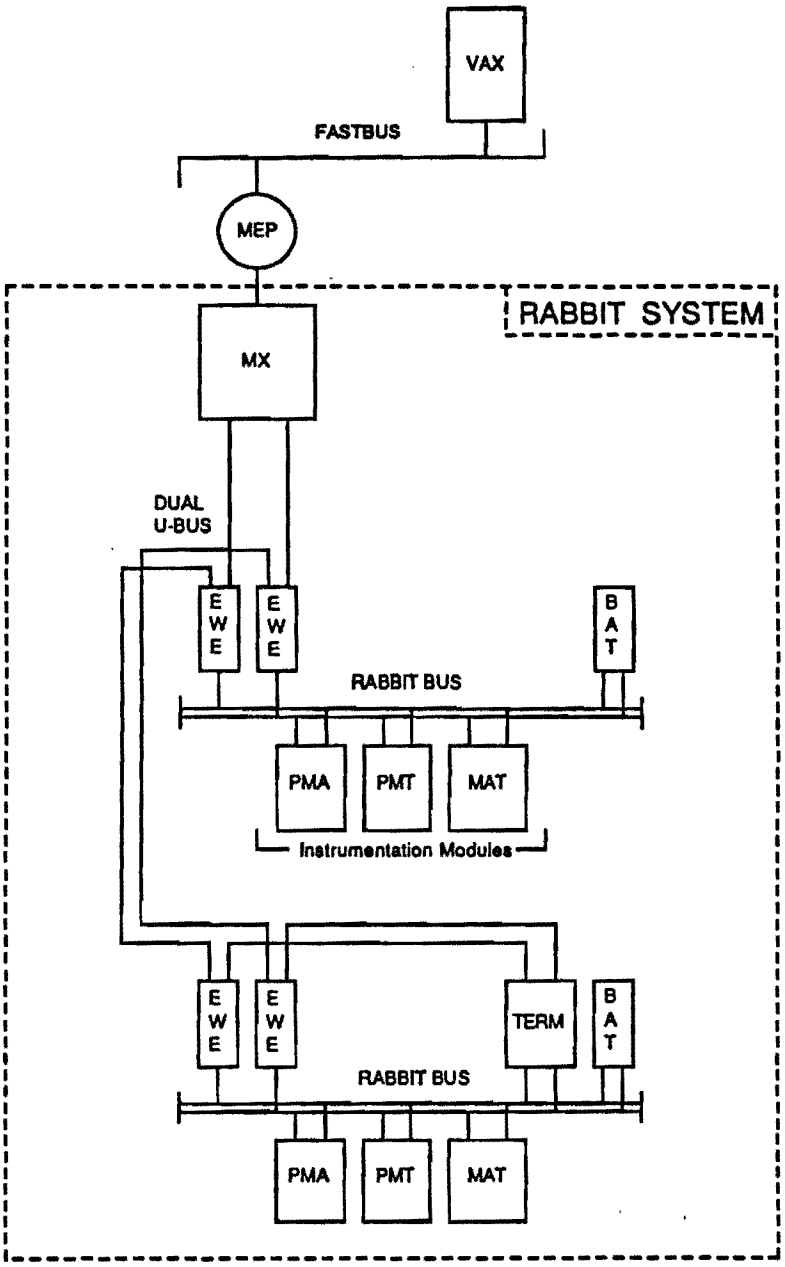

Figure 90: A block diagram of the CDF front-end electronics in the 1988-89 run.

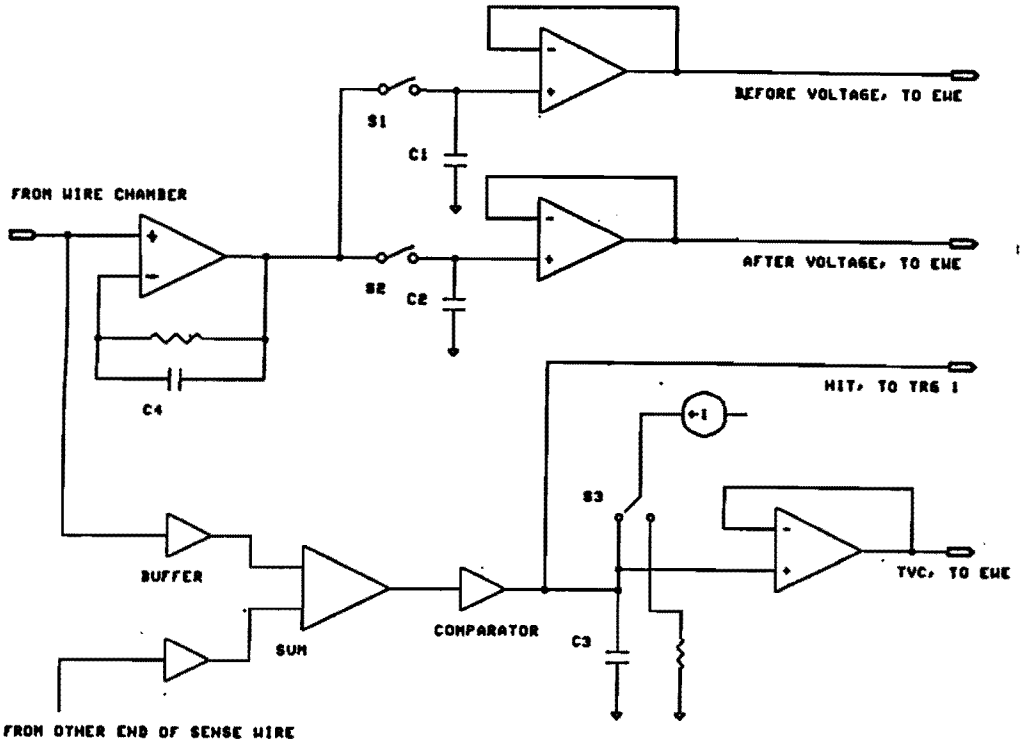

Figure 91: A simplified schematic of one channel of the QVC/TVC card. Note that there are two QVCs associated with each TVC. The two QVCs read out opposite sides of the sense wire pair.

the charge division calculation to compute the z position of the muon track. The QVC circuit is an integrating amplifier combined with two sample-and-hold circuits to measure (and ultimately compare) the voltage before the $\bar{p}p$ collision with the voltage after the collision. At an appropriate time before the $\bar{p}p$ collision, switches S1 and S2 of the sample-and-hold circuits are closed and C1 and C2 charge up at the same rate. Again, before the $\bar{p}p$ collision, S1 is opened, fixing the "before" signal. If a charged particle traverses the muon cell, the charge pulse from the drift elections travels down the wire to the integrating amplifier of the QVC, which converts the charge to an amplified voltage, which gets added to the signal on C2. A common stop signal for the entire front-end then closes S2, fixing the "after" signal. The TVC is connected via a buffer amplifier to the

cells in each layer of a muon chamber are ganged at $\theta = 90°$.

input of both QVCs. These are summed and amplified. When the signal exceeds a fixed threshold, a flip-flop changes state. This generates a digital HIT signal which is sent on to the level 1 trigger card and opens switch S3, which charges capacitor C3 until receipt of the common stop. The voltages on the three capacitors are buffered and multiplexed out to the crate backplane when selected by the crate controller.

The BAT takes an external timing signal (common for all RABBIT) and generates the backplane before-after signals. These and other digital timing control lines on the backplane are converted on the MAT card itself to signals appropriate for controlling the signal-and-hold and TVC circuits.

A schematic of the EWE is given in Fig. 92. The EWE controls and implements crate readout via the crate backplane. On a channel-by-channel basis, the EWE has the capability for analog pedestal subtraction, addition of a voltage offset to the signal, and selection of an overall gain of 1, 2, 4, or 8. In addition, the channel voltage may be compared to a threshold and a test-over-threshold signal generated. This allows for suppression of empty channels in the readout. The EWE takes a difference between any two of three backplane lines: signal (S), return (R), and ground (G), applies any of the analog operations listed above, and converts the result to a digital signal with 16-bit precision.

The EWE receives commands and data via an external bus from a special-purpose computer, the MX scanner, which is downloaded at begin run time with a list of channels to be read out and the pedestal, offset, gain and threshold information for each channel. For the 1988-89 run, a maximum of 8 EWEs could be controlled by each MX, although only two were connected. The MX hardware is implemented in ECL logic for speed. It has 80 kbytes of RAM storage. These are subdivided to store the scanner's control program, various constants including data correction constants for each channel, channel identifiers, a list of instructions for controlling the EWE, and event data. When the CDF detector is read out, the MX loops though its list of channels, issues the command

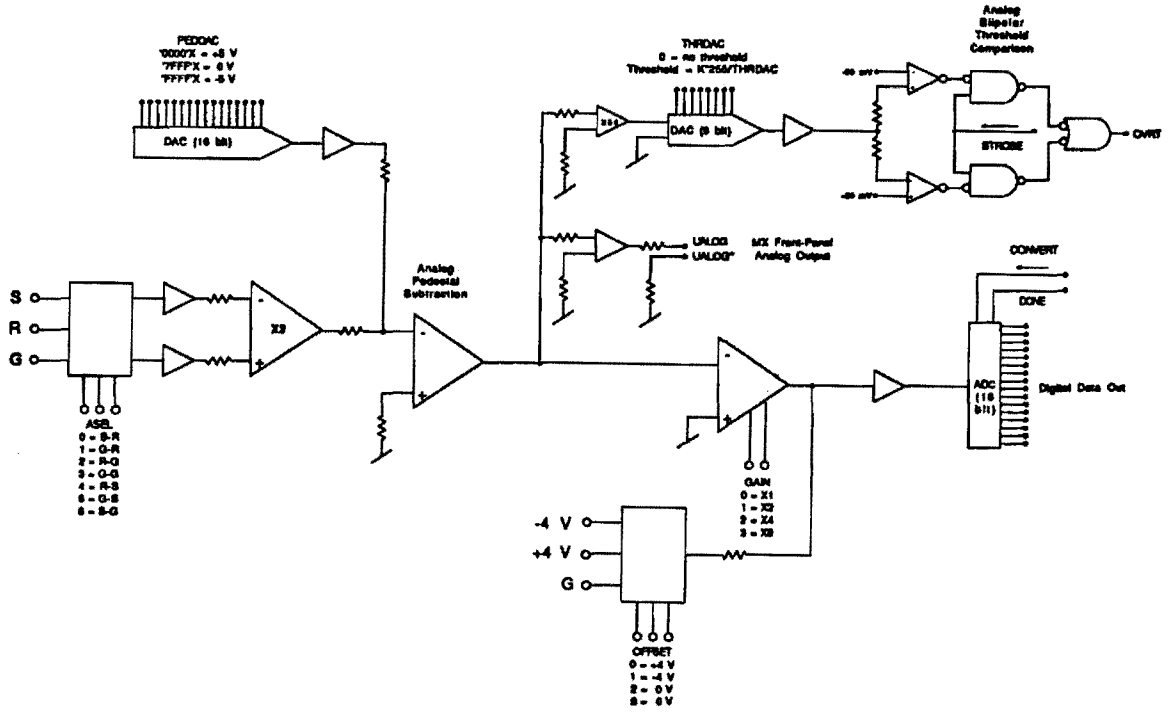

Figure 92: A simplified schematic of the EWE used in the 1988-89 run.

(decoded by the EWE to select gain, offset, test-over-threshold, and crate subaddress) appropriate for each channel, transfers any necessary data (pedestal and threshold), waits for the EWE to indicate that the ADC has finished conversion, takes the digital signal from the EWE, applies any channel-dependent correction constants, and stores it in internal memory. Since the EWE-MX bus is bi-directional, the MX must also control bus direction.

Data is transported from the MX to higher levels of the data acquisition system by the CDF FASTBUS network. The interface between MX and FASTBUS is the Multiple Event Port (MEP), which provides the standard FASTBUS slave interface. At the beginning of each run, the MX control program is downloaded from the VAX through the MEP to the MX. When readout of the detector is initiated, a start scan signal is sent to the MX. When the MX completes its scan of all channels, it returns a done signal to the MEP, which then allows data transfer out of the MX to be initiated at the request of higher level components of the data acquisition system.

D.2 Calibration

The gains of all the muon QVC and TVC channels were calibrated on a test stand [29] before insertion into the front-end [30] of the CDF data acquisition system. To calibrate the QVCs, a known charge is injected at the sense wire input and the voltage signal $(S-R)$ is read out. We calibrate across the full range of the QVC. We then compute gain and intercept by a linear, least-squares fit to the charge-voltage data. Gains and intercepts for all calibrated channels are plotted in Fig. 93. The TVC channels are calibrated somewhat differently. As in the QVC calibration, charge is injected to the inputs of one of the two QVCs associated with the TVC. This is, however, a fixed amount of charge, sufficient to "fire" the TVC, injected at a varying time with respect to the common stop signal of the test stand. The time is varied across the full range of the TVC and the voltage, $S-R$, corresponding to each is read out. Gain and intercept for the time-voltage data are

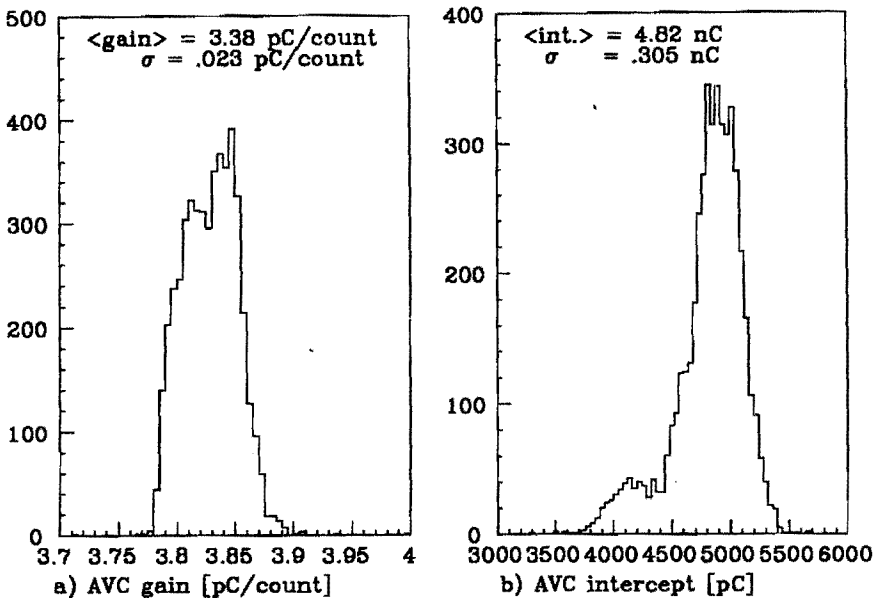

Figure 93: Histogram of the a) the gain and b) the intercept of the charge-to-voltage relationship for all calibrated QVC channels.

computed as for the QVCs and are plotted for all calibrated channels in Fig. 94. These constants are stored in a database for use locally and for transfer to the CDF offline database when appropriate. Several other calibrations and tests are done at this time. We measure the amount of charge – in counts, read from the channel QVC – which must be injected on each QVC to fire the associated TVC. Large thresholds lower the trigger efficiency and large discrepancies between channels effect the ability to calibrate relative timing offsets between channels (see below). Thus, we reject those channels which require more than several 100 counts to fire. Since this procedure uses the digital HIT output of the card to determine if the TDC has fired, we check these as well. We exercise all other functions implemented on the card and verify that they work.

Test stand calibrations alone are not sufficient to interpret signals from real $\bar{p}p$ collisions. Differences between the timing gate signals generated in different crates, the fact that a real chamber is connected to the QVC/TVC card as opposed to calibration electronics, the effect of the electronics used to extract the signal from the DC voltage

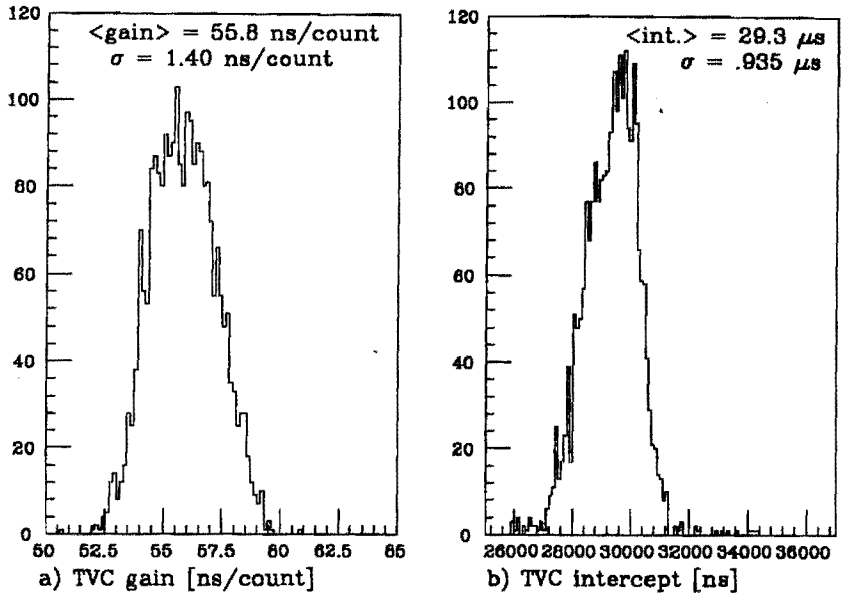

Figure 94: Histogram of the a) the gain and b) the intercept of the time-to-voltage relationship for all calibrated TVC channels.

of the sense wire, the different data acquisition system used to read out the information, the addition of other cards in the crate, and the fact that many channels are being read out at once will all combine to change the QVC and TVC relationships when the cards are installed on the detector.

For timing channels, these effects can be combined as offsets between channels: a relative t_0 between channels. These are determined by pulsing the sense wires *in situ*. Pulses are sent simultaneously to each of the 48 crates where they injected on the sense wire. Since all wires are "hit", these pulses fire the muon level 1 trigger which initiates detector readout. A channel is chosen as a reference and all channels are referenced to this. The data is corrected for the differing pulse propagation times to different crates. The length of the 48 pulse carrying cables has been measured by sending a pulse down the cable and measuring the time it takes to return. Half of this time will be reflected in the TVC data. Since the pulser is not synchronized with the central clock generating timing for the data acquisition system, events must be chosen that are well within the timing

gates used during $\bar{p}p$ data-taking to avoid spurious results. When these corrections are made, the differences between the reference channel and all other channels on a channel-by-channel and event-by-event bases are then computed over many events. Fig. 95 shows the distribution of the mean difference for all channels.

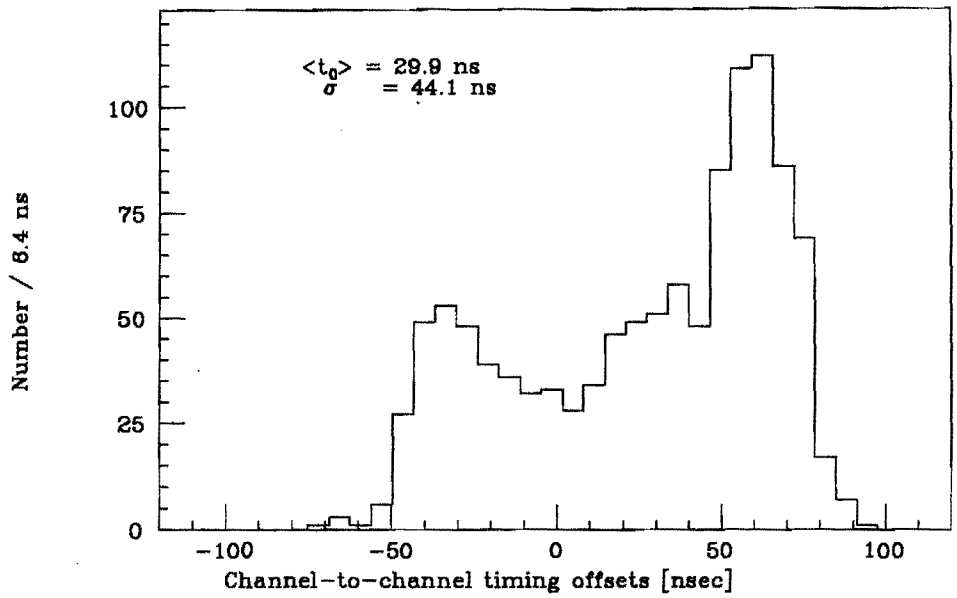

Figure 95: Histogram of the mean timing offset with respect to the reference channel for the 1152 TDC channels of the muon detector.

There is one further timing effect to measure. The global timing (global t_0) relationship between CDF clock and muon electronics is fixed by comparing the earliest hit distribution with the beam-beam crossing time. Data from particles which pass next to the sense wire have no component due to electron drift time. When corrected for channel-to-channel timing offsets, they measure the global offset between the clock and muon electronics. Raw TVC data accumulated over many $\bar{p}p$ events with the relative t_0 subtracted is plotted in Fig 96. The global t_0 is computed by the intercept of the falling edge with the horizontal axis. The background is due to hits from the Fe^{55} sources implanted in the chambers (see below) and cosmic rays which are in the event time window but are not from $\bar{p}p$ collisions.

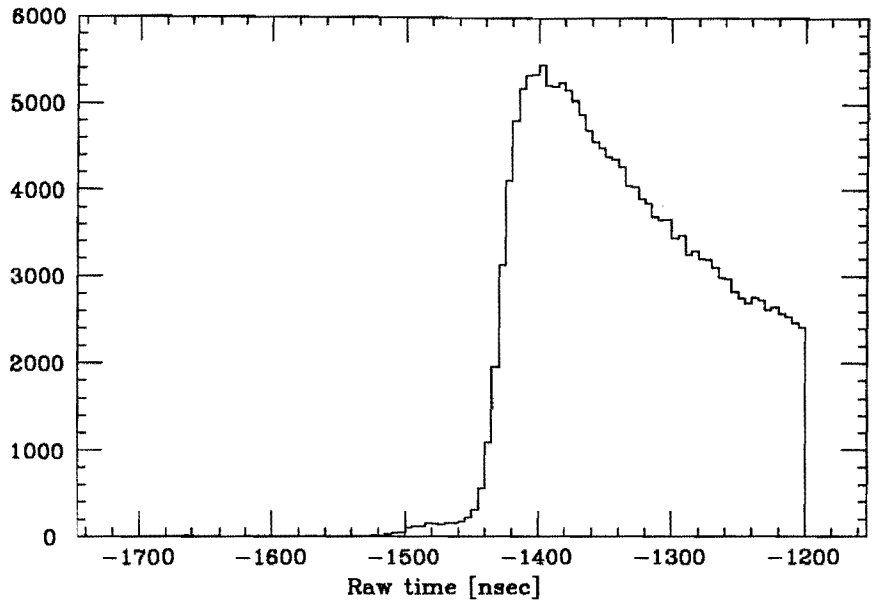

Figure 96: Histogram of raw digitized TVC data with relative t_0s subtracted. The leading edge of the distribution contains events in which a particle passed next to the sense wire in a muon cell. The global t_0 (defined to be the offset needed to set the drift time for such particles to 0) is $\sim$ 1450 nsec.

For the ADC channels, the baseline corresponding to no charge deposit on the sense wire is removed online. This baseline ("pedestal") was measured between each CDF data-taking run by reading out the ADC channels with the chambers unpowered. (With no electric field in the drift cell, cosmic rays and Fe^{55} source hits do not bias the data.) Each "event" is a determination of the pedestal for all 2304 channels. Pedestals are measured over many events and the average becomes part of the information downloaded to the MX at begin run time and is subtracted in the EWE from the channel signal in each event before readout (see above). Typical pedestal distributions are plotted in Fig. 97.

The charge division coordinate,

$$R = \frac{Q0 - Q1}{Q0 + Q1} \quad ,$$

where $Q0$ and $Q1$ are the analog signals read from the two ends of the sense wires, is mapped into z position by a calibration procedure using signals from Fe^{55} sources built

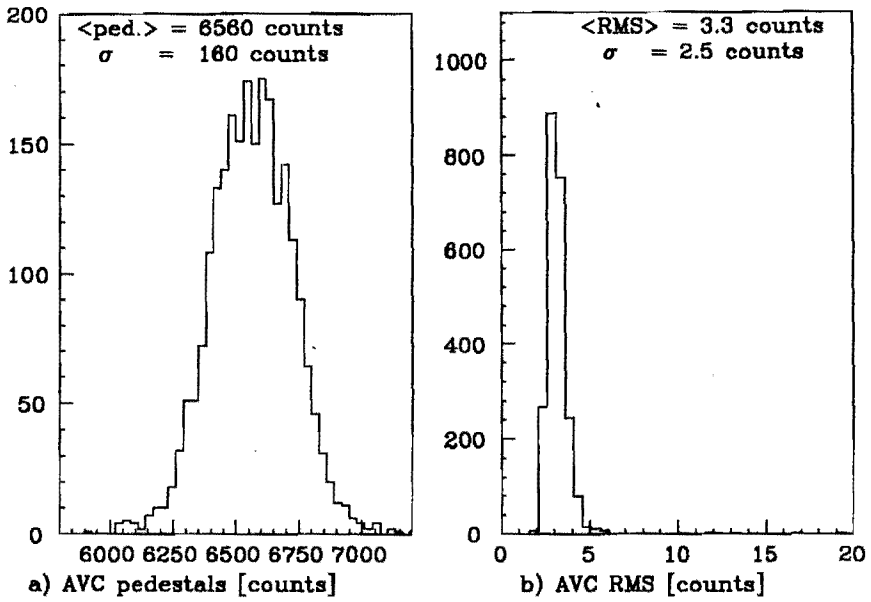

Figure 97: Histogram of a) the pedestals of 2304 ADC channels reading out the Central Muon chambers (in counts) and b) the error on each pedestal value.

into the chambers. Details of this calibration can be found in [31].

References

[1] G. Arnison *et al.* (UA1 collaboration). Experimental Observation of Isolated Large Transverse Energy Electrons with Associated Missing Energy at $\sqrt{s} = 540$ GeV. *Physics Letters*, B(122):103, 1983.

[2] Banner *et al.* (UA2 collaboration). Observation of Single Isolated Electrons of High Transverse Momentum in Events with Missing Transverse Energy at the CERN $\overline{p}p$ Collider. *Physics Letters*, B(122):476, 1983.

[3] Bagnaia *et al.* (UA2 collaboration). Evidence for $Z^0 \rightarrow e^+e^-$ at the CERN $\overline{p}p$ Collider. *Physics Letters*, B(129):130, 1983.

[4] Arnison *et al.* (UA1 collaboration). Experimental Observation of Lepton Pairs of Invariant Mass around 95 GeV/c^2 at the CERN SPS Collider. *Physics Letters*, B(129):273, 1983.

[5] F. Abe *et al.* (CDF Collaboration). Measurement of the Mass and Width of the Z^0 Boson at the Fermilab Tevatron. *Physical Review Letters*, 63(7):720, 1989.

[6] G. Abrams *et al.* (Mark II collaboration). Initial Measurements of the Z^0 Boson Resonance Parameters in e^+e^- Annihilation. *Physical Review Letters*, 63(7):724, 1989.

[7] D. Decamp *et. al.* Determination of the Number of Light Neutrino Species. *Physics Letters*, B(231):519, 1989.

[8] P. Aarnio *et. al.* The Mass and Width of the Z^o-Particle from Multihadronic Final States Produced in e^+e^- Annihilations. *Physics Letters*, B(231):539, 1989.

[9] B. Adeva *et. al.* Determination of the Properties of the Neutral Intermediate Vector Boson Z^o. *Physics Letters*, B(231):509, 1989.

[10] M. Akrawy *et. al.* Measurement of the Z^o Mass and Width with the OPAL Detector at LEP. *Physics Letters*, B(231):530, 1989.

[11] G. Abrams *et al.* (Mark II collaboration). Measurements of Z-Boson Resonance Parameters in e^+e^- Annihilation. *Physical Review Letters*, 63(20):2173, 1989.

[12] J. Alitti *et al.* (UA2 Collaboration). A Precise Determination of the W and Z masses at the CERN $p\bar{p}$ Collider. Technical Report EP/90-22, CERN, 1990. (Submitted to *Physics Letters B*).

[13] Hollik *et. al.* Radiative Corrections in the Standard Model and their Role for Precision Tests of the Electroweak Theory. Technical Report 88-188, DESY, 1988. (Unpublished).

[14] E.L. Berger, F. Halzen, C.S. Kim, and S. Willenbrock. Weak Boson Production at Fermilab Tevatron Energies. *Physical Review*, D(40):83, 1989.

[15] A.D. Martin, R.G. Robert, and W.J. Stirling. Structure Function Analysis and ψ, Jet, W, and Z Production. *Physical Review*, D(37):1161, 1988.

[16] F. Abe *et al.* (CDF Collaboration). The CDF Detector: An Overview. *Nuclear Instruments and Methods*, A(271):387, 1988.

[17] F. Snider *et al.* The CDF Vertex Time Projection Chamber System. *Nuclear Instruments and Methods*, A(268):75, 1988.

[18] F. Bedeschi *et al.* Design and Construction of the CDF Central Tracking Chamber. *Nuclear Instruments and Methods*, A(268):50, 1988.

[19] S. Bhadra *et al.* The Design and Construction of the CDF Central Drift Tube Array. *Nuclear Instruments and Methods*, A(267):92, 1988.

[20] S. Behrends *et al. Track Corrections to Jets and Jet Resolution.* CDF Note 1015.

[21] F. Abe *et al.* (CDF Collaboration). Measurement of the Inclusive Jet Cross Section at the Tevatron $\bar{p}p$ Collider. *Physical Review Letters*, 62(6):613, 1988. This reference provides a description of how we cluster energy into jet-like objects.

[22] M. Franklin. Performance of the Gas Calorimetry at CDF. In *Proceedings of the 7th Topical Workshop on Proton-Antiproton Collider Physics*, June 1988.

[23] D. Brown. *A Search for Multi-Parton Scattering at* $\sqrt{s} = 1.8$ *TeV.* PhD thesis, Harvard University, June 1989. (Unpublished).

[24] G. Ascoli *et al.* CDF Central Muon Detector. *Nuclear Instruments and Methods*, A(267):218, 1988.

[25] Thomas Kevin Westhusing. *Observation of* $W \rightarrow \mu\nu$ *Decays in Proton-Antiproton Collisions at* $\sqrt{s} = 1.8$ *TeV.* PhD thesis, University of Illinois at Urbana-Champaign, December 1989. (Unpublished).

[26] D. Amidei *et al.* A Two Level FASTBUS Based Trigger System for CDF. *Nuclear Instruments and Methods*, A(273):51, 1988.

[27] G. Ascoli *et al.* Central Muon Level-1 Trigger Electronics. *Nuclear Instruments and Methods*, A(267):272, 1988.

[28] G.W. Foster *et al.* A Fast Hardware Track-Finder for the CDF Central Tracking Chamber. *Nuclear Instruments and Methods*, A(269):93, 1988.

[29] D. A. Smith. *Study of Muons in Proton-Antiproton Collisions at* $\sqrt{s} = 1.8$ *TeV.* PhD thesis, University of Illinois at Urbana-Champaign, December 1989. (Unpublished).

[30] G. Drake *et al.* CDF Front End Electronics: The Rabbit System. *Nuclear Instruments and Methods*, A(273):287, 1988.

[31] H. Keutelian. *Measurement of the Mass and Width From $Z^0 \rightarrow e^+e^-$ Decay in $\overline{P}P$ Collisions at $\sqrt{s} = 1.8$ TeV.* PhD thesis, University of Illinois at Urbana-Champaign, May 1990. (Unpublished).

[32] A. Mukherjee *et al.* Calibration of the CDF Central Detector. *Nuclear Instruments and Methods.* In preparation.

[33] F. Abe *et al.* (CDF Collaboration). A Measurement of the W Boson Mass in 1.8 TeV $\bar{p}p$ Collisions. *Physical Review*, D, 1990. In preparation.

[34] The Particle Data Group. Review of Particle Properties. *Physics Letters*, 1990. To be published.

[35] The Particle Data Group. Review of Particle Properties. *Physics Letters*, B(204), 1988.

[36] P. Tipton *et al. A Summary of the New Spin Cycle.* CDF Note 795.

[37] F. Paige and S.D. Protopopescu. Technical Report BNL 38034, Brookhaven National Laboratory, 1986. (unpublished).

[38] Alain Gauthier. *CTC Tracking Studies with Cosmic Rays.* CDF Note 965.

[39] V. Barger and A.D.Martin. Perpendicular $e\nu$ Mass From W Decay. *Zeitschrift fur Physik*, C(21):99, 1983.

[40] R.N. Cahn. Analytic Forms for the e^+e^- Annihilation Cross Section Near the Z Including Initial-State Radiation. *Physical Review D*, 36(9):2666, 1987.

[41] G.Altarelli, R.K.Ellis, M.Greco and G.Martinelli. Vector Boson Production at Colliders: A Theoretical Reappraisal. *Nuclear Physics*, B(246):12, 1984. For a more recent non-calculation of this effect, see also: Arnold and Reno, *NuclearPhysics* B(319):37,1989.

[42] William Trischuk. *A Measurement of the W Boson Mass in* 1.8 *TeV Proton-Antiproton Collisions.* PhD thesis, Harvard University, April 1990. (Unpublished).

[43] E. Eichten, I. Hinchliffe, K. Lane, and C. Quigg. Supercollider Physics. *Reviews of Modern Physics*, 56:579, 1984.

[44] D. Duke and J. F. Owens. Q^2-Dependent Parameterizations of Parton Distribution Functions. *Physical Review*, D(30):49, 1984.

[45] M.Diemoz, F.Ferroni, E.Longo, and G.Martinelli. Parton Densities from Deep Inelastic Scattering to Hadronic Processes at the Super Collider. *Z. Phys.*, C(39):21, 1988.

[46] David Saltzberg. *Statistical and Systematic Uncertainties in the W Mass from Electrons.* CDF Note 1128.

[47] F. James and M. Roos. *Function Minimization and Error Analysis*, 1983. CERN Program Library Documentation.

[48] W. Press, B. Flannery, S. Teukolsky, and W. Vetterling. *Numerical Recipes*, chapter 3, pages 97–101. Cambridge University Press, 1986.

[49] P. Schlabach and W. Trischuk. *The Fitter Jitter.* CDF Note 1174.

[50] P. Schlabach. *The W Fitter at Urbana-Champaign.* CDF Note 1149.

[51] W. Press, B. Flannery, S. Teukolsky, and W. Vetterling. *Numerical Recipes*, chapter 3, pages 86–89. Cambridge University Press, 1986.

[52] P. Schlabach. *Smoothing the W Mass Look-up Tables.* CDF Note 1203.

[53] F. Behrends and R. Kleiss. Hard Photon Effects in $W^{\pm}$ and Z^0 Decay. *Zeitschrift fur Physik*, C(27):365, 1985.

[54] R. G. Wagner. Unpublished, based on calculations by F. Berends. *et al.*, Z. Phys. C (27):155, 1985; F. Behrends and R. Kleiss, Z. Phys. C (27):365, 1985.

[55] F. Abe *et al.* (CDF Collaboration). Measurement of the Ratio $\sigma(W \rightarrow e\nu)$ / $\sigma(Z \rightarrow ee)$ in $p\bar{p}$ Collisions. *Physical Review Letters*, 64(2):152, 1990.

[56] P. Derwent. *Measurement of* $\sigma(W \rightarrow e\,\nu)$ *and* $\sigma(Z^0 \rightarrow e^+\,e^-)$ *in* $\bar{p}p$ *collisions at* $\sqrt{s}$ = *1800 GeV.* PhD thesis, University of Chicago, August 1990. In preparation.

[57] F. Abe *et al.* (CDF collaboration). Search for New Heavy Quarks in Electron-Muon Events at the Fermilab Tevatron Collider. *Physical Review Letters*, 64(2):147, 1990.

[58] F. Abe *et al.* (CDF Collaboration). Search for the Top Quark in the Reaction $p\bar{p} \rightarrow$ electron + jets at $\sqrt{s} = 1.8$ TeV. *Physical Review Letters*, 64(2):142, 1990.

[59] *Monolithic Memories Data Book.*

Vita

It all started some 150 years ago when Christian Shetler left Germany for the new world. Six generations later, young Phil left the Appalachian foothills for the big city and Haverford College, there to test his mettle against the best the east coast had to offer. In that 150 years, Phil managed to be [redacted], move to Ohio, and get 12 years of schooling. After two years at Haverford, he'd had as much fun as he could stand; so he worked for a year in a testing laboratory in New Philadelphia, Ohio. Having forgotten how much fun it was, he went back to Haverford for a year. Then it was off to Case Western Reserve University to try his luck at electrical engineering. It was clear that a career as a high jumper was out of the question and hanging around all those engineering students finally convinced him he was bright enough for graduate school; so it was off to Illinois to learn about the solid state of matter. Six weeks of Physics 489 was too much fun, so he decided to build some drift tubes. Then it was off to Fermilab to work on the CDF detector for a couple of years. He'd obviously been having lots of fun; because, when Lee Holloway said, "Let's measure the W mass", Phil thought he said, "Let's invade Russia", and replied, "OK". After months of slogging across the frozen steppes, fighting off hordes of Cossacks at every turn, and generally having all kinds of fun, he and William and Larry and Lee got within sight of Moscow, and certainly within shouting distance of the W mass; so they declared victory. Three of them went home; the fourth left the country. Phil wanted to move to Montana and raise goats; but that would be too much fun. So it's back to CDF to work for Harvard. Lately, the slightly older Phil has just been sitting around, picking the guitar and singing that old Paul Simon ditty that starts: "When I think of all the crap I learned in grad school, it's a wonder I know anything at all . . ."